William & Mary
CHARTERED 1693

W&M ScholarWorks

Dissertations, Theses, and Masters Projects

Theses, Dissertations, & Master Projects

1980

# Improved characterization of silicon-silicon-dioxide interfaces

Pin Su
*College of William & Mary - Arts & Sciences*

Follow this and additional works at: https://scholarworks.wm.edu/etd

Part of the Condensed Matter Physics Commons

## Recommended Citation

Su, Pin, "Improved characterization of silicon-silicon-dioxide interfaces" (1980). *Dissertations, Theses, and Masters Projects.* Paper 1539623719.
https://dx.doi.org/doi:10.21220/s2-gtw0-kw09

This Dissertation is brought to you for free and open access by the Theses, Dissertations, & Master Projects at W&M ScholarWorks. It has been accepted for inclusion in Dissertations, Theses, and Masters Projects by an authorized administrator of W&M ScholarWorks. For more information, please contact scholarworks@wm.edu.

## INFORMATION TO USERS

This was produced from a copy of a document sent to us for microfilming. While the most advanced technological means to photograph and reproduce this document have been used, the quality is heavily dependent upon the quality of the material submitted.

The following explanation of techniques is provided to help you understand markings or notations which may appear on this reproduction.

1. The sign or "target" for pages apparently lacking from the document photographed is "Missing Page(s)". If it was possible to obtain the missing page(s) or section, they are spliced into the film along with adjacent pages. This may have necessitated cutting through an image and duplicating adjacent pages to assure you of complete continuity.
2. When an image on the film is obliterated with a round black mark it is an indication that the film inspector noticed either blurred copy because of movement during exposure, or duplicate copy. Unless we meant to delete copyrighted materials that should not have been filmed, you will find a good image of the page in the adjacent frame.
3. When a map, drawing or chart, etc., is part of the material being photographed the photographer has followed a definite method in "sectioning" the material. It is customary to begin filming at the upper left hand corner of a large sheet and to continue from left to right in equal sections with small overlaps. If necessary, sectioning is continued again—beginning below the first row and continuing on until complete.
4. For any illustrations that cannot be reproduced satisfactorily by xerography, photographic prints can be purchased at additional cost and tipped into your xerographic copy. Requests can be made to our Dissertations Customer Services Department.
5. Some pages in any document may have indistinct print. In all cases we have filmed the best available copy.

University Microfilms International

300 N. ZEEB ROAD, ANN ARBOR, MI 48106
18 BEDFORD ROW, LONDON WC1R 4EJ, ENGLAND

8103586

SU, PIN

IMPROVED CHARACTERIZATION OF SILICON - SILICON-DIOXIDE INTERFACES

*The College of William and Mary in Virginia* PH.D. 1980

University
Microfilms
International 300 N. Zeeb Road, Ann Arbor, MI 48106

# IMPROVED CHARACTERIZATION OF $Si$-$SiO_2$ INTERFACES

---

A Dissertation
Presented to
The Faculty of the Department of Physics
The College of William and Mary in Virginia

---

In Partial Fulfillment
Of the Requirements for the Degree of
Doctor of Philosophy

---

by

Pin Su

June 1980

APPROVAL SHEET

This thesis is submitted in partial fulfillment of

the requirements for the degree of

Doctor of Philosophy

Pin Su

Approved, June 1980

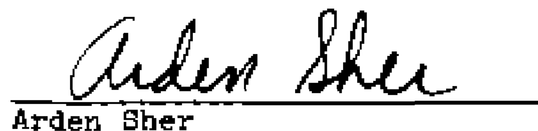

Arden Sher

Harlan E. Schone

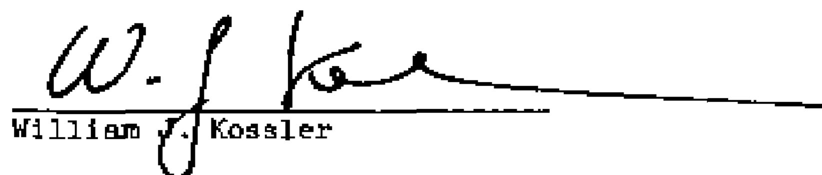

William J. Kossler

Mark S. Conradi

Roger A. Breckenridge
NASA-Langley

To my parents

TABLE OF CONTENTS

| | | Page |
|---|---|---|
| | ACKNOWLEDGMENTS . . . . . . . . . . . . . . . . . . . . . . . . | v |
| | LIST OF TABLES . . . . . . . . . . . . . . . . . . . . . . . . | vi |
| | FIGURE CAPTIONS . . . . . . . . . . . . . . . . . . . . . . . . | viii |
| | ABSTRACT . . . . . . . . . . . . . . . . . . . . . . . . | xv |
| I. | INTRODUCTION . . . . . . . . . . . . . . . . . . . . . . . . | 2 |
| II. | PRINCIPAL FEATURES OF THE EXPERIMENTAL METHODS . . . . | 7 |
| | A. Quasistatic method . . . . . . . . . . . . . . . . . | 7 |
| | B. Conductance method . . . . . . . . . . . . . . . . . | 7 |
| | C. Capacitance-Voltage (C-V) method . . . . . . . . . . | 8 |
| | D. Deep level transient spectroscopy (DLTS) . . . . . | 9 |
| | E. Elevated temperature method . . . . . . . . . . . . | 11 |
| III. | SAMPLE PREPARATION . . . . . . . . . . . . . . . . . . . . | 14 |
| IV. | QUASISTATIC METHOD . . . . . . . . . . . . . . . . . . . . | 20 |
| | A. Quasistatic capacitance method . . . . . . . . . . | 20 |
| | 1. The measurement method . . . . . . . . . . . . | 20 |
| | 2. The quasistatic condition . . . . . . . . . . . | 22 |
| | 3. Determination of $C_0$ . . . . . . . . . . . . . . | 24 |
| | 4. Determination of the surface potential . . . . | 25 |
| | B. Apparatus . . . . . . . . . . . . . . . . . . . . . . | 31 |
| | C. Extra features in quasistatic C-V curve . . . . . . | 31 |

| | | Page |
|---|---|---|
| V. | CONDUCTANCE METHOD . . . . . . . . . . . . . . . . . . . . . . | 43 |
| | A. The method . . . . . . . . . . . . . . . . . . . . . . | 43 |
| | B. Physical models . . . . . . . . . . . . . . . . . . . . . . | 45 |
| | 1. Discrete model . . . . . . . . . . . . . . . . . . | 46 |
| | 2. Continuum model . . . . . . . . . . . . . . . . . . | 49 |
| | 3. Statistical broadening . . . . . . . . . . . . . . | 52 |
| | C. Apparatus . . . . . . . . . . . . . . . . . . . . . . . | 57 |
| | D. Experimental results . . . . . . . . . . . . . . . . . | 59 |
| | 1. Results of the discrete model . . . . . . . . . . | 59 |
| | 2. Modified continuum model . . . . . . . . . . . . . | 61 |
| | 3. A sample with statistical broadening . . . . . . | 64 |
| | 4. Time constant . . . . . . . . . . . . . . . . . . . | 66 |
| VI. | OTHER INTERESTING DATA . . . . . . . . . . . . . . . . . . | 85 |
| | A. Si-58 at liquid nitrogen temperature (77°K) . . . . | 85 |
| | B. Si-101 . . . . . . . . . . . . . . . . . . . . . . . . | 87 |
| | C. Si-102 . . . . . . . . . . . . . . . . . . . . . . . . | 89 |
| | D. Si-107 . . . . . . . . . . . . . . . . . . . . . . . . | 90 |
| VII. | DISCUSSION . . . . . . . . . . . . . . . . . . . . . . . . | 103 |
| | A. The "Ideal" Si-$SiO_2$ interface . . . . . . . . . . . | 107 |
| | B. Scattering-induced band tails . . . . . . . . . . . . | 107 |
| | C. Hybridization and resonant scattering . . . . . . . | 111 |
| VIII. | CONCLUDING REMARKS . . . . . . . . . . . . . . . . . . . | 117 |
| | REFERENCES . . . . . . . . . . . . . . . . . . . . . . . | 120 |

## ACKNOWLEDGMENTS

I wish to express my gratitude to the following persons:

My advisor Arden Sher for the guidance and effort he has contributed to this work;

Bill Miller for his generous supply of equipment and many enlightening discussions;

Simon Tsuo for instruction in experimental methods and much invaluable advice;

Tommy Steele for help with sample preparation;

H. E. Schone, W. J. Kossler, M. S. Conradi, and R. A. Breckenridge for their careful reading of my dissertation and for serving on my dissertation committee;

Sylvia Stout for her assistance and expert typing.

Finally, I wish to thank Hwey-Lain for her understanding and encouragement.

LIST OF TABLES

Table | Page

III-1. Total insulator capacitance measured on Si-58 using the quasistatic method (same ramp rate, different light intensities) at three different temperatures . . 15

III-2. A detailed step-by-step sample preparation procedure . 18

IV-1. Measurable energy ranges of Si-58 at three different temperatures. Higher light intensity was used for lower temperature in order to satisfy the low-frequency condition . . . . . . . . . . . . . . . . . . 29

IV-2. Parameters associated with the two fluorine peaks in Figures IV-6 and 7 . . . . . . . . . . . . . . . . . . 34

V-1. Measured and calculated capacitances and time constants for different applied biases V (volts) and energies E (eV) relative to the valence-band edge. The units of all capacitances are farads, and time constants are seconds. The subscripts I, v, c, f1, f2, and d denote inversion layer, valence-band tail, conduction-band tail, fluorine 1, fluorine 2, and depletion layer, respectively. $C_p$ is the parallel capacitance indicated in Figure (V-2), $C_{QS}$ is the total quasistatic capacitance, and $C_D$ is the total space-charge capacitance [Ref. 2] (inversion plus depletion/

Table | Page

accumulation) calculated from the measured surface potential. For biases V, for which there are two entries, the upper one was taken in the light, with no filter, and the lower one was taken in the dark. The interpretation of the numbers in parentheses is uncertain, and they were not included in the plots . . . 69

V-2. Parameters $N^j_{SSF}$ and $\tau_s$ in Eq. (V-49) were changed continuously and still fit the V = 0.25 volts data equally well . . . . . . . . . . . . . . . . . . . . . 70

V-3. The interface-state densities $N_{SS}$ (states/eV-cm$^2$) for different energies E (eV) relative to the valence-band edge for Si-58 at room temperature . . . . . . . 71

V-4. The valence-band tail response time $\tau_v$(mS) of Si-58 at room temperature for different applied bias voltages and light intensities . . . . . . . . . . . . 72

V-5. The parameters that result from fitting $\tau_v$ to Eqs. (V-55) and (V-56). $\chi^2$ is the coefficient of determination for the least squares fit. The $\psi_s$ values are those found from the quasistatic measurement in the no-filter case. 73

VI-1. Summary of the general character of the samples investigated in some detail . . . . . . . . . . . . . . . 92

VI-2. The valence-band tail response time $\tau_v$ of Si-101 at different light intensities . . . . . . . . . . . . 93

FIGURE CAPTIONS

| Figure | | Page |
|---|---|---|
| II-1. | The schematic energy band diagram displaying the relations among various energies . . . . . . . . . . . . . | 12 |
| II-2. | Illustration of how a double boxcar is used to define the rate window. The left-hand side shows capacitance transients at various temperatures, while the right hand side shows the corresponding DLTS signal resulting from using the double boxcar to display the difference between the capacitance at time $t_1$ and the capacitance at time $t_2$ as a function of temperature [Ref. 22] . . . . | 13 |
| IV. | The simplified equivalent circuit when the low-frequency condition is satisfied . . . . . . . . . . . | 35 |
| IV-2. | The capacitance versus voltage measured on Si-58 at room temperature using the quasistatic method (solid curve) with ramp rate 9.04 mV/sec. The four quasi-static capacitance curves were obtained in different light intensities at a wavelength of 0.820 $\mu$m; the largest intensity is 2.12 $\mu W/cm^2$, and the $10^0$, $10^{-1}$, $10^{-2}$ labels are attenuation factors. The dashed curve is the theoretical calculated curve for a sample with 750Å $SiO_2$, carrier concentration $n_b = 2.4 \times 10^{16}$ $cm^{-3}$, and our measured interface state density for Si-58 at room temperature . . . . . . . . . . . . . . . . . . . . | 36 |

Figure | Page

IV-3. The depletion-layer capacitance in the light with no filter as a function of energy E in the band gap relative to the valence-band edge, and surface potential $\Psi_s$. The open circles are data points from Table (V-1) and the curve was calculated from Eq. (IV-3b) with $n_b = 2.4 \times 10^{14}$ cm$^{-3}$. . . . . . . . . . . . . . . . 37

IV-4. The reciprocal of the square of the depletion-layer capacitance $C_d^{-2}$ versus effective surface potential $\Psi_s^* = \Psi_s(V) - \Psi_s(V_0) - kT/e$. The four curves correspond to four different light intensities for Si-58 at room temperature . . . . . . . . . . . . . . . . . . . . . 38

IV-5. The surface potential as a function of applied voltage V for Si-58 at room temperature. Data points are presented for four light intensities: no-filter ($10^0$), $10^{-1}$, $10^{-2}$, and dark, but solid curves are drawn only for the no-filter ($10^0$) and dark cases. . . . . . . . . . . . . . . 39

IV-6. The block diagram of the quasistatic capacitance measurement [Ref. 3] . . . . . . . . . . . . . . . . . . . 40

IV-7. The interface-state density of fluorine peak number one $N_{SS}^{f1}$ in Figure (IV-2) as a function of energy E relative to the valence-band edge. The solid dots are data from the quasistatic capacitance, and the solid and dashed curves are Lorentzian and Gaussian, respectively, chosen to fit the data . . . . . . . . . . . . 41

Figure | Page

IV-8. The interface-state density of fluorine peak number two $N_{ss}^{f2}$ in Figure (IV-2) as a function of energy relative to the valence band edge E. The solid dots are data from the quasistatic capacitance, and the solid and dashed curves are Lorentzian and Gaussian, respectively, chosen to fit the data . . . . . . . . . 42

V-1. The relation and the diagrams of parallel and series equivalent circuits used in the capacitance bridge measurement. . . . . . . . . . . . . . . . . . . . . . . . 74

V-2. The equivalent circuit of the oxide-capacitance $C_0$ in series with the parallel combination of the fast depletion/accumulation capacitance $C_{d/a}$, and the slower interface and inversion layer modeled by capacitance $C_p$ and conductance $G_p$ . . . . . . . . . . . . . . . . . . 75

V-3. The experimental set-up of the conductance method [Ref. 7] 76

V-4. The parallel conductance divided by angular frequency $G_p/\omega$ versus frequency f and energy E relative to the valence-band edge for Si-58 at room temperature. The curves are fits to the data taken in the light intensity P = 2.12μW/cm using Eq. (V-25). Data points are included only for the foremost curve . . . . . . . . . . 77

V-5. The parallel conductance divided by angular frequency $G_p/\omega$ versus frequency f and energy E relative to the valence-band edge for Si-58 at room temperatures. The

Figure Page

curves are fits to the data taken in the dark using Eq. (V-24). Data points are included only for the foremost curve . . . . . . . . . . . . . . . . . . . . . 78

V-6. The sum of the parallel-capacitance $C_p$ and the depletion-layer-capacitance $C_d$ versus frequency f and energy E relative to the valence-band edge for Si-58 at room temperature. The curves are fits, using Eq. (V-25), to data taken in the no-filter case with $P_0 = 2.12\ \mu W/cm^2$ at wavelength 0.820 $\mu$m. Data points are included only for the foremost curve . . . . . . . 79

V-7. The sum of the parallel-capacitance $C_p$ and the depletion-layer-capacitance $C_d$ versus frequency f and energy E relative to the valence-band edge for Si-58 at room temperature. The solid curves are fits, using Eq. (V-25), to data taken in the dark. Data points are included only for the foremost curve. . . . . . . . . . . . . . . 80

V-8. A more detailed model of the features incorporated into $C_p$ and $G_p$ in Figure (V-2), where the subscripts I, v, c, f1, f2 denote inversion layer, valence-band tail, conduction-band tail, fluorine one, and fluorine two, respectively . . . . . . . . . . . . . . . . . . . . . 81

V-9. The normalized conduction-band tail parallel conductance divided by angular frequency $G_p^c(\omega)/\omega$ and parallel capacitance $C_p^c$ as functions of frequency for

Figure | Page

discrete (dotted curves), continuum (dashed curves), and modified continuum (solid curves) models. The peaks of $G_p^c/\omega$ were adjusted to be in the same frequency ($2 \times 10^3$ Hz). Data points in the dark and in the light were both put on. This figure is associated with Si-58 under no bias at room temperature . 82

V-10. The four components of the measured interface-state density of Si-58 at room temperature, as discussed in Section (V-D-2). The circles and solid diamonds denote results obtained from quasistatic data, while the squares and open diamonds denote results obtained from conductance data . . . . . . . . . . . . . . . . . 83

V-11. The fast time constant $\tau_c$ identified with the conduction-band tails versus energy E relative to the valence-band edge for Si-58 at room temperature. The solid points are data, and the dashed curve is drawn through them. The solid curve is calculated from the SRH-model prediction with $\bar{v} = 10^7$ cm/sec, $\sigma = 1.2 \times 10^{-15}$ cm$^2$, $n_b = 2.4 \times 10^{14}$ cm$^{-3}$. . . . . . 84

VI-1. The three components of the measured interface-state density of Si-58 at 77°K as discussed in Section (VI-A). The solid and open diamonds denote results obtained from quasistatic capacitance measurement, while the solid and open circles denote results from the conductance method 94

Figure | Page

VI-2. The conduction-band tail time constant as a function of the energy relative to the valence-band edge both in the dark and in the light for Si-58 at 77°K . . . . 95

VI-3. The quasistatic capacitance versus voltage measured on Si-101 with ramp rate 10.3 mV/sec in the dark and in the light of $P_0$ = 1.60 $\mu$W/cm and $P_0$ = 16.5 $\mu$W/cm 96

VI-4. The reciprocal of the square of the depletion-layer capacitance $C_d^{-2}$ versus $\Psi_s^* = \Psi_s(V) - \Psi_s(V_0) - \frac{kT}{e}$. The three curves correspond to three different light intensities in Figure (VI-3) . . . . . . . . . . . . . 97

VI-5. The two components of the interface-state density measured on Si-101. The solid diamonds denote results obtained from the quasistatic capacitance measurement. The solid and open circles denote results from the conductance method . . . . . . . . . . . . . . . . . . . 98

VI-6. The conduction-band tail time constants of Si-101 versus energy E relative to the valence-band edge extracted from the conductance method data . . . . . . . . . . . 99

VI-7. The raw quasistatic capacitance versus voltage curves with ramp rate 10.3 mV/sec in the dark and in the light for Si-107 . . . . . . . . . . . . . . . . . . . 100

VI-8. The total interface state density versus energy E extracted from the curve in the light in Figure (VI-7) 101

| Figure | | Page |
|---|---|---|


VI-9. Time constants of Si-107 determined from the $G_p(\omega)/\omega$ peak positions as a function of energy E, as predicted by SRH model . . . . . . . . . . . . . . . . . . . . . 102

VII-1. The imaginary part of the scattering-induced self energy as a function of energy E in the band gap relative to the valence-band edge. Solid circles and squares are derived from conduction- and valence-band-tail data for Si-58 at 77°K, respectively. And open circles and squares are derived from conduction- and valence-band-tail data at room temperature, respectively . . . . . . . . . . . . . . . . . . . . . . . . 115

VII-2. The imaginary part of the scattering-induced self energy as a function of energy E in the band gap relative to the valence-band edge. Circles and squares are derived from conduction- and valence-band-tail data for Si-101 respectively . . . . . . . . . 116

ABSTRACT

Silicon is the heart of modern semiconductor devices. The dominance of Si in semiconductor technology depends on the superior quality and properties of thermally grown $SiO_2$ compared with the oxide that can be placed on any other semiconductor. For this reason, $Si-SiO_2$ interface has been an interesting and important research subject for many years.

The well established quasistatic and conductance methods used in the study of the $Si-SiO_2$ interface are improved by using (i) an effectively thin composite insulator, (ii) low carrier concentration substrates, and most importantly (iii) low-level illumination at a wavelength that creates electron-hole pairs. Accurate measurements of both the total density of interface states and its major components as a function of energy in the forbidden gap have been made over four decades ($10^{10}$ - $10^{14}$ states/eV-$cm^2$) due to items (i) and (ii). Item (iii) decreases the response time of the slow states (those in the lower half of the band gap for n-type samples), so the quasistatic condition is well satisfied and the conductance method can be used to study the interface states throughout the band gap on a single sample. Without illumination, the quasistatic condition is not satisfied even for ramp rates on the lower side of those used previously and complementary n- and p-type samples are needed for the conductance method.

The samples investigated have a thermally grown oxide prepared in dry oxygen. They were never exposed to $H_2$ or $H_2O$ at an elevated temperature. We speculate that this processing provides an abrupt $Si-SiO_2$ interface. The composite gate insulator was completed by having an e-gun deposited 250Å layer of $LaF_3$. The resulting interface, subjected to the improved experimental method, yields a wealth of distinctive structure rather than the often-reported featureless U-shaped interface-state density.

# IMPROVED CHARACTERIZATION OF $Si-SiO_2$ INTERFACES

# I. INTRODUCTION

It is well known that impurities and defects can introduce states in the forbidden energy gap of semiconductors. The energy levels at the interfaces of a semiconductor with vacuum, an insulator, or a metal, are strongly perturbed from those in bulk crystals, and they are called "interface states". The ones in the forbidden band gap are the most interesting because they can capture and emit electrons as their energy levels pass the Fermi level due to the applied bias voltage. These states affect the performance of devices.[1] In general, they are almost always deleterious. Structures involving silicon and silicon-dioxide are the foundation of modern semiconductor technology.

Even for the interface between silicon and thermally grown silicon-dioxide, which is the most predictable and generally the best quality of those investigated to date, is not completely understood. This paper describes a refined experimental method to study the properties of silicon and silicon-dioxide interfaces. This experimental method and the accompanying theory can also be applied to the properties of other interfaces.

In the past twenty years, a host of methods[2-4] has been devised to investigate the interface-state properties of semiconductors with vacuum,[3,5,6] insulators,[3,4,7] and metals.[2,3] The most productive of these methods are photoemission spectroscopy[3,5,6] and various electrical

impedance measurements.[2-4,7] Photoemission spectroscopy offers comparatively low-resolution state-density information, but it extends over the entire energy range for which there are filled states. This method yields state densities for cleaved semiconductor to vacuum surfaces, and for surfaces with fractional monolayers of oxygen and other impurities. The impedance measurements fall into several broad classes. They all tend to yield moderately high-resolution interface information but only about states with energies lying in the band gap of the bulk semiconductor.

Dozens of experimental methods have been devised to deduce interface-state densities and time constants from impedance measurements.[2,3,7-] Because of their simple structure and advanced planar technology, MIS-C (metal-insulator-semiconductor-capacitors) are most widely used to investigate interfaces. The two techniques which have yielded the most information on such interface states are the quasistatic and the conductance methods. In the quasistatic method the variation of the ultra-low frequency capacitance is measured as a function of the gate voltage. The conductance method consists of measuring the frequency dependence of the conductance for different gate voltages.

Better data is needed in order to verify theoretical predictions, discriminate among different theories, and modify the theories. Three modifications are incorporated here into the quasistatic and conductance methods to improve these techniques. The first is the use of a composite insulator consisting of thin $SiO_2$ followed by 250Å of $LaF_3$. The $LaF_3$ has such a large capacitance[10] ($> 1\ \mu f/cm^2$) that the composite insulator

capacitance $C_0$ is almost entirely due to the $SiO_2$, yet the composite insulator has far lower leakage current than 250Å of $SiO_2$. Second, a low-bulk carrier concentration substrate is used to reduce the depletion-layer capacitance. Third, low-intensity light at wavelength $\lambda = 0.820\,\mu m$ is shone at normal incidence on the transparent front Au surface of a depleted MIS-C structure. Others[11] have incorporated illumination in the study of MIS structures, but usually for different purposes and at much higher intensities. We use the light to create electron-hole pairs in the space-charge region. The electrons in this n-type material are driven to the back of the depletion layer by the space-charge fields, while the holes are driven to the interface. The light-generated electrons and holes reduce the response time of any inversion layer present, and of the interface states adjacent to the valence band edge.[3] The reduction of these time constants makes it easier to satisfy the low-frequency condition[9] in the quasistatic measurement, and it raises the characteristic frequency of their conductance ($G_p/\omega$) peaks into a range ($>$ 20 Hz) where they can be easily observed. The net result of these three modifications is to increase the dynamic range of interface-state measurements from the usual two decades[3] to over four decades. The more accurate conductance method can be used over the whole band gap, and since the low frequency condition[9] is easily satisfied with the illumination, the voltage dependence of the surface potential is properly determined.

Several of the most important methods used to investigate interface states are reviewed in Section II. The quality and properties of

interfaces depend sensitively on the sample preparation process. For devices a low interface-state density is ordinarily sought. This is usually achieved by adding hydrogen to the interface either by growing the oxide in steam or by annealing the sample in $H_2$ as a post deposition treatment. Our samples were prepared without hydrogen so the nature of the uncontaminated $Si/SiO_2$ interface could be studied. In addition the $SiO_2$ layer is thin, and it is likely that the transition between the Si and the $SiO_2$ is also more abrupt than those for thicker oxides. The details of the sample preparation procedure are discussed in Section III.

Section IV is devoted to the quasistatic measurement, with and without light. We found it is almost impossible to satisfy the quasistatic condition without shining light on the sample. The kinds of errors that are introduced into the density of states and the surface potentials by not satisfying the quasistatic condition are presented. In addition, the properties of two sharp lines due to fluorine at the interface will be examined in Section IV,C.

The conductance method is treated in Section V. Different physical models are critically reviewed and special attention is paid to the shape of the experimental $G_p/\omega$ and $C_p$ versus frequency curves. It is demonstrated that the curves do not exactly fit either the discrete-level or the continuum model curves.[3] A major approximation in the derivation[12,13] of the continuum-model expressions is that the capture cross sections and the state densities vary little over an energy range of order kT about the Fermi level.[6] Neither of these conditions appears to be well satisfied, and when the complete expressions are used in place of the approximate

ones, the theory more closely reproduces the experimental results. Most of our samples exhibit little flat band voltage shift due to positive fixed charge and there is no indication of statistical broadening.[7] However, in samples with positive fixed charges statistical broadening is also present. Consequently, studies of this phenomenon are reported in Sections V, B and D.

Under illumination the conductance method allows the fast and slow interface states to be resolved into separate components. The energy and light variation of the interface state response times is treated in Section V.D. For most samples, the fast time constants do not behave in the manner predicted by the normal Shockly-Reed-Hall (SRH) model.[14] A modification of the model is suggested by the experimental data. The only sample satisfying the SRH model is the one exhibiting statistical broadening.

Data on several samples is presented in Section VI. Although there is a large amount of experimetnal data, the theoretical understanding of the interface between insulators and semiconductors is still rather poor. A tentative interpretation of the observed interface-state densities suggested by our data is that they are scattering-induced band tails of surface valence and conduction bands. Given this interpretation, we can deduce the imaginary part of the valence band $\Delta_v$ and conduction band $\Delta_c$ self energies from the observations. These quantities are presented in Section VII. Finally, Section VIII is devoted to concluding remarks.

## II. PRINCIPAL FEATURES OF THE EXPERIMENTAL METHODS

Numerous experimental methods have been devised to investigate semiconductor insulator interface state properties. The more important ones are reviewed here and their principal features are identified.

### A. Quasistatic method [Refs. 15-17 and discussed in detail in Sect. IV]

Using this method the total capacitance including the interface capacitance and space charge capacitance, and the dependence of the surface potential on applied voltage can be obtained[7,18] relatively simply over a large part of the energy gap. However, no direct information is provided on the nature of these states.

### B. Conductance method [Ref. 7 and discussed in detail in Section V]

In this method both the interface state density and the rate of charge exchange (usually in the form of a time constant) with the bulk energy bands can be determined. It is possible in principle, therefore, to separate the total density of states into component parts, each identified by a characteristic time constant and, quite likely, a different physical origin. However, the normal conductance method can only detect so-called "fast" interface states, such that in _n_-type (_p_-type) material the time constants of states in the lower (upper) half of the band gap are usually too long to be observed. Thus complementary _n_- and _p_-type samples are required to examine the entire band gap, an obvious disadvantage.

C. Capacitance-Voltage (C-V) method

This method was first suggested in 1962 by Terman[19] and also explained by Sze[2] and Goetzberger[3]. In the C-V method, the high frequency ( $\omega\tau \gg 1$) capacitance variation of the MIS structure is measured as a function of bias voltage at a fixed temperature. The existance of interface states causes a shift $\Delta V$ of the high frequency ideal, space charge (without inversion) associated MIS capacitance curve along the voltage axis. The additional charge $\Delta Q_{ss}$ stored in the interface states is determined from the voltage shift across the insulator capacitance:

$$\Delta Q_{ss} = C_o \cdot \Delta V \quad . \tag{II-1}$$

Then the interface state density is given by

$$N_{ss} = \frac{1}{e\,A}\,\frac{d\,Q_{ss}}{d\,\Psi_s} \tag{II-2}$$

where $\Psi_s$ is the semiconductor surface potential (Fig. II-1) and A is the area of the front metal plate. This method provides a quick way to examine the general character of a sample but does not give accurate quantitative information.

Another method, which is similar to Terman's method that we have just discussed, varies the temperature to shift the Fermi level.[20] The gate voltage, which changes as charge is thermally excited out of the interface states, is adjusted to maintain the flat band condition (i.e., so that the conduction and valence bands approached the interface with zero

slope). The charge $\Delta Q_{ss}$ leaving the interface states as they cross the Fermi level is given by

$$\Delta Q_{ss} = C_o \left( \frac{\Delta E_F}{e} + \Delta V \right) \tag{II-3}$$

where $\Delta E_F$ is the temperature induced shift of the Fermi level and $\Delta V$ is the shift in the voltage to maintain the flat band condition. Therefore the interface state density is

$$N_{ss} = \frac{1}{A} \frac{d Q_{ss}}{d E_F} \quad . \tag{II-4}$$

This data reduction method assumes that the metal work function and the electron affinity of the semiconductor are temperature independent, approximations that are somewhat doubtful. Also, it is assumed that the interface state density varies slowly over small energy ranges in the forbidden gap. This condition is not well satisfied especially near the band edges.[21]

Gray and Brown observed maxima near the conduction and valence band edges which are probably an artifact arising from the use of a low ac frequency (150 KHz). Much higher frequency is required if $Q_{ss}$ is not to contribute to the capacitance. Ours, and other recently reported data, show there is no maxima near the band edges.

D. Deep level transient spectroscopy (DLTS)

Lang first proposed the DLTS method and applied it to the study of bulk traps in semiconductors.[22] A collection of other transient methods

is reviewed by Sah.[23] DLTS was first applied to interface states in MIS-capacitors by Yamasaki, et al.[24] In this method a sequence of electrical voltage pulses is applied to an MIS-capacitor. Suppose for definiteness that it is n-type. In the quiescent state the substrate surface is kept in depletion by a d.c. gate voltage $V_a$. At $t = -t_0$, an additional positive voltage pulse of amplitude $V_b$ is applied to the MIS-capacitor that temporarily drives the surface of the substrate into accumulation or weak depletion, then it drops back to the quiescent value. This causes some interface states and bulk traps to cross the Fermi level and become filled by electrons. When the energy bands return to the quiescent state, those electrons above the Fermi level are emitted from the interface states and bulk traps into the conduction band with characteristic emission rates. Throughout this process the changes of the capacitance are monitored. The characteristic emission rate $e_n$ depends exponentially on temperature

$$e_n = n_b \sigma_n \bar{v} \exp\left( e\psi_s / kT \right) \quad , \qquad \text{(II-5)}$$

where $n_b$ is the bulk carrier concentration in the conduction band, $\bar{v}$ is the rms thermal velocity of electrons in the Si bulk, $\sigma_n$ is the electron-capture cross section, and $\psi_s$ is the surface potential.

This experimental procedure is repeated while the sample is subjected to a thermal scan. This results in the capacitance transients shown schematically in Fig. (II-2). The capacitance difference measured with a dual channel boxcar integrator $c(t_1) - c(t_2)$ at sampling times $t_1$ and $t_2$ goes through a maximum at temperature $T_{max}$. The maximum occurs

when the emission time constant approximately equals the sampling window $t_2 - t_1$. The emission rate is related to the sampling times through the equation,

$$e_n = \ln(t_2/t_1)/(t_2 - t_1) \quad \text{(II-6)}$$

Assuming the interface state capacitance is much smaller than the insulator capacitance $C_0$ and varies slowly with energy, the interface state density at maximum capacitance change is

$$N_{ss}(\xi^*) = \frac{-C_0[C(t_1) - C(t_2)]\, \epsilon N_D(W)}{C^3(t_1) \cdot kT \cdot \ln(t_2/t_1)} \quad \text{(II-7)}$$

where $\xi^*$ is the energy corresponding to the maximum capacitance change and $N_D(W)$ is the shallow donor density at depletion layer depth W. One of the major advantages of the DLTS method is that it measures dynamic interface properties directly in a way not affected by surface potential fluctuations, so time constants can be accurately determined.

E. Elevated temperature method

Cooper and Schwartz[25] tried to shorten the time constants of the slow interface states by elevating the temperature of samples so they could study the lower half of the band gap for n-type samples. The measurable energy range includes weak inversion and depletion ($0.302$ eV $< E < 0.704$ eV). However, their sensitivity is low. The range of interface state densities covered by their measurement extends over only about one decade.

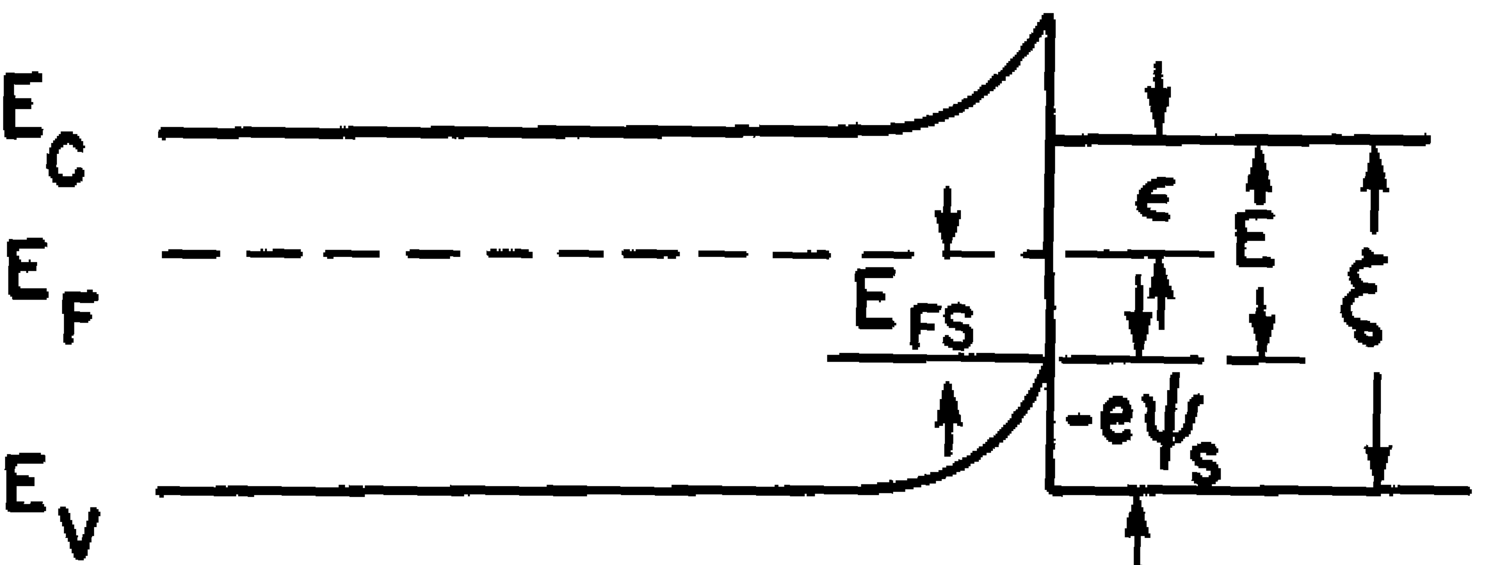


Fig. II-1

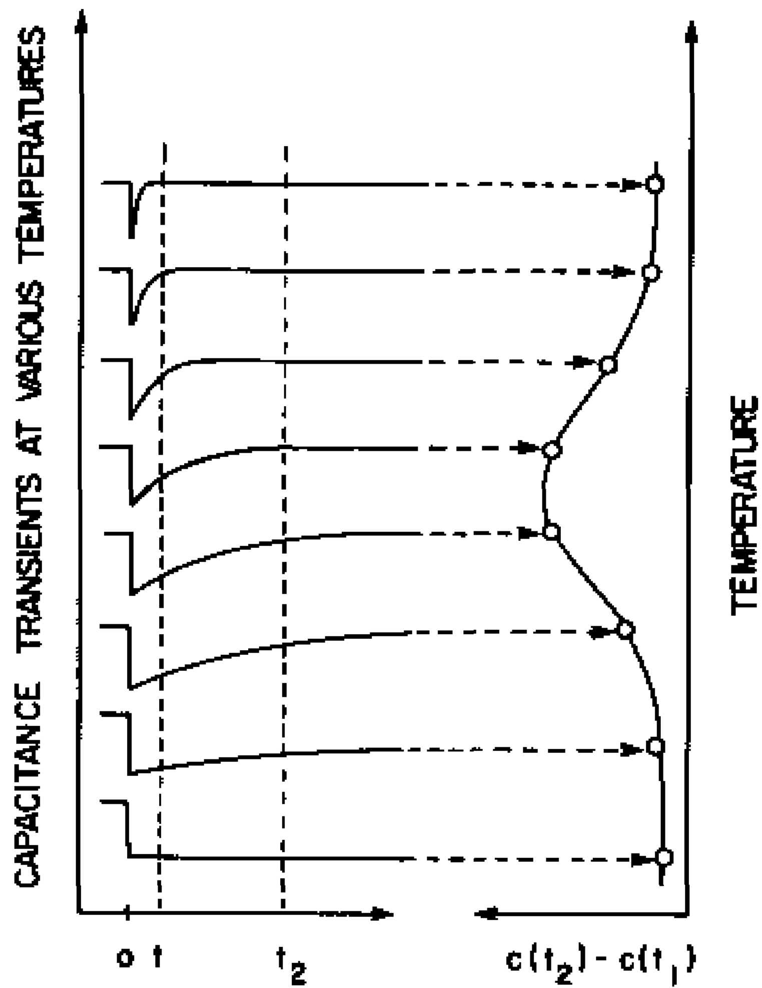


Fig. II-2

## III. SAMPLE PREPARATION

Samples are prepared on low carrier concentration n-type substrates which are 300 $\mu$m thick. The insulators are composites consisting of thin $SiO_2$ layers followed by 250Å of $LaF_3$. The thin $SiO_2$ layers were thermally grown in dry $O_2$ at 1150°C with no exposure to hydrogen or water vapor at elevated temperatures. The $SiO_2$ layers were followed by 250Å e-gun deposited $LaF_3$ films. The $LaF_3$ film possesses very thin dipole layers at its surfaces which produce large capacitances coupled by the ionic conductivity of the material. In these MIS structures, the composite insulator also acts as a blocking contact to electronic conduction as long as the breakdown voltage of the device is not exceeded. The effective capacitance of the $LaF_3$ film is independent of the actual thickness as long as the measurement frequency lies below a characteristic value corresponding to the RC time constant of the $LaF_3$. For a typical 250Å film at room temperature, we have established that the characteristic frequency is well above 100 KHz. At high enough frequencies, or at low enough temperatures where the ionic conduction ceases, the capacitance of $LaF_3$ film is expected to decrease to its geometrical value.[18] For sample Si-58 at room temperature, the measured net insulator capacitance $C_0 = 139\ nF/cm^2$. Assuming that the dielectric constant for $SiO_2$ is 3.9, the theoretical capacitance of a 250Å layer of $SiO_2$ is 138 $nF/cm^2$. Hence the net insulator capacitance arises totally from the $SiO_2$ layer. Since the dielectric

constant of $SiO_2$ is a weak function of the impurity $H_2O$ and OH content, the oxide fabrication method, and the frequency, the real $SiO_2$ dielectric constant of this sample may differ slightly from 3.9. At the beginning of growth, the oxide thickness increases linearly with time. Then the growth process slows and the thickness increases as the square root of time. Thus the oxide may change character depending on whether it is grown directly to the thickness needed, or grown too thick and then etched to the final thickness. Both types of oxides are treated in this study. These observations may account for some of the differences found among the oxides.

Table III-1. Insulator capacitance $C_0$ measured on Si-58 using the quasistatic method at three temperatures.

| T [°K] | 77 | 195 | 295 |
|---|---|---|---|
| $C_0$ [nF/cm$^2$] | 120 | 132 | 139 |

Table III-1 shows that $LaF_3$ is still an ionic conductor at 77°K but the capacitance is reduced when the temperature is lowered. The effective capacitance of the $LaF_3$ layer at 77°K, assuming that the oxide capacitance is temperature independent, is 880 nF/cm$^2$. This is still very large.

The back contact of the MIS structure consists of an e-gun deposited Al film which is then sintered onto the surface at the Si-Al eutectic temperature 550°C, in flowing $N_2$ gas for 10 minutes. When this

back contact is made properly it acts as an ohmic contact. If there is a finite series resistance introduced by the back contact it will cause an extra high frequency peak in the $G_p/\omega$ versus f curve. No such peak is observed in well prepared samples. The metal plate on the front surface is a 125Å thick e-gun deposited Au film. The light transmission coefficient of Au film is greater than 50%. Finally, we anneal the sample in flowing $N_2$ at 400°C for 20 minutes.

We observed several improvements of the sample after annealing:

1. In the quasistatic measurement, because the interface state density decreases, the ratio of $C_{max}$ to $C_{min}$ (maximum and minimum capacitance of the capacitance curve) increases after annealing. For example, Si-96 (70Å $SiO_2$/250Å $LaF_3$) has $C_{max}/C_{min}$ approximately 2.5 and 5 before and after annealing, respectively. This sample is an extreme case.
2. Positive fixed charges are reduced because we observe the capacitance curve shift along the voltage axis. For Si-77 (250Å $SiO_2$/250Å $LaF_3$) before annealing, the flat band voltage is V = 1.5V. After annealing, the flat-band voltage moves to 0.0V. The decrease in the interface state density noted in item one may also be a consequence of the reduction of the fixed charge.
3. In general, the leakage current decreases after annealing.

After the samples were prepared, they were kept in a dry box to avoid drifts that others have reported to be connected with humidity. The stability of most of our samples was quite good.

A detailed step-by-step sample preparation procedure is listed in Table (III-2). This was the standard preparation procedure except Step 3 was applied only if the oxide was too thick. The oxide thickness and its index of refraction were measured with an Ellipsometer. The uncertainty is $\sim 1\%$.

Table III-2

The wafers were n-type phosphorous doped ⟨100⟩ or ⟨110⟩ oriented samples, with resistivity $\rho$ = 100 $\Omega\cdot$cm, and thickness 300 $\mu$m.

1. Wafer cleaning procedures:
   a. $H_2O$ rinse, 5 minutes
   b. $H_2SO_4$:$H_2O_2$ (2:1)etch, 5 minutes
   c. $H_2O$ rinse, 10 minutes
   d. Blow dry with $N_2$ gas
2. $SiO_2$ growth procedures:
   a. $N_2$, 5 minutes
   b. Dry $O_2$ at 1150°C for t minutes (4 minutes to grow 450Å)
   c. $N_2$, 10 minutes
3. $SiO_2$ etching procedure: (when required)
   a. HF:$H_2O$ (1:10) for t' minutes (etching rate $\cong$ 10Å/sec)
   b. Methanal rinse, 5 minutes
   c. Running $H_2O$ rinse, 5 minutes
   d. Blow dry with $N_2$
4. Back ohmic contact:
   a. Mask the front surface of the wafer with black wax
   b. Etch away the $SiO_2$ on the back with HF:$H_2O$ (1:1) for $\sim$40 sec
   c. Remove black wax with trichloroethylene
   d. Acetone rinse, 3 minutes
   e. Methanal rinse, 3 minutes
   f. Blow dry with $N_2$

g. Immediately deposit 3000Å Al (e-gun) on the back surface

h. Sinter at 550°C in flowing $N_2$, 10 minutes

i. Dice the wafer into squares of 125 mil each side ( = 0.101 $cm^2$)

5. e-gun deposit $LaF_3$, the thin Au metal plate, and the Cr-Au front contact dot

a. Trichloroethylene, 3 minutes

b. Acetone rinse, 3 minutes

c. Methanal rinse, 3 minutes

d. Blow dry with $N_2$

e. Deposit 250Å $LaF_3$ on the front surface

f. Deposit 0.042 $cm^2$ 125Å Au on top of the $LaF_3$ film

g. Deposit 300Å Cr then 2000Å Au on a corner of the thin Au film as the front contact dot

6. Anneal the sample at 400°C in flowing $N_2$ for 20 minutes.

## IV. QUASISTATIC METHOD

### A. Quasistatic capacitance method

#### 1. The measurement method

In the quasistatic method,[3] a linearly varying voltage with constant ramp rate $\frac{dV}{dt}$ is applied to the sample. The current I(t) charging the sample is then measured. The total capacitance $C_{QS}$ per unit area A is

$$C_{QS} = \frac{I(t)}{A \cdot dV/dt} \tag{IV-1}$$

provided that the ramp rate is slow enough to maintain the sample in thermal equilibrium.

In thermal equilibrium the equivalent circuit simplifies to that shown in Figure (IV-1). If the total (depletion/accumulation plus inversion) space charge capacitance per unit area is denoted by $C_D$, and the total interface state capacitance per unit area is $C^{ss}$, and the insulator capacitance per unit area is $C_0$, then

$$\frac{1}{C_{QS}} = \frac{1}{C_0} + \frac{1}{C^{ss} + C_D} , \tag{IV-2a}$$

so

$$C^{ss} = \frac{C_{QS}\, C_0}{C_0 - C_{QS}} - C_D . \tag{IV-2b}$$

The space charge capacitance can be calculated theoretically by the following equations if we know the surface potential $\psi_s$ and the bulk carrier concentration $n_b$. For p-type substrates, one finds[2]

$$C_D = \frac{\epsilon}{L_{Dp}} \frac{\left| \left[ 1 - e^{-\beta\psi_s} + \frac{n_b}{p_b}\left(e^{\beta\psi_s} - 1\right)\right] \right|}{F_p} , \qquad \text{(IV-3a)}$$

where

$$F_p \equiv \left[ \left( e^{-\beta\psi_s} + \beta\psi_s - 1 \right) + \frac{n_b}{p_b}\left(e^{\beta\psi_s} - \beta\psi_s - 1\right) \right] ,$$

$$L_{Dp} \equiv \left( \frac{2kT\epsilon}{p_b e^2} \right)^{1/2} , \quad \epsilon \text{ is permittivity of silicon}$$

$$\beta \equiv \frac{e}{kT} , \quad k \text{ is Boltzmann's constant}$$

and

$$n_b p_b = n_i^2 .$$

For n-type substrates the expression changes form slightly so

$$C_D = \frac{\epsilon}{L_{Dn}} \frac{\left| \left[ 1 - e^{\beta\psi_s} + \frac{p_b}{n_b}\left(e^{-\beta\psi_s} - 1\right)\right] \right|}{F_n} \qquad \text{(IV-3b)}$$

where

$$F_n \equiv \left[ \frac{p_b}{n_b}\left( e^{-\beta\psi_s} + \beta\psi_s - 1 \right) + \left( e^{\beta\psi_s} - \beta\psi_s - 1 \right) \right]^{1/2} ,$$

$$L_{Dn} \equiv \left( \frac{2kT\epsilon}{n_b e^2} \right) .$$

Hence by measuring $C_0$, $n_b$, and the gate voltage V dependence of $C_{QS}(V)$, and $\psi_s(V)$ one can determine the voltage variation of the total interface state capacitance.

The applicability of this method is limited to structures for which the leakage current remains small with respect to the charging current. In the presence of small leakage currents the charging current is measured relative to the static current-voltage (I-V) curve.

## 2. The quasistatic condition

In the quasistatic measurement, although the ramp rate is a constant, the variation rate of the surface potential $d\psi_s/dt$ is not always a constant. It is larger in depletion and weak inversion than in strong inversion and accumulation (see Figure IV-4). It is the size of $d\psi_s/dt$ that determines whether or not the system is in thermal equilibrium (see Eq. IV-3). The formation of the inversion layer, and the capture and emission of charges by interface states all depend directly on the surface potential. The criterion that the sample remains in thermal equilibrium while V changes (the quasistatic condition) is[8]

$$\beta \tau_{max} \frac{d\psi_s}{dt} \ll 1 \quad , \qquad \text{(IV-4)}$$

where $\tau_{max}$ is the largest response time of any interface state or space-charge capacitance encountered in the measurement and $\beta = e/kT$. At very small applied voltages (-0.1 to 0.1V), $d\psi_s/dt$ is nearly the same as the ramp rate, while $\tau$ is limited by the time constant for the "slow"

valence-band-side interface states. From the conductance measurements for the sample Si-58 discussed later, we have determined that $\tau > 3$ sec for these states in the dark, so that $\beta\tau \cdot d\psi_s/dt \quad 1$ for the slowest ramp rates we could use. In the presence of light, however, $\tau$ is reduced to the millisecond range and the electronic system which is in a light driven steady state follows the ramped gate voltage. We shall denote this arrangement with the phrase "the quasistatic condition is well satisfied".

The variation of the low-frequency capacitance vs. bias voltage is shown in Figure IV-2 for sample Si-58. The different low-frequency curves were all taken at the same ramp rate, 9.04 mV/sec, but with different light intensities $P_0$ at wavelength 0.820 $\mu$m, shone on the front surface. The maximum $P_0$ is 2.12 $\mu W/cm^2$ and the other two were obtained by using neutral density filters of $10^{-1}$ and $10^{-2}$ attenuation. For light intensities up to $\sim$ 10 $\mu W/cm^2$, there is little additional change in the shape of the quasistatic curves from the no-filter (2.12 $\mu W/cm^3$) curve. However, for intensities beyond that, the space-charge distribution begins to be modified by the light intensity, and the shape changes once more.[11]

It is very easy to mistakenly conclude that the quasistatic condition is satisfied when in fact it is not. One is tempted to choose a ramp rate by starting from a typical value reported before[17] and then decrease it until the shape of the capacitance curve becomes independent of the ramp rate.[26] We found that the shape of the $C_{QS}$ curve in the dark was independent of ramp rates between 6 mV/sec and 35 mV/sec. Using this

criterion, we were content with a ramp rate of 9 mV/sec. It was only after we illuminated the sample and observed the narrowing of the quasistatic curve on the long-time-constant (in n-type material), valence-band side of the curve that the inaccuracy of this procedure became apparent. There are evidently large ranges in ramp rate over which the shape of the capacitance voltage curve is constant, but nevertheless for some states the quasistatic condition is not satisfied so they do not respond. This happens because the different major classes of states have time-constant distributions that are separated by many orders of magnitude.

The use of light appears to be an excellent way to test whether or not the quasistatic condition is indeed satisfied. However, slow states whose response times are light-insensitive may still be missed.

### 3. Determination of $C_0$

Features of the quasistatic C-V curve can be understood easily by examining the equivalent circuit in Figure (IV-1). For large negative gate voltages when the sample is in inversion or for large positive voltages when the sample is in accumulation then $C_D \gg C_o$, and Eq. (IV-2a) becomes

$$\frac{1}{C_{QS}} = \frac{1}{C_0} + \frac{1}{C^{SS} + C_D} \longrightarrow \frac{1}{C_0} , \qquad \text{(IV-5)}$$

The value of $C_0$ measured at the high and low voltage extremes will be used. In order to obtain an accurate value for $C_0$ the bias voltage must be extended well into the inversion and accumulation ranges. Hence, good, low-leakage insulators are needed for accurate measurements.

In Figure (IV-2), the apparent $C_0$ is increasing for the curves measured in progressively higher light intensities because except for the no filter case, none satisfy the quasistatic condition. Even for the largest and smallest voltages the effective magnitudes of $C^{ss} + C_D$ in Eq. (IV-5) do not become much larger than $C_0$ until an intense enough light is shown on the sample to satisfy the quasistatic condition.

For comparison to other more typical experiments Figure (IV-2) also shows a theoretical quasistatic curve (dashed) for a sample with a thicker oxide (750Å) and higher carrier concentration $n_b$ ($2.4 \times 10^{16}$ $cm^{-3}$) but with our measured interface state density. This oxide thickness and carrier concentration are commonly used by other experimenters. With this smoother curve it is difficult to pick the correct $C_0$ and there is obviously less resolution.

4. Determination of the surface potential

What has now become the standard way of deducing the surface potential from the low-frequency capacitance was first suggested by Berglund.[27] The applied voltage V is divided between the oxide and the space charge layer. Thus a small change dV is

$$dV = dV_{ox} + d\psi_s \qquad \text{(IV-6)}$$

where $dV_{0x} = dQ/C_0$ is the voltage drop across the oxide and $d\psi_s$ is the change in the surface potential. The quantity dQ is the differential charge transferred to the sample front (insulator side) surface associated with the voltage change dV, so $dQ = C_{QS} \cdot dV$. Combining these equations,

we get the Berglund expression for the relation between the differential surface potential and applied voltage:

$$d\psi_s = \left(1 - \frac{C_{QS}}{C_0}\right) dV \quad . \tag{IV-7a}$$

Integrating along the quasistatic curve we get

$$\psi_s(V) - \psi_s(V_0) = \int_{V_0}^{V} \left[1 - \frac{C_{QS}(V')}{C_0}\right] dV' \quad . \tag{IV-7b}$$

The constant $\psi_s(V_0)$, which is the maximum excursion of the surface potential for $V_0$ sufficiently small, can be determined by either of two methods.

The first method is to compare the measured quasistatic curve with the ideal low-frequency C-V curve. Because the quasistatic measurement yields a thermal equilibrium C-V curve and in strong inversion and accumulation $C_{QS} \cong C_0$, the measured quasistatic curve should coincide with the ideal low-frequency C-V curve both in the strong inversion and accumulation regions. Then one plots $C_{QS}(V)$ as a function of $\psi_s(V) - \psi_s(V_0)$ obtained from the integration in Eq. (IV-7b) and compares the result with the ideal capacitance versus $\psi_s$ curve. The displacement of the ends of the curve along the surface potential axis is the additive constant $\psi_s(V_0)$. In order to get the ideal C-V curve, it is necessary to know the thickness of the oxide (or the insulator capacitance) and the bulk carrier concentration. The uncertainty in the measurement of these parameters makes this method inaccurate.

The more accurate way to determine the constant $\psi_s(V_0)$ is by fitting the observed high-frequency depletion layer capacitance $C_d$ to its theoretical dependence on $\psi_s$ in the large $-\beta\psi_s$ limit. $C_d$ can be experimentally determined by removing $C_0$ from the high frequency capacitance measured with the capacitance bridge. The theoretical expression for the high frequency depletion layer capacitance is found by simply setting the minority carrier concentration to zero in the formula for $C_D$ (Eq. IV-3). The minority carriers in the inversion layer do not respond to a high frequency ac signal.[2] The experiment data points and theoretically calculated curve were shown in Figure (IV-3). Considering an n-type sample, the appropriate expression is:[7]

$$C_d^{-2} = \frac{2kT}{n_b e^2 \epsilon} \left( -1 - \beta\psi_s \right) , \tag{IV-8}$$

where $\epsilon$ is the semiconductor's permittivity, and $\beta \equiv e/kT$. Figure (IV-4) is a plot of $C_d^{-2}$ as a function of $\psi_s^*$

$$\psi_s^* \equiv \psi_s(V) - \psi_s(V_0) + \beta^{-1} . \tag{IV-9}$$

The quantity $\psi_s^*$ is determined from Eqs. (IV-7b) and (IV-9) by numerical integration of the curves in Figure (IV-2). The zero intercept and the slope of the $C_d^{-2}$ curve determine the maximum excursion of the surface potential $\psi_s(V_0)$ and the bulk carrier concentration $n_b$, respectively. Notice that the slopes of the curves for the different light intensities are all the same, but the apparent value of $\psi_s(V_0)$ changes with light intensity.

The bulk carrier concentration can also be determined from the measured resistivity $\rho$ :

$$\rho = \frac{1}{e(\mu_n n_b + \mu_p p_b)} \cong \frac{1}{e \mu_n n_b} \quad \text{for n-type} \quad \text{(IV-10)}$$

where $\mu_n$ and $\mu_p$ are the electron and hole mobilities respectively and $n_b$ and $p_b$ are the bulk densities of electrons and holes respectively. For n-type materials $n_b \gg p_b$ and the equation reduces to the second form in Eq. (IV-10). The resistivity $\rho$ was measured using the four-point probe method. The value of $n_b$ determined this way agrees with the results from the $C_d^{-2}$ plots. Evidently the fact that the correct $n_b$ is measured cannot be used to conclude that the quasistatic condition is satisfied in a given experiment.

The apparent variation of $\psi_s(V_0)$ is another artifact of violating the quasistatic condition. Figure (IV-3) is a plot of the apparent surface potential dependence on applied voltage for the different light intensities. Only the curve for the highest light intensity, the no-filter case labeled $10^0$, corresponds to an instance in which the quasistatic condition is satisfied. The other curves all correspond to an anomalously large range for $\psi_s$. Others[7] have observed $\psi_s$ values that extend over a larger range than is physically possible corresponding to a surface Fermi energy that changes by more than the band gap. These authors ascribe the anomalously large range to "a gross nonuniformity", but the underlying physical phenomenon is never made clear. As we shall demonstrate in Section V, the $G_p/\omega$ vs. frequency curves display no statistical or

other unexpected broadening, so there is no possibility of a gross nonuniformity being present in our samples. Hence we conclude that the features formerly ascribed to gross nonuniformity were instead the result of long-interface-state time constants, so the quasistatis condition was not satisfied in the measurement.

Lowering the temperature increases all the time constants. At 77°K it would be impossible to satisfy the quasistatic condition without the help of illumination. The reports on lower temperature C-V curves all exhibit a tendency to resemble the high frequency curve.[28] Not satisfying the quasistatic condition, these curves do not yield correct surface potential ranges. Our measurement in various light intensities clearly shows that at lower temperature the curve moves to a higher total capacitance if the quasistatic condition is satisfied. The $\psi_s$ range, $\Delta\psi_{smax}$, at three different temperatures is listed in Table (IV-1). Obviously the range of $\psi_s$ never exceeds the band gap energy.

Table IV-1

| T[°K] | $\rho_0$[μW/cm$^2$] | $\Delta\psi_{smax}$[eV] |
|---|---|---|
| 298 | 2.12 | 0.667 |
| 195 | 20.4 | 0.565 |
| 77 | 22.0 | 0.488 |

We shall introduce experimental evidence in Section V that the largest shift of the surface potential caused by the brightest light

used at room temperature is 0.068V, which is small compared to the apparent shift in $\psi_s$ due to the light, Figure (IV-4). Thus if the ramp rate is so large that the quasistatic condition is violated, one would erroneously conclude that the surface Fermi energy

$$E_{FS} = E_F + e\psi_s \qquad \text{(IV-11)}$$

comes closer to the valence-band edge than it actually does. This will distort the energy dependence of the interface state density and give it a smoother U-shaped character than is proper.

The flat band voltage and so the "fixed positive charges"[26] at the interface are almost uneffected by the light. Notice in Figure (IV-4) that while the apparent surface potential excursion decreases as the light intensity is decreased, the flat band voltage changes by only $\sim$ 20 mV. The measured flat band voltage is 0.81V. The work function (to vacuum) difference between the Au front contact and the Al back contact is 0.55V. This work function difference deduced from photoresponse is 0.9V. Hence, the contribution to the flat band voltage from the fixed positive charges lies between 0.26V and -0.09V depending on which work function difference is appropriate in this case. If one ascribes the difference between the observed 0.81V and the vacuum work function difference 0.55V to fixed positive charges $Q_+$, then with the oxide capacitance $C_0$ = 139 nf/cm$^2$, one finds $Q_+ = 3.6 \times 10^{-8}$ coul/cm$^2$, or $3.3 \times 10^{-4}$ charges/surface atom. However, because of the uncertainty in the appropriate work function difference it is possible that there is much less positive fixed charge. To settle this question unambiguously samples should be prepared using the same metal on the front and back contacts.

## B. Apparatus

The apparatus for a quasistatic capacitance measurement is depicted schematically in Figure (IV-6). The voltage ramp generator must be capable of producing linear ramps at rates dV/dt from 1 to 100 mV/sec. Except when the voltage nears the preset limits, dV/dt is constant to better than 1% in our apparatus. A Keithley model 602 electrometer was used as the operational amplifier. The "normal" mode was used to minimize the noise. In order to maintain the sample in thermal equilibrium, a slow ramp rate is preferred. The minimum ramp rate is limited by the signal to noise ratio. We use ramp rates between 5 and 50 mV/sec, with most of the data taken around 10 mV/sec.

## C. Extra features in quasistatic C-V curve

There are two subsidiary peaks in Figure (IV-2) that appear near -0.5 and +0.2V. A hump can be present on the C-V curve if the ramp rate is so high that the sample is driven well away from thermal equilibrium. When the ramp rate is positive for n-type materials the hump is caused by inversion charge effects. A hump caused by this mechanism usually will not appear when a negative ramp rate is applied because the electron mobility is much larger than the hole mobility.[3] We observed these two peaks for both positive and negative ramps. Also, they are revealed by the application of light, a circumstance in which the time constant of the inversion layer is reduced. Thus the peaks we observe do not originate from a failure to satisfy the quasistatic condition.

These two peaks correspond to energies in the Si-$SiO_2$ system where ion-implanted fluorine is known to produce discrete donor levels.[29-31] We therefore ascribe these features to fluorine ions that have diffused from the $LaF_3$ to the interface during the post deposition anneal. For 500Å $SiO_2$ samples these two peaks become so small that we can just barely discern their presence and cannot make an accurate measurement of their density. Apparently the thick oxide prevents most of the fluorine ions from diffusing to the interface.

When the wavelength $\lambda$ of light was increased until the photon energy is smaller than the band gap energy then the two subsidiary peaks disappeared. From this we conclude that the effect of the light is related to the reduction of interface state time constants, rather than a direct photo-excitation of the discrete states.

These two peaks can hardly be noticed in the dark at room temperature. But they are very pronounced at liquid nitrogen temperature (77°K) even without the illumination. Under low illumination ($P_0 = 1.60\ \mu W/cm$ shone on the sample at 77°K both peaks grow. But in more intense light ($P_0 = 16.5\ \mu W/cm^2$), the first peak broadens and is reduced in amplitude. The second peak exhibits the same trend but to a lesser extent. There are two possible causes for this behavior:

1. The light increases the number of holes in the inversion layer and its capacitance can fully respond because its time constant is shortened. The enhanced response of the inversion layer may mask the fluorine line.

2. The fluorine response rate is in some fashion being reduced by the light. The observed light dependent broadening may simply be lifetime broadening. The second peak is broader than the first and so is not affected as much by the light.

These two peaks taken at room temperature are shown on extended scales and plotted against the interface Fermi energy relative to the valence-band edge (see Figures IV-7 and 8). Both peaks have been fit to Lorentzian and Gaussian curves. The parameters of these fits are presented in Table IV-2. Since there is no systematic way to pick the base line for these curves, the shape function cannot be determined with certainty. However, the Gaussian seems to offer a slightly superior fit in both cases. Several features of these curves are noteworthy.

1. The widths of both peaks (especially the one at 0.246 eV) are quite narrow compared to the energy gap.
2. Since the density of surface atoms on the (100) surface is $6.8 \times 10^{14} cm^2$, the area under the peaks (using the Gaussian shape) implies there are $3.3 \times 10^{-5}$ and $1.8 \times 10^{-5}$ fluorines per interface site, respectively, contributing to the first and second peak.
3. For both the Gaussian and Lorentzian shapes, the ratio of the area of peak one to peak two is 1.86.

A systematic study of these features is required to fully understand them.

Table IV-2

| Peak | | | Lorentzian | | Gaussian | |
|---|---|---|---|---|---|---|
| Number | Position (eV) | Height (states/eV-cm$^2$) | Half-width (eV) | Area (states/cm$^2$) | Variance (eV) | Area (states/eV) |
| 1 | 0.2458 | $4.95 \times 10^{12}$ | $2.10 \times 10^{-3}$ | $3.27 \times 10^{10}$ | $1.80 \times 10^{-3}$ | $2.23 \times 10^{10}$ |
| 2 | 0.441 | $2.00 \times 10^{11}$ | $2.80 \times 10^{-2}$ | $1.76 \times 10^{10}$ | $2.40 \times 10^{-2}$ | $1.20 \times 10^{10}$ |

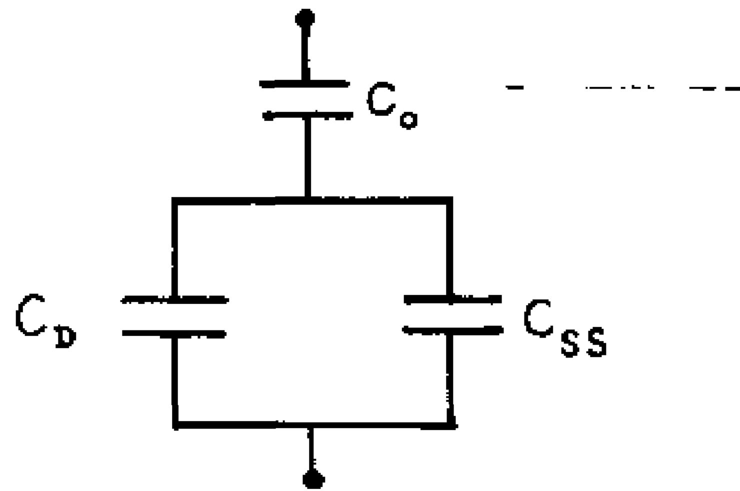


Fig. IV-1

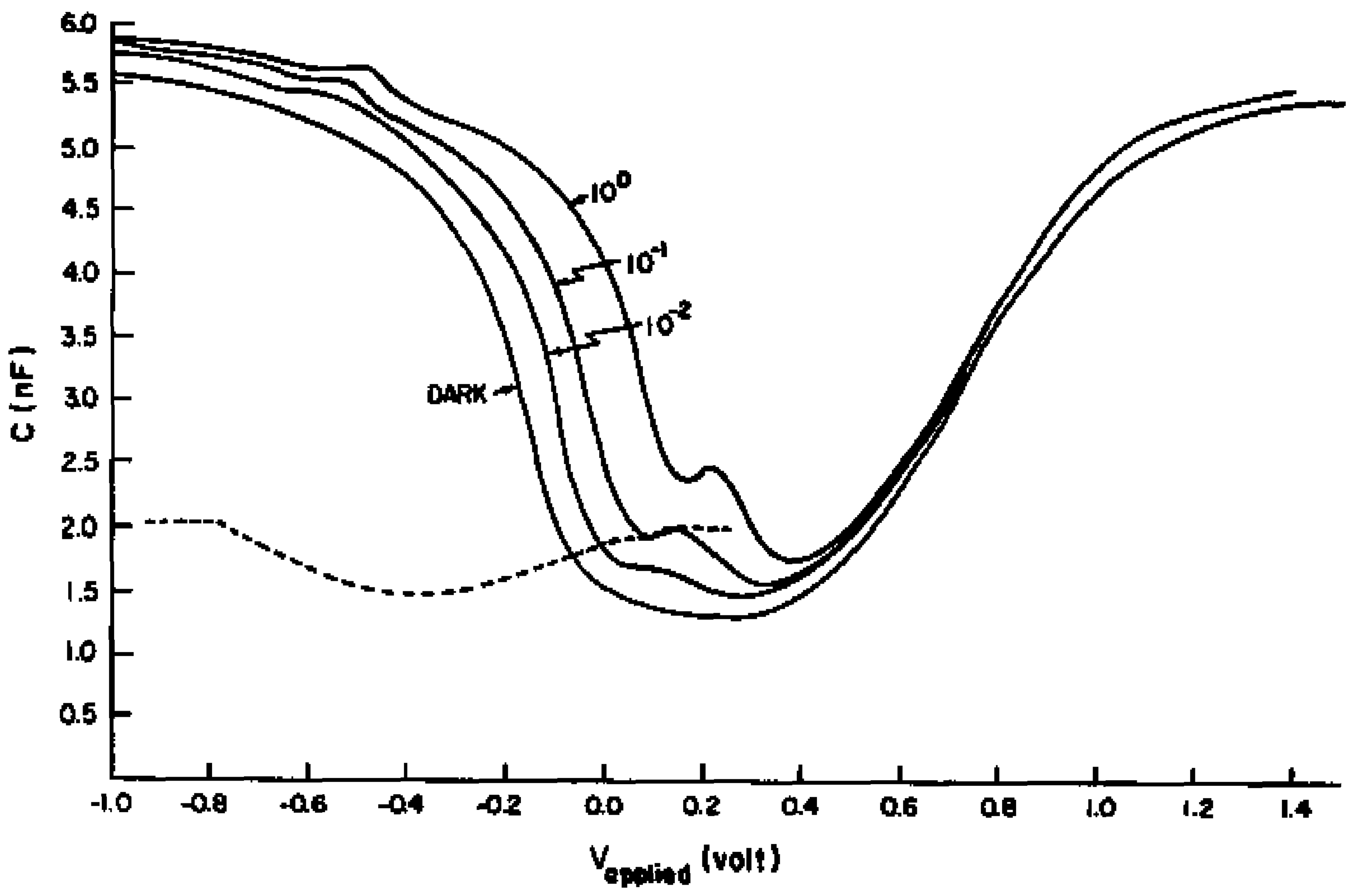


Fig. IV-2

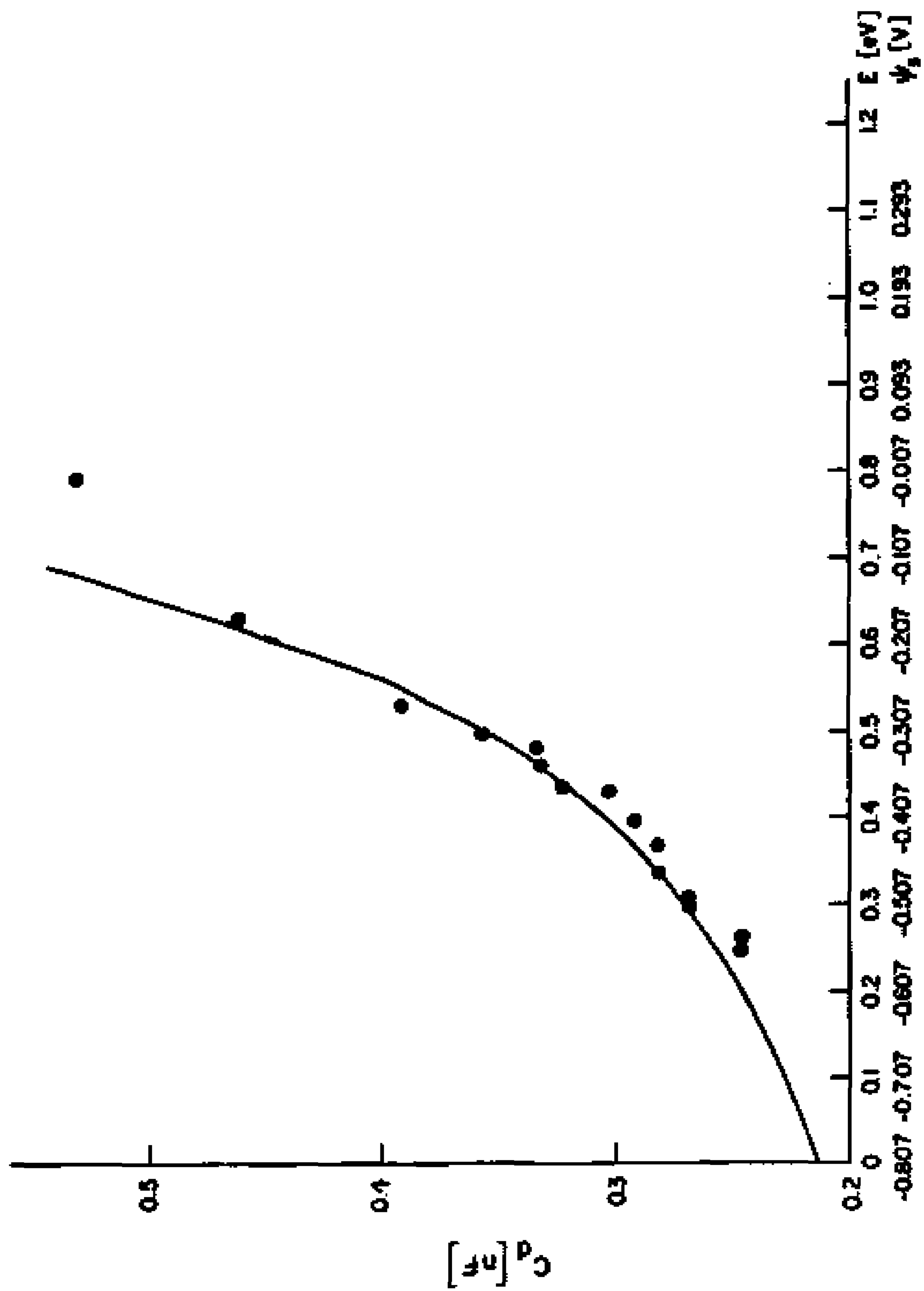


Fig. IV-3

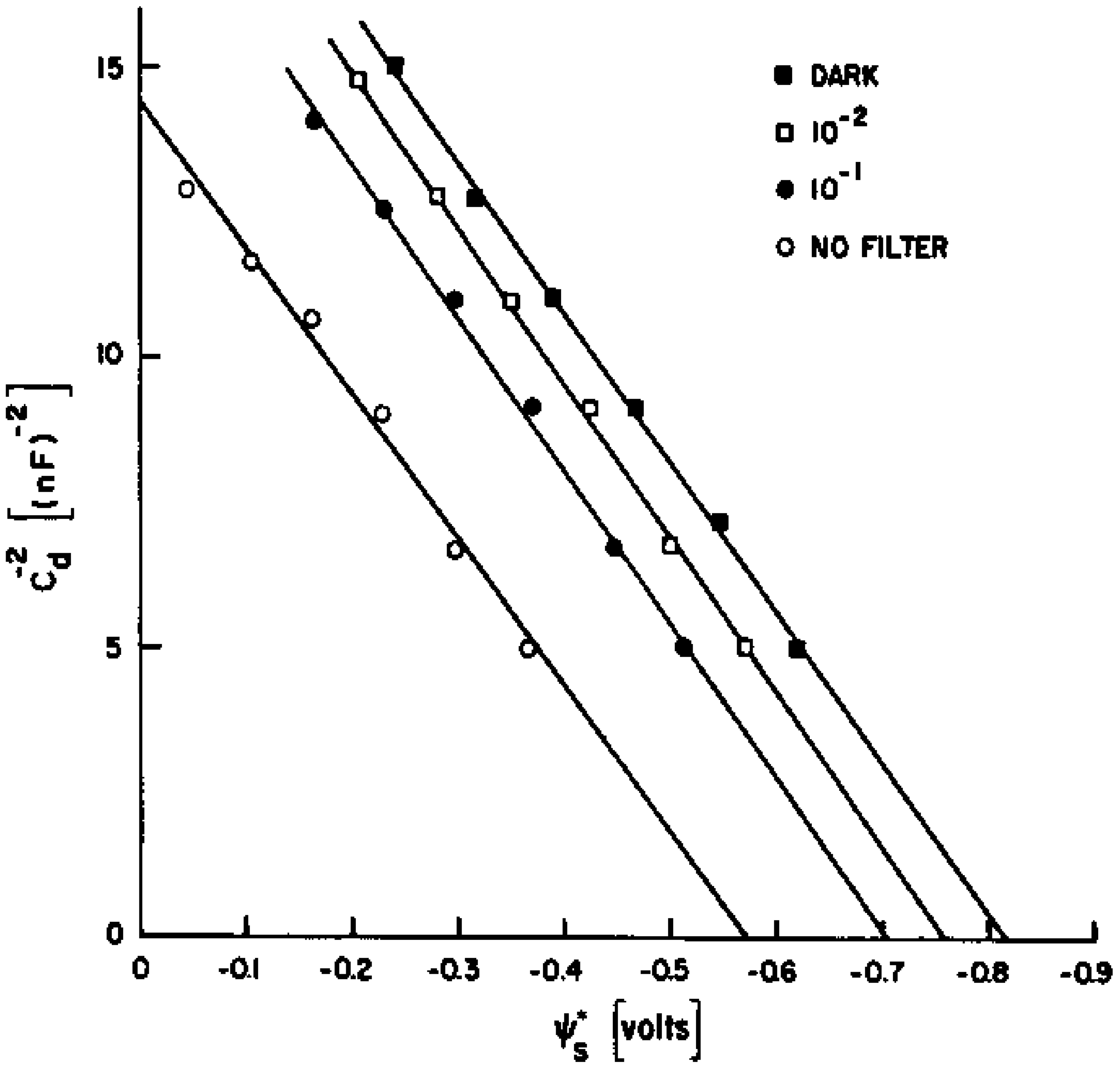


Fig. IV-4

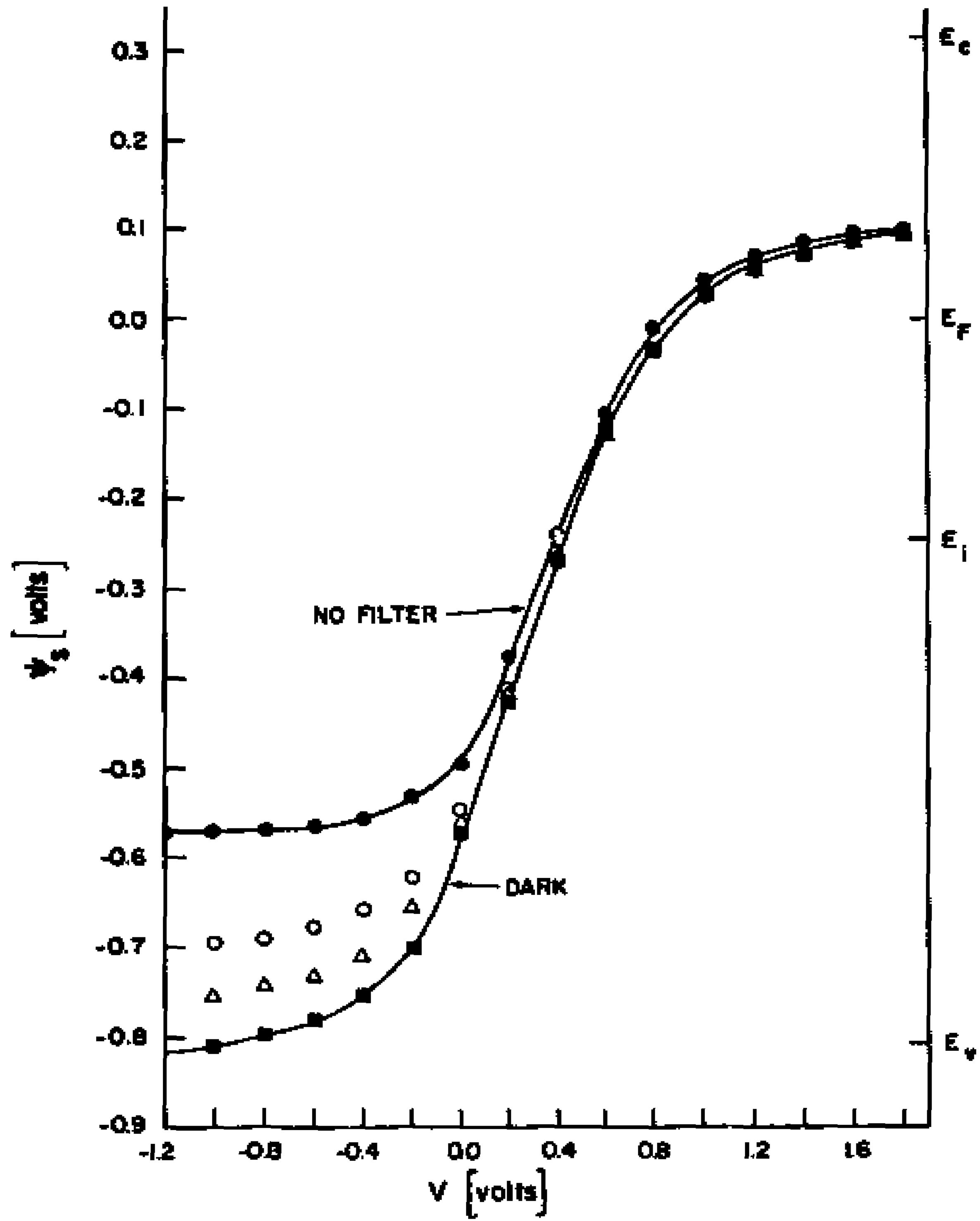


Fig. IV-5

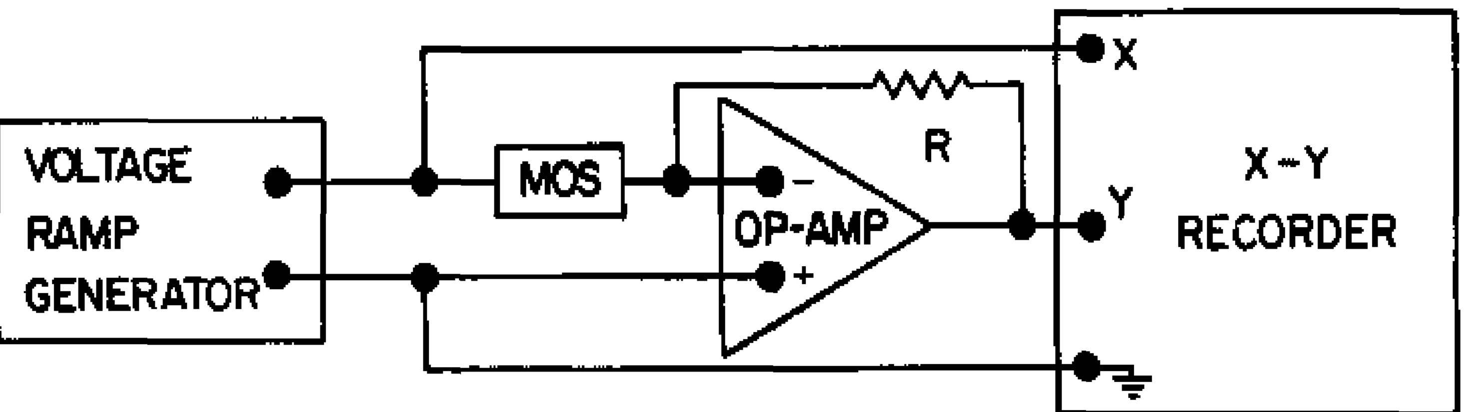


Fig. IV-6

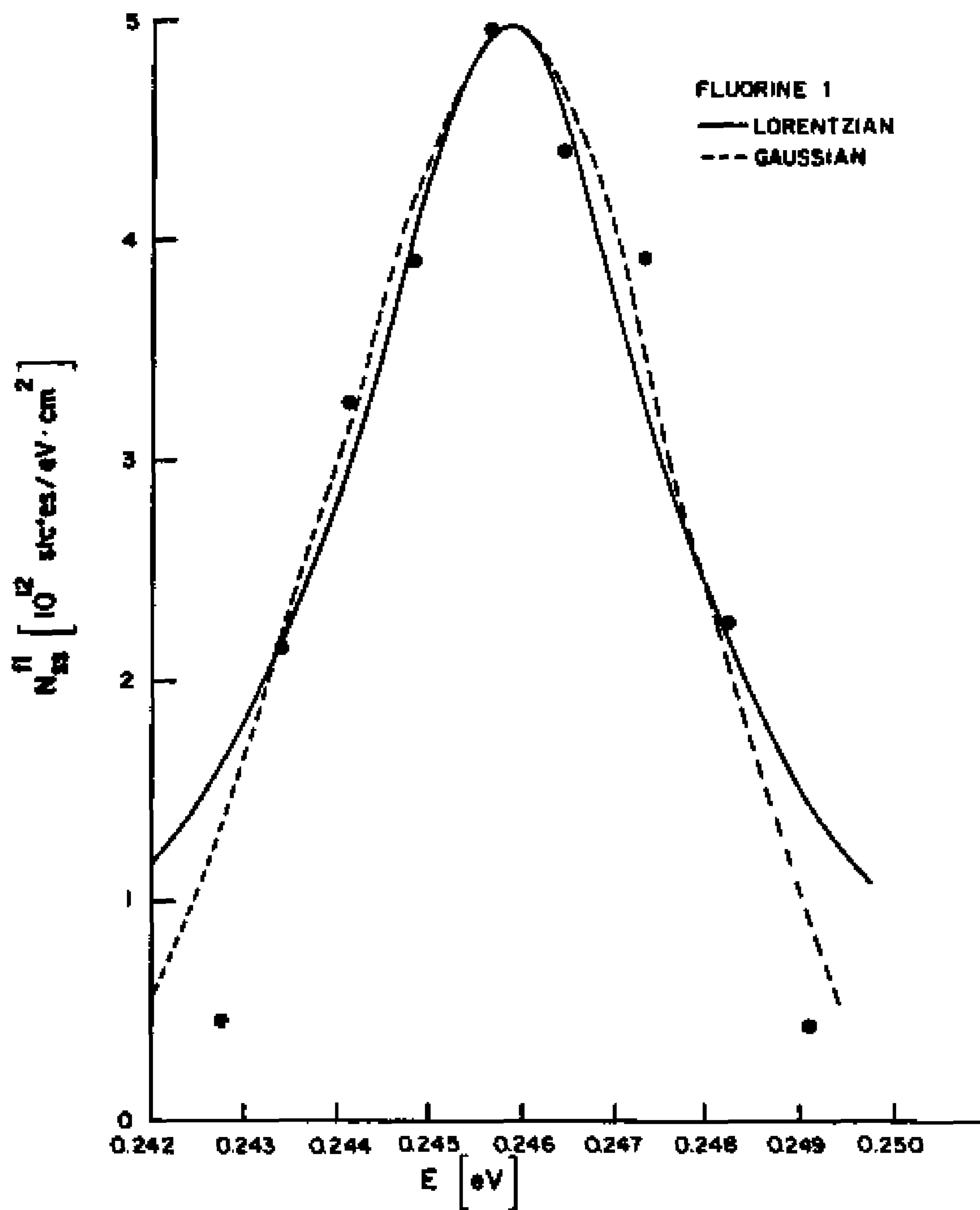


Fig. IV-7

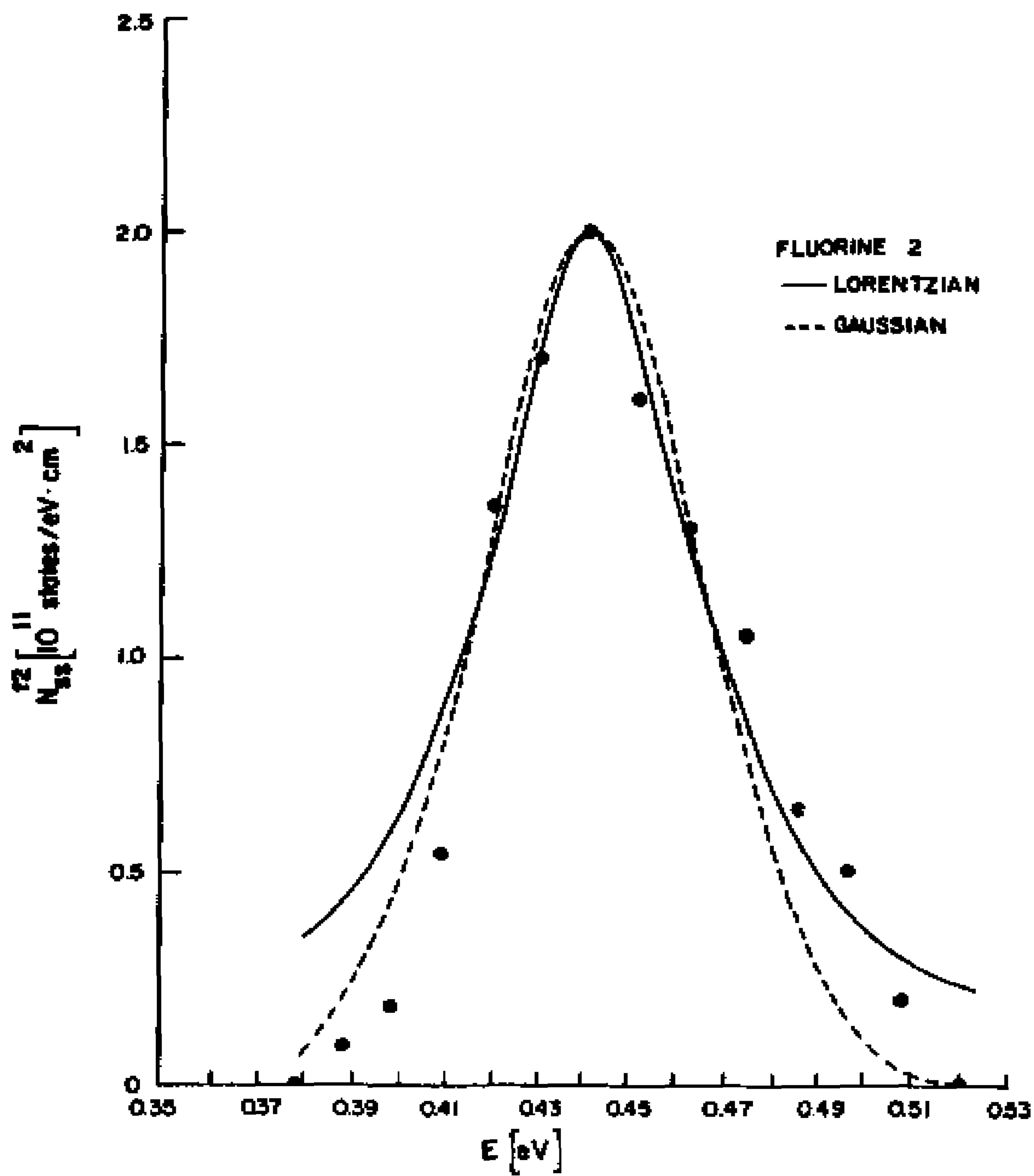


Fig. IV-8

# V. CONDUCTANCE METHOD

## A. The method

This method was devised by Nicollian and Goetzberger.[7] Much more detailed interface state density information, which yields insight into their physical origin, can be obtained when the full frequency range of the MOS capacitance and conductance are measured and analyzed. The data collection and reduction involved in this method is a highly labor-intensive activity, but much more information is revealed.

Normally this method can only be employed conveniently to study the interfaces in accumulation and depletion. Even using both n- and p-type materials in order to cover a larger energy range, very little information is gained on the behavior of interface states in the midgap and inversion regions. Moreover there is no assurance when one uses two samples, one n-type and the other p-type, that their interface state densities are identical. The use of light in our method shortens time constants of the states one encounters in weak to strong inversion, so the interface state profile can be tracked throughout the band gap on the same sample.

The "conductance method"[7] starts by applying a small ac signal to the MOS structure. The real and imaginary parts of the impedance (or the total series-capacitance $C_{ST}$ and dissipation-factor D) are measured as functions of the ac signal frequency for different fixed-bias voltages and temperatures.

The surface potential varies in response to the ac signal causing the interface states to move relative to the Fermi level, so electrons are captured and emitted by interface states. Thus, there is a capacitance $C_{SS}$ associated with the charge stored in the interface states, and the density of interface states $N_{SS}$ is related to $C_{SS}$ by the equation

$$N_{ss} = \frac{C_{ss}}{eA} \quad , \tag{V-1}$$

where e is the charge of an electron and A is the surface area. The response time $\tau$ of electrons being captured or emitted by interface states is related to an effective resistance R by

$$\tau = R C_{ss} \tag{V-2}$$

The interface state capacitance and response time can be extracted from the measurements. A bridge, depending on the magnitudes of the parameters, reads either the total parallel capacitance $C_{PT}$ and total parallel conductance $G_{PT}$, or the total series capacitance $C_{ST}$ and dissipation factor D which is defined as the ratio of the real part of the impedance to imaginary part of the impedance. The relations among these parameters are shown in the insets to Figure (V-1).

From the measured total series capacitance $C_{ST}$ and dissipation factor D we can determine the frequency dependence of $C_p + C_{d/a}$ and $G_p/\omega$ (see Fig. (V-2)) from the expressions:

$$C_p + C_{d/a} = \frac{[1-(C_{ST}/C_o)]}{[1-(C_{ST}/C_o)]^2 + D^2} \quad , \tag{V-3}$$

and

$$\frac{G_p}{\omega} = \frac{C_{ST}\, D}{[1-(C_{ST}/C_0)]^2 + D^2} \qquad (V\text{-}4)$$

In the past, samples were used for which $C_0$ and $C_{d/a}$ were comparable. Then the accuracy of the information deduced from $C_p$ in Eq. (3) was limited because $C_{ST}$ differs from $C_0$ by only a few percent. It is evident from Eq. (4) that $G_p/\omega$ does not suffer as badly from this limitation. Hence most experiments have relied on extracting information from $G_p/\omega$, which accounts for the designation "conductance method". In principle, $G_p/\omega$ and $C_p$, which are connected by the Kramers-Kronig relations, contain the same information. However, there are instances in which the information can be extracted from one more easily than from the other. By fitting the theoretical curves to the data points calculated from Eqs. (V-3) and (V-4), interface state capacitances and time constants can be extracted.

## B. Physical models

The analytical expressions for the frequency variation of $C_p(\omega)$ and $G_p(\omega)/\omega$ depend on the physical model of the interface states. The formulas deduced from different models will be compared against the experimental data. The data is sufficiently accurate so it is possible to discriminate between the models and even to suggest corrections to the standard results.

## 1. Discrete model

Suppose the interface states are made of several components with different physical origins, each designated by an index j. Consider first a collection of single-level interface states and assume that only capture and emission of majority carriers are important. Then for n-type materials with an electron density $n_s(t)$ at the surface at time t, the capture flux of electrons is

$$R_n(t) = \sum_j N_{SS}^j \, C_n^j \left[ 1 - f_j(t) \right] n_s(t) \quad , \tag{V-5}$$

where $C_n^j$ is the net capture coefficient (units $cm^3/sec$) for state j, $N_{SS}^j$ is the number of states per unit area of type j, and $f_j(t)$ is the Fermi function for states j at time t. The emission flux is

$$G_n(t) = \sum_j N_{SS}^j \, e_n^j \, f_j(t) \quad , \tag{V-6}$$

where $e_n^j$ is the emission rate (unit $sec^{-1}$) for states j. The surface current density is

$$i_s(t) = \sum_j \left\{ e N_{SS}^j \, C_n^j \left[ 1 - f_j(t) \right] n_s(t) - e N_{SS}^j e_n^j f_j(t) \right\} . \tag{V-7}$$

Express $f_j(t)$ as the sum of a dc and an ac part

$$f_j(t) = f_{jo} + \delta f_j(t) \quad . \tag{V-8}$$

Similarly one can write

$$n_s(t) = n_{so} + \delta n_s(t) \, . \tag{V-9}$$

Substitute Eqs. (8) and (9) into Eq. (7) and make the small ac signal approximation by keeping only terms linear in $\delta f_j$ and $\delta n_s$ (small signal criterion). Then Eq. (7) becomes

$$i_s(t) = \sum_j e N_{ss}^j C_n^j \left[ (1-f_{jo}) n_{so} + (1-f_{jo}) \delta n_s - n_{so} \delta f_j \right] - e N_{ss}^j e_n^j (f_{jo} + \delta f_j) \quad . \tag{V-10}$$

When only the dc bias is applied, there is zero net current, so

$$e N_{ss}^j C_n^j (1 - f_{jo}) n_{so} = e N_{ss}^j e_n^j f_{jo} \quad . \tag{V-11}$$

Substituting Eq. (11) into Eq. (10) we get

$$i_s(t) = \sum_j e N_{ss}^j C_n^j \left[ (1-f_{jo}) \delta n_s - n_{so} \frac{\delta f_j}{f_{jo}} \right] \quad . \tag{V-12}$$

Since the net current density is

$$i_s(t) = \sum_j e N_{ss}^j \frac{d f_j}{dt} \quad , \tag{V-13}$$

we can equate Eqs. (12) and (13) to get

$$\frac{d f_j}{dt} = C_n^j (1 - f_{jo}) \delta n_s - C_n^j n_{so} \frac{\delta f_j}{f_{jo}} \quad . \tag{V-14}$$

For small signals the variation of Fermi function is

$$\delta f_j = f_{jm} e^{i\omega t} \quad , \tag{V-15}$$

where $f_{jm}$ is the maximum value of the perturbation of the Fermi function for j type states by the ac signal. From Eqs. (8) and (15) we get

$$\frac{d f_j}{dt} = i \omega \delta f_j \quad . \tag{V-16}$$

Next equate Eqs. (14) and (16) and solve for $\delta f_j$.

$$\delta f_j = \frac{f_{j0} ( 1 - f_{j0}) \delta n_s}{n_{s0} ( 1 + i \omega f_{j0} / C_n^j n_{s0})} \quad . \tag{V-17}$$

Combining Eqs. (17) and (16) and substituting into Eq. (13) results in the expression

$$i_s(t) = \sum_j \frac{i \omega e N_{ss}^j f_{j0} (1 - f_{j0}) \delta n_s}{(1 + i \omega f_{j0} / C_n^j n_{s0}) n_{s0}} \quad . \tag{V-18}$$

The instantaneous surface electron density $n_s(t)$, and surface potential $\psi_s(t)$ are related by the expression

$$n_s(t) = n_i \exp \left[ \beta \left( \psi_s(t) - V_B \right) \right] \quad , \tag{V-19}$$

where $n_i$ is the intrinsic carrier concentration and $V_B$ is the potential difference between the mid gap energy and the Fermi level in the bulk. Taking the differential of Eq. (19) gives

$$\frac{\delta n_s}{n_{s0}} = \frac{\frac{e}{kT} n_i \exp \left[ \frac{e}{kT} ( \psi_s - V_B) \right] \delta \psi_s}{n_i \exp \left[ \frac{e}{kT} ( \psi_s - V_B) \right]} = \frac{e}{kT} \delta \psi_s \quad . \tag{V-20}$$

Using Eq. (20), Eq. (18) becomes

$$i_s(t) = \sum_j i \omega \frac{e^2}{kT} \frac{N_{ss}^j f_{j0} (1 - f_{j0}) \delta \psi_s}{(1 + i \omega f_{j0} / C_n^j n_{s0})} \quad . \tag{V-21}$$

This can be written as

$$i_s(t) = \sum_j Y_{ss}^j \, \delta \psi_s = Y_{ss} \, \delta \psi_s \quad , \tag{V-22}$$

where

$$Y_{ss}^j = i\omega \frac{e^2}{kT} \frac{N_{ss}^j f_{j0} (1 - f_{j0})}{(1 + i\omega f_{j0} / C_n^j n_{s0})} \quad . \tag{V-23}$$

$Y_{SS}^j$ is the admittance of a series RC network with capacitance $C_{SS}^j = \frac{e^2}{kT} N_{SS}^j f_{j0} (1 - f_{j0})$ and time constant $\tau_j = \frac{1}{C_n^j n_{s0}}$. This can be converted into a parallel capacitance and a parallel conductance given by the expressions:

$$C_p = \sum_j \frac{C_{ss}^j}{1 + \omega^2 \tau_j^2} \tag{V-24}$$

and

$$\frac{G_p}{\omega} = \sum_j \frac{C_{ss}^j \omega \tau_j}{1 + \omega^2 \tau_j^2} \quad . \tag{V-25}$$

The parameters $C_{SS}^j$, $\tau_j$ in Eqs. (24), (25) can be determined by selecting them to fit all the details of a $G_p(\omega)/\omega$ and $C_p(\omega)$ data set, or if the $G_p/\omega$ curve is a single well resolved line with the proper shape then its peak occurs at a frequency such that $\omega \tau_j = 1$ and the peak height is $C_{SS}^j/2$.

2. Continuum model

It is evident from the shape of the measured interface state densities with energy in the band gap that they vary continuously over

the band gap. Lehovec[12,13] followed by others,[3,7,9] extended the discrete level SRH (Shockly-Reed-Hall) model into what is now called the continuum model. The admittance for the discrete level SRH model given in Eq. (23) is then modified by dividing the sum over discrete states into subclasses. If within a given subclass now labeled j the levels actually form a continuous distribution then the number of states per unit area $N_{SS}^{j}$ is converted into an energy density and the sum is converted to an integral, so $eN_{SS}^{j} \Rightarrow N_{SS}^{j}(\xi)$ where $\xi$ is an interface state energy relative to the valence-band edge in the bulk and $N_{SS}^{j}(\xi)$ is the number of states per unit area per energy (in eV). In this case, an expression for the small-signal admittance per unit area $Y_{SS}^{j}$ associated with a particular class of interface state j has the form

$$Y_{ss}^{j}(\omega) = i\omega \frac{e}{kT} \int_{E_v^s}^{E_c^s} \frac{N_{ss}^{j}(\xi) f_0(\xi)[1-f_0(\varepsilon)]}{1+i\omega \tau_j(\xi) f_0(\varepsilon)} d\varepsilon$$

$$= G_p^{j}(\omega) + i\omega C_p^{j}(\omega) \tag{V-26}$$

where $E_v^s = E_v - e\psi_s$ and $E_c^s = E_g + E_v^s$ are the energies of the valence- and conduction-band edges at the surface relative to the valence-band edge in the bulk, $\varepsilon = \xi - E_F$ is a interface-state energy relative to the Fermi level. The relations among these energies are illustrated in Figure (II-1). The Fermi function for energy $\varepsilon$ is

$$f_0(\varepsilon) = \frac{1}{\exp(\varepsilon/kT) + 1} \tag{V-27}$$

The product

$$f_0 (1 - f_0) = -kT \frac{df_0}{dE} \tag{V-28}$$

is sharply peaked about $E_F$ with width $\sim kT$. This leads to the idea that over the range for $E$ for which $f_0(1 - f_0)$ has a finite value, one could approximate

$$N_{ss}^{j}(\xi) \cong N_{ss}^{j}(E_{FS}) \equiv N_{ssF}^{j} \quad \text{and} \quad \tau_j(\xi) \cong \tau_j(E_{FS}) \equiv \tau_{jF} , \tag{V-29}$$

by constants where $E_{FS} \equiv E_F + e\psi_s$. Doing this generated the continuum-model expressions

$$C_{pc}^{j}(\omega) = \frac{e N_{ssF}^{j}}{\omega \tau_{jF}} \tan^{-1} \omega \tau_{jF} , \tag{V-30}$$

and

$$\frac{G_{pc}^{j}(\omega)}{\omega} = \frac{e N_{ssF}^{j}}{2 \omega \tau_{jF}} \ln \left( 1 + \omega^2 \tau_{jF}^2 \right) . \tag{V-31}$$

States whose time constants follow the SRH model vary as

$$\tau_j^{-1}(\xi) = n_b \sigma_j \bar{v} \exp\left( e\psi_s / kT \right) , \tag{V-32}$$

where $n_b$ is the bulk carrier concentration in the conduction band, $\bar{v}$ is the rms thermal velocity in the bulk, and $\sigma_j(\xi)$ is the electron-capture cross section for the states j. The continuum-model approximation is invalid if the capture cross section varies rapidly with energy $\xi$. As long as it was thought that $N_{SS}$ varied smoothly in a U-shaped curve,

it was reasonable to suppose that the approximation held for $N_{SS}$, but in view of our results (see the next section) it is now evident that the approximation is not satisfied either.

Let us next establish the expressions needed to investigate the consequences of not invoking the continuum-model approximation. Combining Eqs. (26) and (28) leads to the expressions

$$C_p^j(\omega) = e N_{ssF}^j \int_{f_0(E_c^s)}^{f_0(E_v^s)} \left(\frac{N_{ss}^j}{N_{ssF}^j}\right) \frac{df_0}{1+\omega^2\tau_{jF}^2(\tau_j/\tau_{jF})^2 f_0^2} \qquad \text{(V-33)}$$

and

$$\frac{G_p^j(\omega)}{\omega} = e N_{ssF}^j \int_{f_0(E_c^s)}^{f_0(E_v^s)} \left(\frac{N_{ss}^j}{N_{ssF}^j}\right) \frac{\omega\tau_{jF}(\tau_j/\tau_{jF}) f_0\, df_0}{1+\omega^2\tau_{jF}^2(\tau_j/\tau_{jF})^2 f_0^2} . \qquad \text{(V-34)}$$

Once the variation of $N_{SS}^j$ with energy is established in the next section, its functional form can be inserted into Eqs. (33) and (34). Then $C_p^j(\omega)$ and $G_p^j(\omega)/\omega$ found from numerical integration of these equations can be compared against experiment.

### 3. Statistical broadening[7,32]

While this does not occur in Si-58, when certain samples are biased into depletion, they have a broader $G_p/\omega$ peak than that predicted by Eq. (31). This can be explained by assuming there are statistical fluctuations of the surface potential in the plane of the interface due

to the random distribution of fixed charges in the insulator, charged interface states, and ionized acceptors in the space charge region. According to Nicollian and Goetzberger,[7] the fixed built-in charges in the oxide are the main source of the fluctuation in the surface potential. Declerck et al (1974) found their data can be explained only if negative and positive surface charges are both present.[33] It is more widely accepted that Ziegler and Klausmann found no evidence that negative fixed charges are present at the interface.[34] When the sample is in inversion the effect of fluctuations of these fixed positive charges is reduced by the screening due to the conducting inversion layer. When the sample is biased to accumulation, fixed positive charges are again screened. In either case, the effect of the fluctuations caused by the build-in charges is reduced. In general, statistical broadening can be observed only in the depletion region.

For simplicity, only the derivation for the real part of the admittance will be presented. The derivation of the imaginary part is similar. We conceptually divide the plane of the interface into a number of characteristic regions of equal area within which the surface potential is uniform. The number of characteristic regions $d\nu$ which contain between N and N + dN randomly distributed surface charges is

$$d\nu = P(N)\, dN, \tag{V-35}$$

where P(N) is the probability of finding a characteristic region having N randomly distributed surface charges. When the mean number $\bar{N}$ of surface charges is large, P(N) is given by a Gaussian approximation to a

Poisson distribution

$$P(N) = (2\pi \bar{N})^{-\frac{1}{2}} \exp\left[ -(N-\bar{N})^2 / 2\bar{N} \right] \quad . \tag{V-36}$$

This is reasonable for a charge density below $10^{12}$ $cm^{-2}$ where the probability for a charged center to be located at a certain place is independent of the places where other charges are located.[33] Let Q be the density of surface charges, we get

$$N = \alpha Q / e \tag{V-37}$$

where $\alpha$ is the area of each characteristic region. From Eq. (36) and (37) we get

$$P(Q) = (2\pi\alpha \bar{Q}/e)^{-\frac{1}{2}} \left(\frac{\alpha}{e}\right) \exp\left[ -\alpha(Q-\bar{Q})^2 / 2e\bar{Q} \right] , \tag{V-38}$$

where $\bar{Q}$ is the mean of surface charge density Q. The total charge density is

$$Q_T = Q_s + Q_f + Q_{sc} \quad , \tag{V-39}$$

where $Q_s$ is the interface state charge density, $Q_f$ is the fixed charge density in the oxide, and $Q_{sc}$ is the silicon space charge density. The surface charge density is

$$Q = Q_s + Q_f = Q_T - Q_{sc} \quad . \tag{V-40}$$

Since the voltage is distributed across the oxide and the space charge

layer, we have

$$V(t) = V_o + \delta V_o(t) = \psi_s(t) + Q_T/C_o \quad , \qquad \text{(V-41)}$$

where the bias is decomposed into ac and dc parts. The relation between $\psi_s$ and $Q_T$ can be found by examining the dc terms in Eq. (41)

$$(V_o - \psi_s)\, C_o = Q_T \quad . \qquad \text{(V-42)}$$

Substituting $Q_T$ in Eq. (42) into Eq. (40) results in

$$Q = (V_o - \psi_s)\, C_o - Q_{sc} \quad . \qquad \text{(V-43)}$$

Differentiating Eq. (43), it becomes

$$\begin{aligned} -dQ &= C_o\, d\psi_s + C_D\, d\psi_s \\ &= \left( C_o + \frac{\epsilon}{W(\bar{\psi}_s)} \right) d\psi_s \quad , \end{aligned} \qquad \text{(V-44)}$$

where $W(\bar{\psi}_s)$ is the space charge width at the mean surface potential, and $\epsilon$ is the permittivity of silicon. Assuming the fluctuation is small, we can replace $dQ$ and $d\psi_s$ by $(Q - \bar{Q})$ and $(\psi_s - \bar{\psi}_s)$ respectively. That is

$$-(Q - \bar{Q}) = \left( C_o + \frac{\epsilon}{W(\bar{\psi}_s)} \right) \left( \psi_s - \bar{\psi}_s \right) \quad . \qquad \text{(V-45)}$$

Combining Eqs. (38), (44), (45) and the transformation

$$P(\psi_s) = -P(Q)\, \frac{dQ}{d\psi_s} \quad , \qquad \text{(V-46)}$$

where the minus sign arises because increasing Q causes $\psi_s$ to decrease, thus

$$P(\psi_s) = (2\pi\sigma_s)^{-\frac{1}{2}} \exp\left[-(\psi_s - \bar{\psi}_s)^2/2\sigma_s^2\right] \quad \text{(V-47)}$$

,

where the standard deviation $\sigma_s$ of the surface potential is

$$\sigma_s = \left(\frac{e\bar{Q}}{\alpha}\right)^{\frac{1}{2}} \left(\frac{W(\bar{\psi}_s)}{C_0 W(\bar{\psi}_s) + \epsilon}\right) \quad \text{(V-48)}$$

.

If we assume that both the interface state density and capture cross section are nearly constant over an energy range of several kT, as previously discussed in the section on the continuum model, Eq. (31) can be modified to the form

$$\frac{G_p^j}{\omega} = (2\pi\sigma_s^2)^{-\frac{1}{2}} \frac{eN_{SSF}^j}{2} \int_{E_v^s}^{E_c^s} \frac{\ln\left(1+\omega^2\tau_{jF}^2 e^{-2\beta(\psi_s-\bar{\psi}_s)}\right)}{\omega\tau_{jF} e^{-\beta(\psi_s-\bar{\psi}_s)}} \exp\left[-\frac{(\psi_s-\bar{\psi}_s)^2}{2\sigma_s^2}\right] d\psi_s \quad \text{(V-49)}$$

.

A similar argument yields an equation for the imaginary part of impedance

$$C_p^j = C_D(\bar{\psi}_s) + (2\pi\sigma_s^2)^{-\frac{1}{2}} eN_{SSF}^j \int_{E_v^s}^{E_c^s} \tan^{-1}\left(\omega\tau_{jF} e^{\beta(\psi_s-\bar{\psi}_s)}\right) \exp\left[\frac{(\psi_s-\bar{\psi}_s)^2}{2\sigma_s^2}\right] d\psi_s \quad \text{(V-50)}$$

.

Now we can fit the experimental $G_p/\omega$ data with the expression in Eq. (V-49) to determine $N_{SSF}^j$, $\tau_{jF}$ and $\sigma_s$. Next we insert the fitted values of these three parameters into Eq. (V-50), and fit the experimental $C_p^j$ data to Eq. (V-50) to find $C_D(\bar{\psi}_s)$. Finally, the average surface

potential $\tilde{\psi}_s$ can be determined by the relation between the space-charge capacitance and the surface potential in Eq. (IV-36).

## C. Apparatus

The sensitivity of the conductance method is higher than that of the capacitance method. In order to take full advantage of this, we must exercise control of the experimental parameters. The signal is obtained by maximizing $C_0$, minimizing $C_d$ (or the carrier concentration), and using illumination.

The block diagram of the experimental arrangement is shown in Figure (V-3). The GR1615A capacitance bridge operates over the frequency range from 20 Hz to 100 KHz. The measured frequencies were checked against an HP3300 Function Generator and with an oscilloscope. The scope was also used to monitor the amplitude of the ac voltage applied to the sample through the bridge. The amplitude was chosen by two considerations: it has to be big enough to provide enough sensitivity for the measurement, but small enough so that the results were independent of the amplitude. We found experimentally that at room temperature for most frequencies the actual voltage across the MOS structure near the balance condition was 10 mV when the peak-to-peak amplitude at the HP3300 Function Generator was 500 mV. Since the actual ac voltage across the sample is only 10 mV and this is smaller than kT/e at room temperature, the small signal criterion is satisfied at room temperature. At liquid nitrogen temperature we found that a 350 mV peak-to-peak voltage from the Function

Generator resulted in $\sim$ 5 mV across the sample, and in this circumstance the measurement was again independent of the ac signal amplitude. A digital multimeter was used to measure the bias voltage and was disconnected from the measuring circuit before the bridge was balanced. Three terminal capacitance measurements were made throughout the experiment.

The bridge has two modes: it can either measure $C_{pT}$ and $G_{pT}$, or measure $C_{sT}$ and D. $C_{pT}$ and $G_{pT}$ are the total parallel capacitance and conductance respectively, while $C_{sT}$ is the total equivalent series capacitance and D is the dissipation factor. When $G_{pT}$ is small, the first mode is preferred because the sensitivity is better. However, when $G_{pT}$ becomes so large that it is out of the range of the first mode, the second mode is used to continue the measurement. In the intermediate range, both modes give consistent results.

The reliability of the data is quite good. The accuracy is poorest at the low and high frequency ends of the spectrum. However, even there the reproducibility is within 1%.

The samples were stored in a dry box at room temperature when they were not being studied. Some changed interface properties slightly after they were first prepared, but after about a month they stabilized. While data was being taken the samples were at times housed in an evacuated chamber, and at other times were exposed to the ambient atmosphere. No systematic differences were observed between data collected in these two arrangements.

D. Experimental results

For the oxide thicknesses normally used little accurate information can be extracted from measuring the imaginary part of the impedance. Since our samples have $C_0 \gg C_d/a$ for most bias voltages, accurate $C_p$ values can be obtained and we shall examine the frequency variation of both $G_p/\omega$ and $C_p$.

1. Results of the discrete model

Figure (V-4) presents a three-dimensional plot of $G_p/\omega$ versus frequency and interface-state energy relative to the valence-band edge E, taken in the light with no filter. Figure (V-5) is a similar plot in the dark. The variation of $C_p$ with f and E is shown in Figure (V-6) in the light, and in Figure (V-7) in the dark. The curves in all cases are fits to the data using the equivalent circuit in Figure (V-8). It consists of a parallel network of five capacitor-resistor pairs and the depletion or accumulation layer capacitance $C_{d/a}$, all in series with the insulator capacitance $C_0$. The parameters obtained from the fits to the data are listed in Table (V-1). These parameters will be interpreted in detail presently. For now it suffices to say that the indices I, V, C, f1, f2 stand for inversion, valence-band tail, conduction-band tail, fluorine-line 1, and fluorine-line 2, respectively. The resistance $R_j$ in series with each capacitance actually arises from the finite response time of that feature, and is related to $\tau_j$ by $R_j = \tau_j/C_j$.

The high-frequency features of $G_p/\omega$ and $C_p$ are almost unaffected by the light, but the low-frequency behavior is changed dramatically.

The high-frequency peak that grows for E in the upper part of the gap is identified as $C_c$, $\tau_c$ (solid diamonds). These states are the usual "fast interface-states" observed in n-type materials. The low-frequency peaks, which are fully formed only in the light, are identified as $C_v$, $\tau_v$ (open diamonds) and $C_I$, $\tau_I$. These states are the "slow interface-states" that cannot be observed in the absence of light because their time constants are too long.

In analyzing the data it is supposed that the interface states near the valence-band side exchange charge with the inversion layer rapidly compared to the response of either to an external stimulus. Hence, in the light, $\tau_v$ is set equal to $\tau_I$ and the low-frequency peak height of $G_p/\omega$ is equated to $(C_I + C_v)/2$. $C_I$ is calculated from the measured $\psi_s$, and subtracted to arrive at the $C_v$ values in Table (V-1). Since $C_I$ is always less than 10% of $C_v$ for all bias voltages, this assumption has little effect on the numbers in Table (V-1). The $\tau_v$ time constants in the dark are obtained by assuming that $C_v$ is light-insensitive, and fitting the slight curvature in the low-frequency $G_p/\omega$ and $C_p$ data at each bias to a $\tau_v$. We do not expect these numbers to be very reliable but note that they are quite long, well over one second. The $C_{f2}$, $\tau_{f2}$ numbers arise from the extra features that can be seen near the center of the gap. We have not observed any sign of $C_{f1}$, $\tau_{f1}$ in the impedance measurements, but this curve is so narrow that we may have missed it.

There is supposed to be a third fluorine peak in the upper part of the band gap. We have seen evidence that it is there but have

not attempted to track it in detail. It appears as a small shoulder on the low-frequency side of the high-frequency peak in $G_p/\omega$ .

The numbers in Table (V-1) were obtained by fitting the experimental $G_p/\omega$ and $C_p$ data to the discrete model Eqs. (V-24) and (V-25). Data points are included in Figures (V-4, 5, 6, and 7) only for the foremost curves. Other curves with data points can be found in reference [36]. The quality of the fits is equally good for all biases. The procedure works because sample Si-58, unlike many studied by others,[3] exhibits no statistical broadening. Also, the corrections to the shape functions introduced by the continuum model are such that they can be applied when the raw data is interpreted. This will be done in the next section.

2. Modified continuum model

Once the data has been fit to an equivalent circuit, interface-state densities must be extracted from it. The literal interpretation of the equivalent circuit and the relations in Eqs. (V-24) and (V-25) result from an SRH analysis for discrete interface states.[7] In this case, $C_v$ and $C_c$ are identified with interface state densities through the relations

$$C_j = e N_{ss}^j \quad , \qquad j = c\ ,\ v \quad , \tag{V-51}$$

and since the peak value of $(G_p^j/\omega)_{peak}$ is $C_j/2$

$$\left(\frac{G_p^j}{\omega}\right)_{peak} = \frac{e N_{ss}^j}{2} \quad . \tag{V-52}$$

Next we shall examine a modified version of the continuum model and extract the corresponding relation between $(G_p^J/\omega)_{peak}$ and $N_{SS}^J$.

From the observed variation of $C_c$ and $C_v$ with E, it is evident that the interface state profile does not resemble a collection of discrete states. They are better described as a continuum of states. The details of the shapes of the $C_c(\omega)$ and $G_p^c(\omega)/\omega$ curves support this contention. However, some modifications to the simple continuum model are required to fit the data.

The expressions, Eqs. (V-33) and (V-34), have been integrated numerically to illustrate the nature of the deviations from the continuum-model approximation in a modified continuum model (MCM). $N_{SS}^J(\xi)$ was replaced by a function that was fit to the general trends of the $C_v$ versus energy data for sample Si-58 at room temperature,

$$\frac{N_{SS}^c}{N_{SSF}^c} \cong \frac{\left(1 - \frac{E + E_{FS}}{1.00\,(eV)}\right)^{-3.02}}{\left(1 - \frac{E_{FS}}{1.00\,(eV)}\right)^{-3.02}} = \left[\frac{1 - \frac{E_{FS}}{1.00} - \frac{\ln\left(\frac{1-f_0}{f_0}\right)}{1.00\,\beta}}{1 - \frac{E_{FS}}{1.00}}\right]^{-3.02} \qquad \text{(V-53)}$$

The functional form for $\tau_c(\xi)$ is chosen to fit the observed shape of the frequency variation of $G_p/\omega$,

$$\frac{\tau_c}{\tau_{cF}} \cong \frac{\left(1 - \frac{E + E_{FS}}{1.00\,(eV)}\right)^{-4}}{\left(1 - \frac{E_{FS}}{1.00\,(eV)}\right)^{-4}} = \left[\frac{1 - \frac{E_{FS}}{1.00} - \frac{\ln\left(\frac{1-f_0}{f_0}\right)}{1.00\,\beta}}{1 - \frac{E_{FS}}{1.00}}\right]^{-4} \qquad \text{(V-54)}$$

The results of the numerical integrations of Eqs. (33), (34), (53), (54) for $E_{FS}$ = 0.318 eV (corresponding to V = 0.0 V), with the corresponding discrete-level (Eqs. (24), (25)), and continuum-model (Eqs. (30), (31)) curves, are shown in Figure (V-9).

The different models all produce $G_p^j/\omega$ versus frequency curves for fixed $\psi_s$ that peak for different $\omega\tau$ products, $\omega_{peak}\tau = \Omega$, $\Omega$ = 1.00, 1.98, 2.35 respectively for the DM, CM, and MCM. The curves in Figure (V-9) are adjusted so they peak in the same place by plotting $C_p^c/eN_{SSF}^c$ against $f = 2 \times 10^3\ \omega\tau_{cF}/\Omega$. The $2 \times 10^3$ factor in f is the frequency of the observed peak in $G_p^c/\omega$ at V = 0.

Several conclusions become evident immediately on inspection of the curves in Figure (V-9). The experimental $G_p^c/\omega$ and $C_p^c$ points lie between the DM and CM curves, but they are closer to the CM curves. Since the experimental $G_p/\omega$ points lie within the CM curve, no statistical broadening is in evidence; a result consistent with the absence of a positive fixed charge. Notice that the ratio $C_p^c(0)/(G_p^c/\omega)_{peak}$ is $\sim$ 2.4, 2.00, 2.48, and 2.38 for the experimental data, DM, CM, and MCM curves respectively; slightly favoring the MCM over the CM interpretation and mitigating against the DM interpretation. If the capture cross section is assumed to be constant independent of energy, then the change in $G_p^c/\omega$ caused by the energy variation of $N_{SS}^c$ alone (Eqs. (34), (53)) is to broaden the line relative to the CM. A variation of the capture cross section in which it becomes larger near the band edge causes $G_p^c/\omega$ to narrow, while the opposite trend causes $G_p^c/\omega$ to broaden. The minus fourth power energy dependence on Eq. (54) was selected to fit the data. The shape

of the $G_p^c/\omega$ curves alone offer little discrimination between the CM and MCM interpretations. However, the shape of the high frequency roll off of $G_p^c/\omega$, and the ratio $C_p^c(0)/(G_p^c/\omega)_{peak}$ are more sensitive to the model choice.

The relation between the peak value of $G_p/\omega$ and the interface state density is model dependent, $(G_p^j/\omega)_{peak} = g_j e N_{SS}^j$, where $g_c = 2.00$, 2.48, and 2.31 for the DM, CM and MCM respectively. The conductance-determined interface-state densities listed in Table 3 were derived from the $C_p^j$, $j = c, v, f2$ values in Table 2 by using the relations $N_{SS}^j = 1.24\ C_p^j/e = 2.48\ (G_p^j/\omega)_{peak}/e$, $j = c,v$ and $N_{SS}^{f2} = C_p^{f2}/e = 2(G_p/\omega)_{peak}$ The $N_{SS}^j$ values determined from the quasistatic measurement are all determined from the relation $N_{SS}^j$ and $C_{QS}^j/e$. These interface-state densities, along with one for $N_{SS}^{f1}$ found from the quasistatic measurements, are listed in Table V-3 and plotted together in Figure (V-10). The properties of these curves will be explored in Section VII.

### 3. A sample with statistical broadening

Most of our samples have little or no flat band voltage shift due to positive fixed charges and show no sign of statistical broadening. However, broadened $G_p(\omega)/\omega$ peaks are observed in the depletion region on Sample Si-107. Si-107 has a 250Å $SiO_2$ layer, a moderately large flat band voltage $V_{FB} = 1.20V$, and a $\langle 110 \rangle$ orientation. These features are consistent with the existence of statistical broadening from fluctuations in the location of the positive fixed charge. Without including statistical broadening the $G_p(\omega)/\omega$ curves cannot be fit well. Numerical

integration of Eq. (V-49) was done to fit the experimental data points. There are three parameters to be determined in Eq. (V-49): the time constant $\tau^j$, the interface state density $N_{SS}^j$, and the standard deviation $\sigma_s$.

In order to examine the effect on the curve of changing the parameters, only one branch of interface states was considered. Taking the data at 0.25V bias as a trial, we found the time constant $\tau^j = 5.2 \times 10^{-3}$ sec corresponding to the $G_p(\omega)/\omega$ peak. This value of $\tau^j$ confirms the peak occuring at $\omega\tau^j = 2.50$ as claimed in Ref. [7]. However, the other two parameters can be changed continuously and still fit the data points equally well. The values of the parameters are listed in Table (V-2). It is evident that when statistical broadening is present, the data reduction is much less reliable.

There is another difficulty with the statistical broadening model. In this model, the mean number of surface charges $\bar{N}$ can be calculated from the measured flat band voltage $V_{FB}$ by

$$\bar{N} = V_{FB}\, C_{OT}/2 \quad ,$$

where $C_{OT}$ is the total insulator capacitance of the sample. Assuming the Gaussian approximation to a Poisson probability distribution of Eq. (V-36), the standard deviation can be written as $\sigma_s = e\bar{N}^{1/2}/C_{OT}$. Combining these equations yields $\sigma_s = (eV_{FB}/C_{OT})^{1/2}$. Substituting the parameters for Si-107, $V_{FB} = 1.20$V and $C_{OT} = 4.13$ nF, we get $\sigma_s = 6.8 \times 10^{-6}$V. This is much smaller than the values needed to fit the data. According to others,[2,3,7,36] $\sigma_s$ is found to be of the

order of kT/e. However, none of these papers also quote a flat band voltage, but values calculated from this model are unbelievable. For example, in reference [32], the sample has diameter D = 0.55 mm, and insulator capacitance per unit area = 3.26 nf/cm$^2$. Assuming $\sigma_s$ = kT/e as indicated in their Table 1, we find $V_{FB}$ = 3.0 x 10$^5$V, which is impossibly big. This argument also applies to the more detailed Eq. (V-48) with $\alpha$ taken as the area of the device and $C_0$ large. The difficulty evidently arises from the assumptions leading to the Poisson distribution. The Poisson distribution is correct if the possibility for a charged center to be located in a given position is independent of the location of the other charges. Since this assumption predicts results grossly different from the experiments, it is violated and the locations of the charges are correlated. A detailed study of these correlations would constitute an interesting extension to the present work.

### 4. Time constant

Finally, let us examine the light intensity and energy variation of the time constants $\tau_v$, $\tau_c$. The $\tau_v^{-1}$ values found directly from the fits to the discrete-level curves should be multiplied by $\Omega_v$ to determine absolute numbers. While $\tau_v$ is uncertain to within a multiplicative constant, information can nevertheless be extracted from its bias voltage and light intensity variation. The SRH theory that relates the measured impedance to the interface state density and response time, Eq. (V-26) is easily generalized to include the effects of low intensity

light. The only modification is that the time constant $\tau_v$ becomes

$$\tau_v = \tau_v^{dark} e^{-e\delta\psi_s/kT} \qquad \text{(V-55)}$$

where $\delta\psi_s$ is the shift of the surface potential caused by the light flux $\Phi$ ,

$$\delta\psi_s = \left(\frac{eA}{C_d}\right) \tau_r \Phi \quad , \qquad \text{(V-56)}$$

assuming the quantum efficiency is unity, and $\tau_r$ is the electron-hole recombination time across the space charge layer. The data is summarized in Table (V-4). Table (V-5) contains parameters that result from fitting the data to Eqs. (55), (56). Notice that $e^2 A \tau_r / C_d kT$ is nearly constant, and if these numbers are multiplied by the measured capacitances $C_d$ they are even more nearly constant, $e^2 A \tau_r / kT = 6.32 \pm 0.49$ (F-sec), which implies $\tau_r \cong 9.1$ ms. Since $\tau_v^{dark}$ should vary proportionally to $e^{+e\psi_s/kT}$ we have tested this relation by fitting $\tau_v^{dark} = K_1 e^{K_2 \psi_s}$. The $\psi_s$ values used (see Table V-4) are those taken from the quasi-static measurement in the no filter case. This is done because the error in $\psi_s$ introduced by the fact that the quasistatic condition is not satisfied ($|\psi_s^{light} - \psi_s^{dark}|_{max} = 250$ mV), is larger than the shift $\delta\psi_s$ caused by the light ($\delta\psi_{smax} = 68$ mV). Using this procedure one finds $K_1 = 9.65 \times 10^{-11}$ sec, and $K_2 = 40.7$ ($eV^{-1}$) with a coefficient of determination $\chi^2 = 0.93$. The $K_2 = 40.7$ ($eV^{-1}$) is close to e/kT for room temperature and tends to confirm the model.

Figure (V-11) is a plot of $\tau_c' = 2.35 \tau_c$ as a function of energy E. The reason for the $\Omega_c = 2.35$ factor has been discussed.

For comparison, the $\tau$ from the SRH model deduced from parameters measured by Nicollian and Goetzberger[7] is shown. Obviously the response times of our conduction-band tail states have a different functional dependence and are faster than the SRH model predicts. We shall address this quandry in Section VII. The insensitivity of $\tau_c$ to light can be understood by examining Eq. (V-56). For the more positive surface potentials where $\tau_c$ is measured $C_d$ is larger, and $\tau_r$ is expected to be smaller since the electrons and holes have a smaller barrier to overcome in order to recombine. Evidently for the range of surface potentials where most $\tau_c$ values are measured, $\delta\psi_s \ll kT$, and $\tau_c \cong \tau_c^{dark}$.

Table V-1

| $Y$ | $E$ | $C_c$ | $\tau_c$ | $C_v + C_I$ | $\tau_v$ | $C_{f2}$ | $\tau_{f2}$ | $C_d$ | $C_D$ | $C_F$ | $C_{QS}$ |
|---|---|---|---|---|---|---|---|---|---|---|---|
| -0.50 | 0.246<br>0.037 | $1.5 \times 10^{-10}$<br>1.5 | $5.9 \times 10^{-5}$<br>5.9 | $4.9 \times 10^{-8}$<br>1.01 | 0.066<br>1.634 | | | $2.43 \times 10^{-10}$<br>1.99 | $2.9 \times 10^{-9}$<br>$1.14 \times 10^{-7}$ | $6.07 \times 10^{-8}$ | $1.40 \times 10^{-7}$ |
| -0.25 | 0.263<br>0.088 | 1.81<br>1.88 | 7.1<br>7.1 | 1.55<br>1.01 | 0.022<br>0.42 | | | 2.43<br>2.13 | $1.77 \times 10^{-9}$<br>$9.21 \times 10^{-8}$ | 1.94 | $3.94 \times 10^{-8}$ |
| -0.10 | 0.297<br>0.154 | 2.08<br>2.08 | 6.2<br>6.2 | $8.6 \times 10^{-9}$<br>4.1 | 0.033<br>0.245 | | | 2.66<br>2.41 | $7.32 \times 10^{-10}$<br>$2.50 \times 10^{-8}$ | 1.13 | 2.34 |
| 0.0 | 0.310<br>0.233 | 2.25<br>2.25 | 6.75<br>6.75 | 6.07<br>$4.65 \times 10^{-10}$ | 0.0068<br>0.0188 | | | 2.61<br>2.51 | $5.59 \times 10^{-10}$<br>$4.10 \times 10^{-9}$ | $5.32 \times 10^{-9}$ | 1.36 |
| 0.06 | 0.337 | 2.9 | 8.5 | | | | | 2.80 | $3.86 \times 10^{-10}$ | | |
| 0.10 | 0.369<br>0.306 | 2.81<br>2.81 | 7.5<br>7.5 | $2.25 \times 10^{-9}$<br>$8.2 \times 10^{-10}$ | 0.0038<br>0.015 | | | 2.81<br>2.78 | 3.24<br>6.03 | 3.42 | $5.41 \times 10^{-9}$ |
| 0.16 | 0.397 | 2.8 | 6.0 | $2.05 \times 10^{-9}$ | 0.004 | $8.0 \times 10^{-11}$ | $5.0 \times 10^{-4}$ | 2.90 | 3.14 | 3.26 | 4.03 |
| 0.20 | 0.429 | 3.0 | 7.0 | 1.58 | 0.0026 | $2.3 \times 10^{-10}$ | 3.0 | 3.03 | 3.19 | 2.07 | 4.13 |
| 0.21 | 0.435 | 3.3 | 7.0 | | | 3.9 | 3.5 | 3.21 | 3.21 | | |
| 0.24 | 0.455 | 4.5 | 8.5 | $7.2 \times 10^{-10}$ | 0.0022 | 5.0 | 4.7 | 3.28 | 3.30 | 2.28 | 4.04 |
| 0.25 | 0.461<br>0.422 | 4.9<br>6.3 | 8.0<br>$1.0 \times 10^{-4}$ | 5.25<br>2.2 | 0.0021<br>0.0029 | 5.5<br>3.3 | 3.8<br>4.5 | 3.3<br>3.3 | 3.33<br>3.17 | 2.14 | 3.93 |
| 0.26 | 0.468 | 5.0 | $8.3 \times 10^{-5}$ | 4.8 | 0.0023 | 5.8 | 4.4 | 3.32 | 3.36 | 2.13 | 3.79 |
| 0.275 | 0.482 | 7.0 | 9.0 | | | 4.9 | 4.5 | 3.43 | 3.43 | | |
| 0.30 | 0.496<br>0.457 | 8.0<br>7.65 | $1.7 \times 10^{-4}$<br>1.1 | 2.1<br>1.6 | 0.0027<br>0.0027 | 4.0<br>3.2 | 4.2<br>4.2 | 3.55<br>3.55 | 3.31<br>3.31 | 2.01 | 2.94 |
| 0.355 | 0.532 | $1.08 \times 10^{-9}$ | 1.3 | 1.1 | 0.0010 | 2.6 | 4.0 | 3.90 | 3.67 | 2.13 | 1.81 |
| 0.50 | 0.632<br>0.610 | 2.04<br>1.99 | 1.8<br>1.68 | 3.05<br>1.65 | 0.0012<br>0.0012 | | | 4.61<br>4.63 | 4.85<br>4.53 | 2.84 | 3.18 |
| 0.75 | 0.790<br>0.737 | 7.4<br>7.1 | 5.3<br>4.8 | | | | | | $1.344 \times 10^{-9}$<br>$9.61 \times 10^{-10}$ | $2.263 \times 10^{-8}$ | 8.40 |
| 1.00 | | $(1.82 \times 10^{-8})$ | $(1.05 \times 10^{-3})$ | | | | | | | | |

Table V-2

| $N^{j}_{SSF}$ $\left[\frac{states}{eV\text{-}cm^2}\right]$ | $2.31 \times 10^{12}$ | $1.29 \times 10^{12}$ | $9.52 \times 10^{11}$ | $1.26 \times 10^{12}$ |
|---|---|---|---|---|
| $\sigma_s[v]$ | 1.00 | 0.50 | 0.10 | 0.025 |

Table V-3

| E | $N_{SS}^{QS}$ | $N_{SS}^{v_{cond}}$ | $N_{SS}^{c_{cond}}$ | $N_{SS}^{f2}$ |
|---|---|---|---|---|
| 0.237 | $7.85 \times 10^{13}$ | | | |
| 0.242 | 2.21 | | | |
| 0.244 | 1.75 | | | |
| 0.246 | 1.55 | $8.56 \times 10^{12}$ | $2.77 \times 10^{10}$ | |
| 0.248 | 1.47 | | | |
| 0.250 | $9.82 \times 10^{12}$ | | | |
| 0.263 | | 2.57 | 3.34 | |
| 0.273 | 5.20 | | | |
| 0.297 | | 1.47 | 3.85 | |
| 0.310 | | $6.55 \times 10^{11}$ | 4.16 | |
| 0.377 | | | 5.36 | |
| 0.369 | | 4.09 | 5.19 | |
| 0.397 | | 3.75 | 5.18 | $1.48 \times 10^{10}$ |
| 0.429 | | 2.99 | 5.50 | 4.25 |
| 0.435 | | | 6.10 | 7.21 |
| 0.455 | | 1.33 | 8.3 | 9.24 |
| 0.461 | | $9.75 \times 10^{10}$ | 9.06 | $1.02 \times 10^{11}$ |
| 0.468 | | 8.80 | 9.24 | 1.07 |
| 0.482 | | | $1.29 \times 10^{11}$ | 1.02 |
| 0.496 | | $3.96 \times 10^{10}$ | 1.49 | $7.39 \times 10^{10}$ |
| 0.532 | | 2.30 | 2.00 | 4.81 |
| 0.632 | | 3.05 | 3.81 | |
| 0.790 | | | $1.37 \times 10^{12}$ | |
| 0.848 | $3.29 \times 10^{12}$ | | 3.37 | |
| 0.860 | 3.96 | | | |
| 0.875 | 7.44 | | | |
| 0.880 | 8.93 | | | |
| 0.890 | $1.27 \times 10^{13}$ | | | |

Table V-4

| V \ fil / $\phi$ [$cm^{-2}$-$sec^{-1}$] | dark<br>0 | $10^{-2}$<br>$1.43 \times 10^{11}$ | $10^{-1}$<br>$8.60 \times 10^{11}$ | $10^{0}$<br>$8.76 \times 10^{12}$ |
|---|---|---|---|---|
| 0 | 24 | 24 | 16 | 4.0 |
| -0.10 | 250 | 230 | 87 | 13 |
| -0.25 | 420 | 270 | 130 | 22 |
| -0.50 | 1430 | 810 | 460 | 66 |

Table V-5

| V[V] | $\tau_v^{dark}$[ms] | $\frac{e^2 A}{C_d} \frac{\tau_r}{kT}$ [cm$^2$-sec] | $\chi^2$ | $\psi_s$[V] |
|---|---|---|---|---|
| 0 | 22.5 | $2.01 \times 10^{-13}$ | 0.98 | -0.479 |
| -0.1 | 168 | 2.96 | 0.93 | -0.510 |
| -0.25 | 270 | 2.92 | 0.91 | -0.544 |
| -0.50 | 907 | 3.04 | 0.93 | -0.561 |

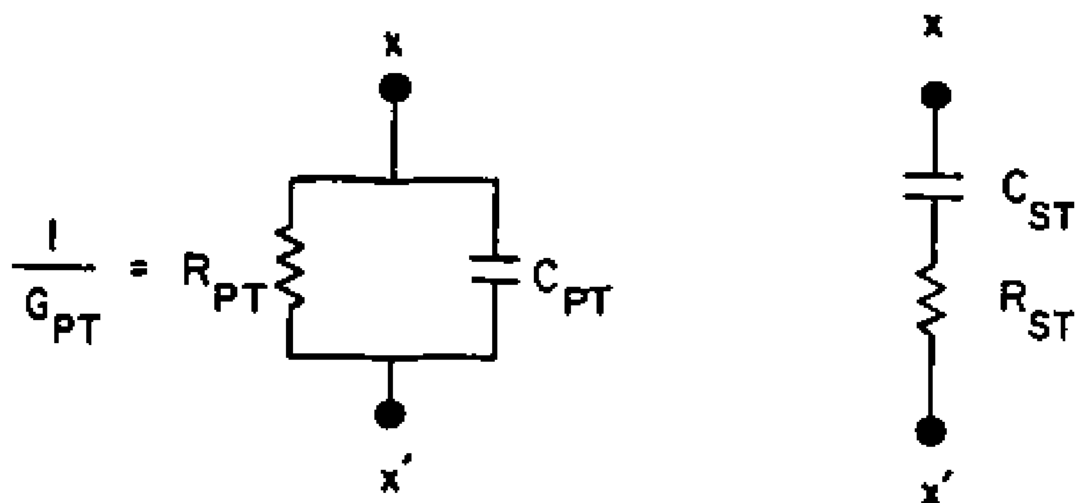


$$R_{PT} = R_{ST}\left(\frac{D^2 + 1}{D^2}\right)$$

$$C_{PT} = \left(\frac{C_{ST}}{D^2 + 1}\right)$$

where $D = \omega R_{ST} C_{ST}$

Fig. V-1

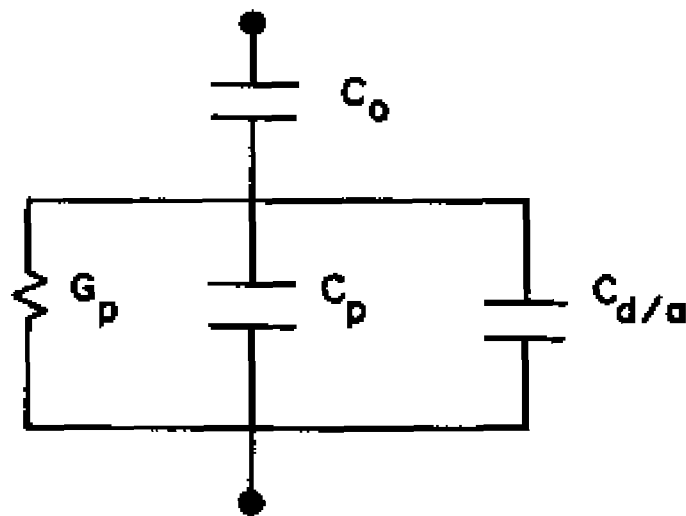


Fig. V-2

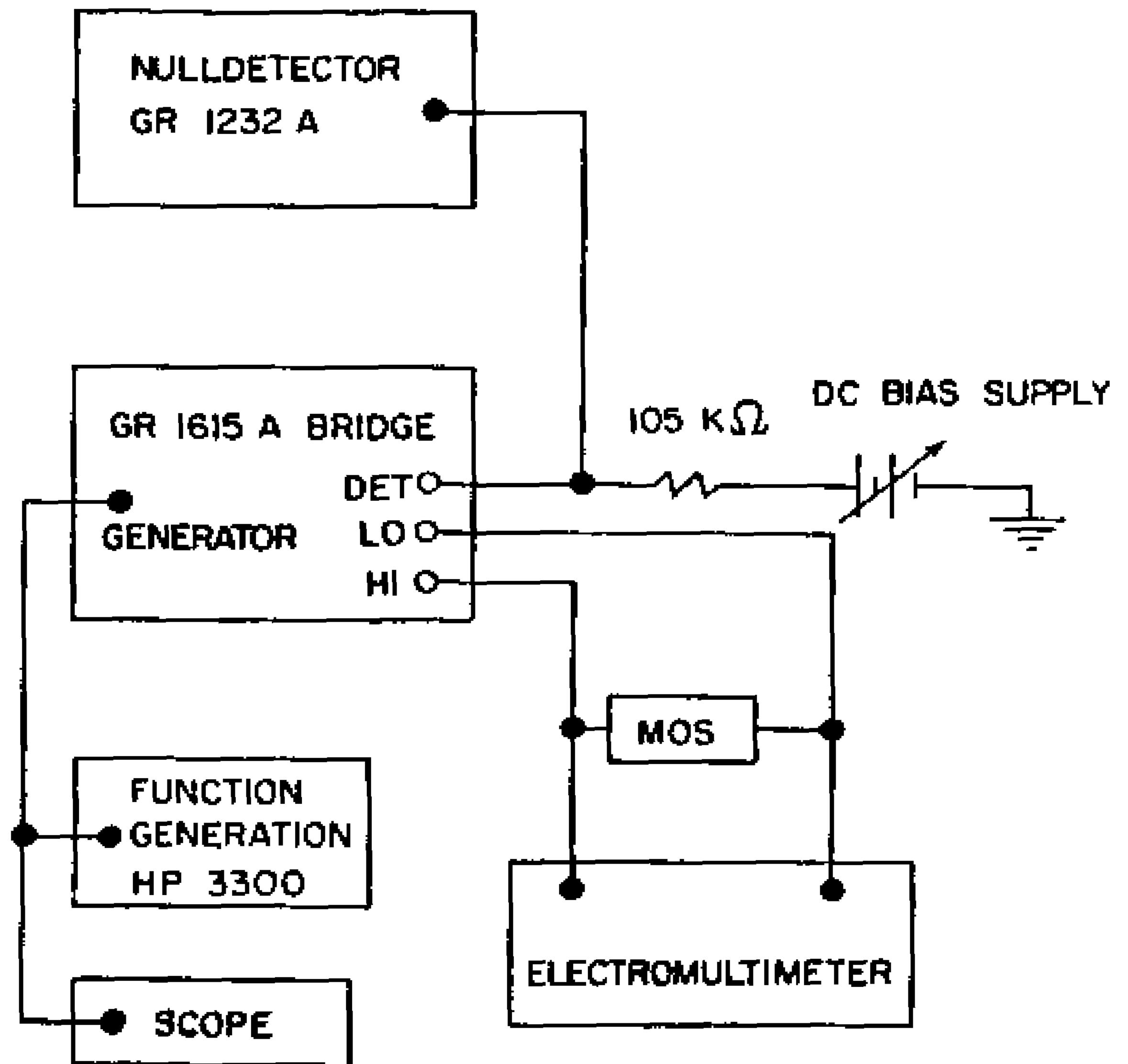


Fig. V-3

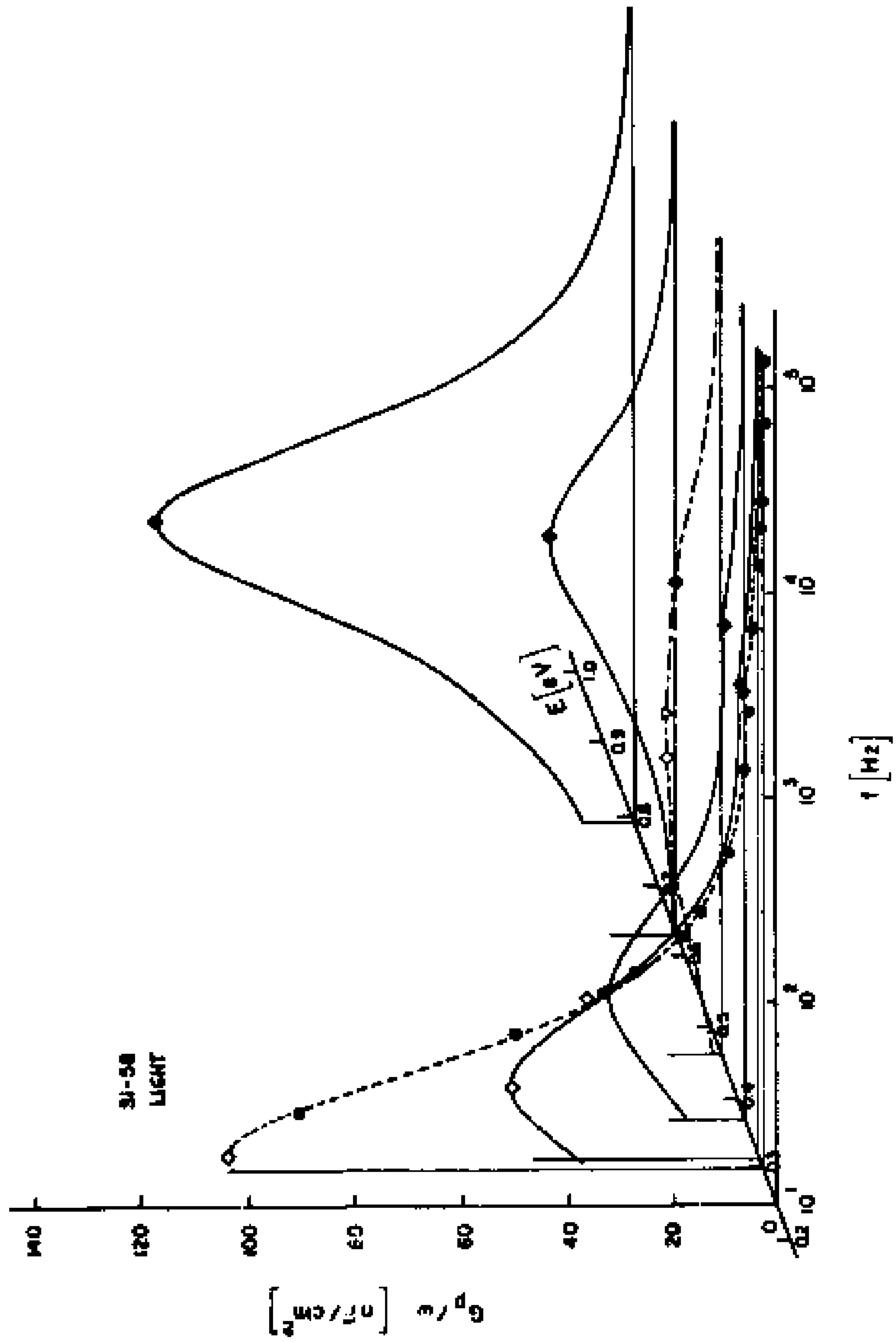


Fig. V-4

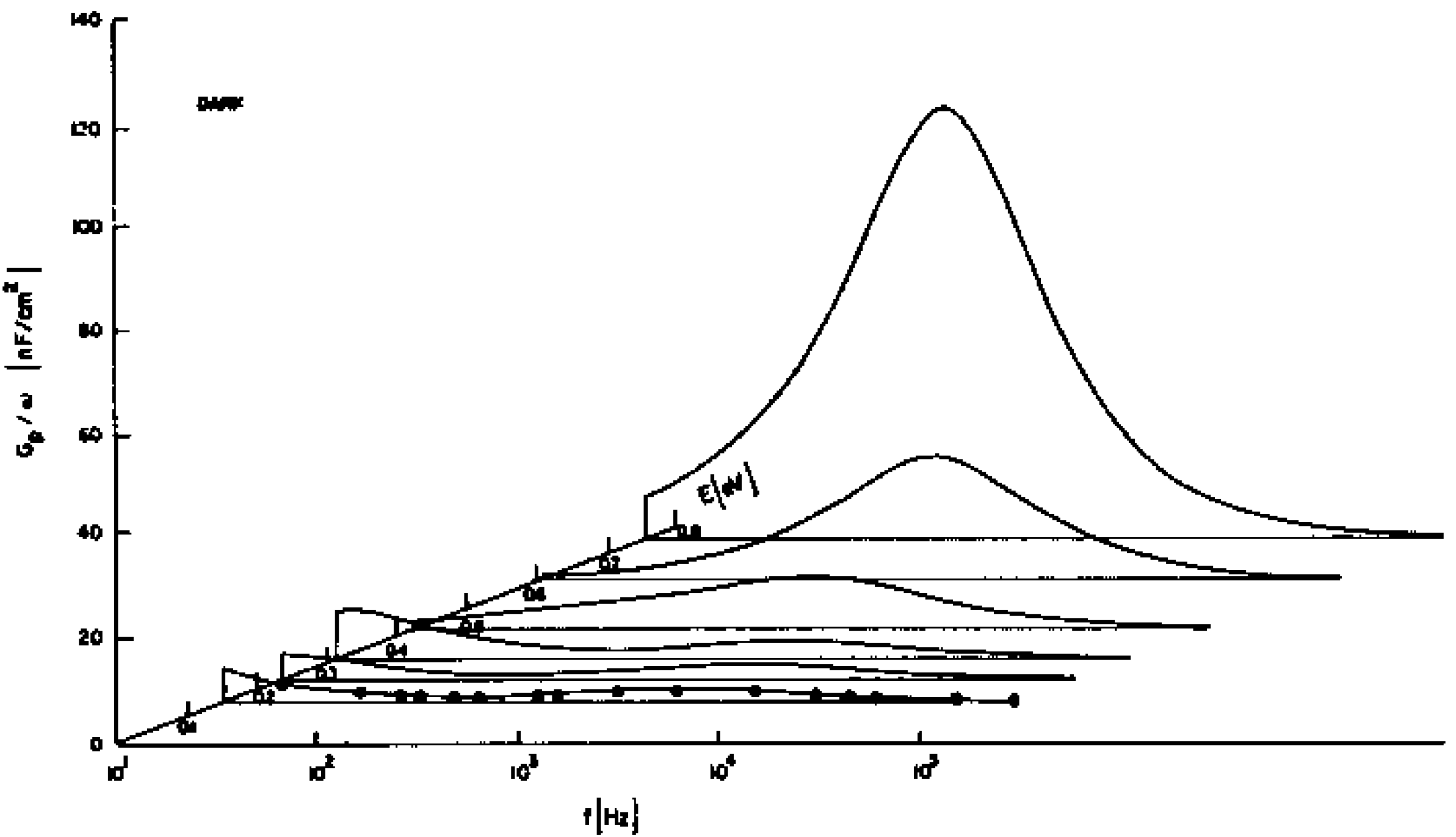


Fig. V-5

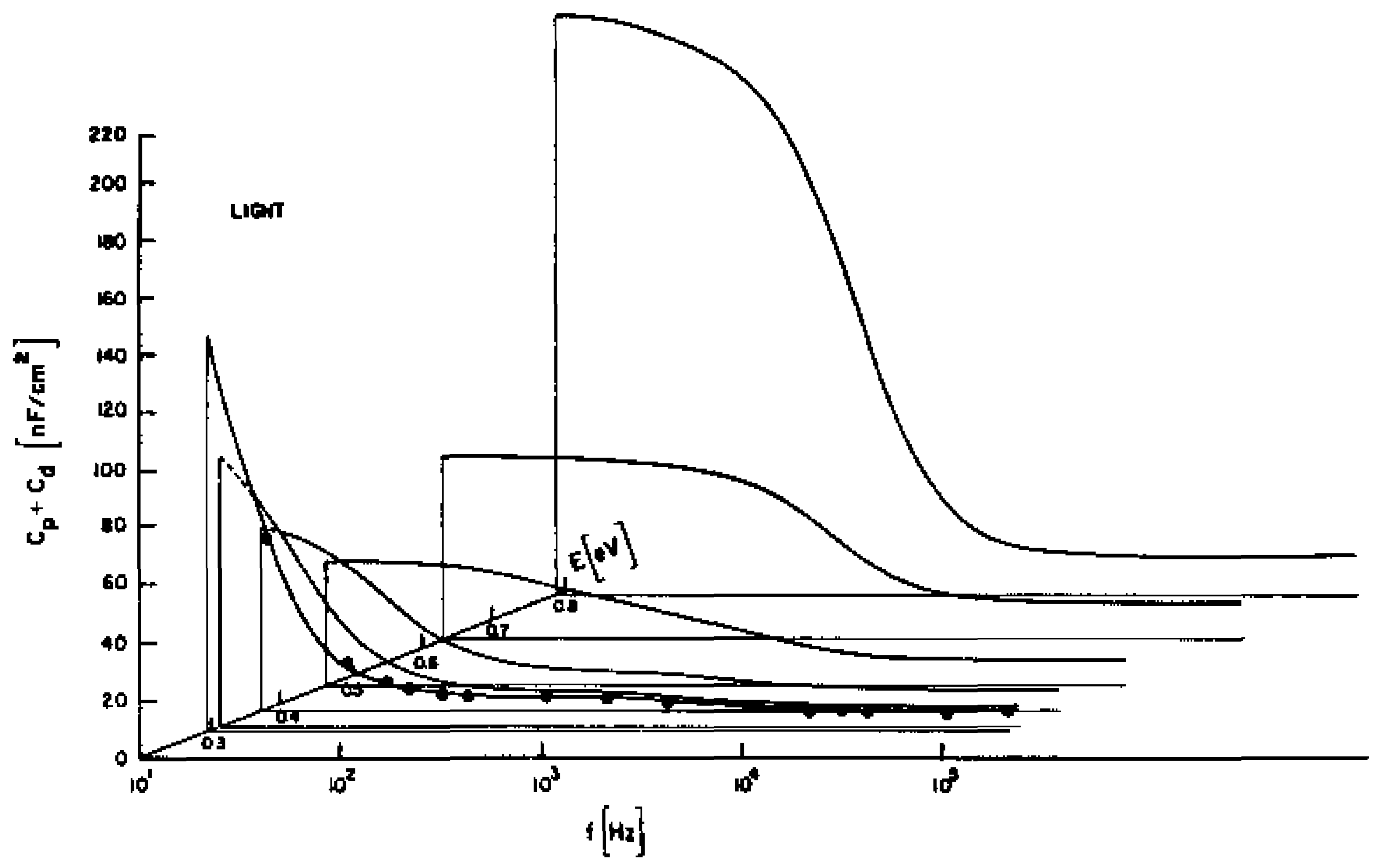


Fig. V-6

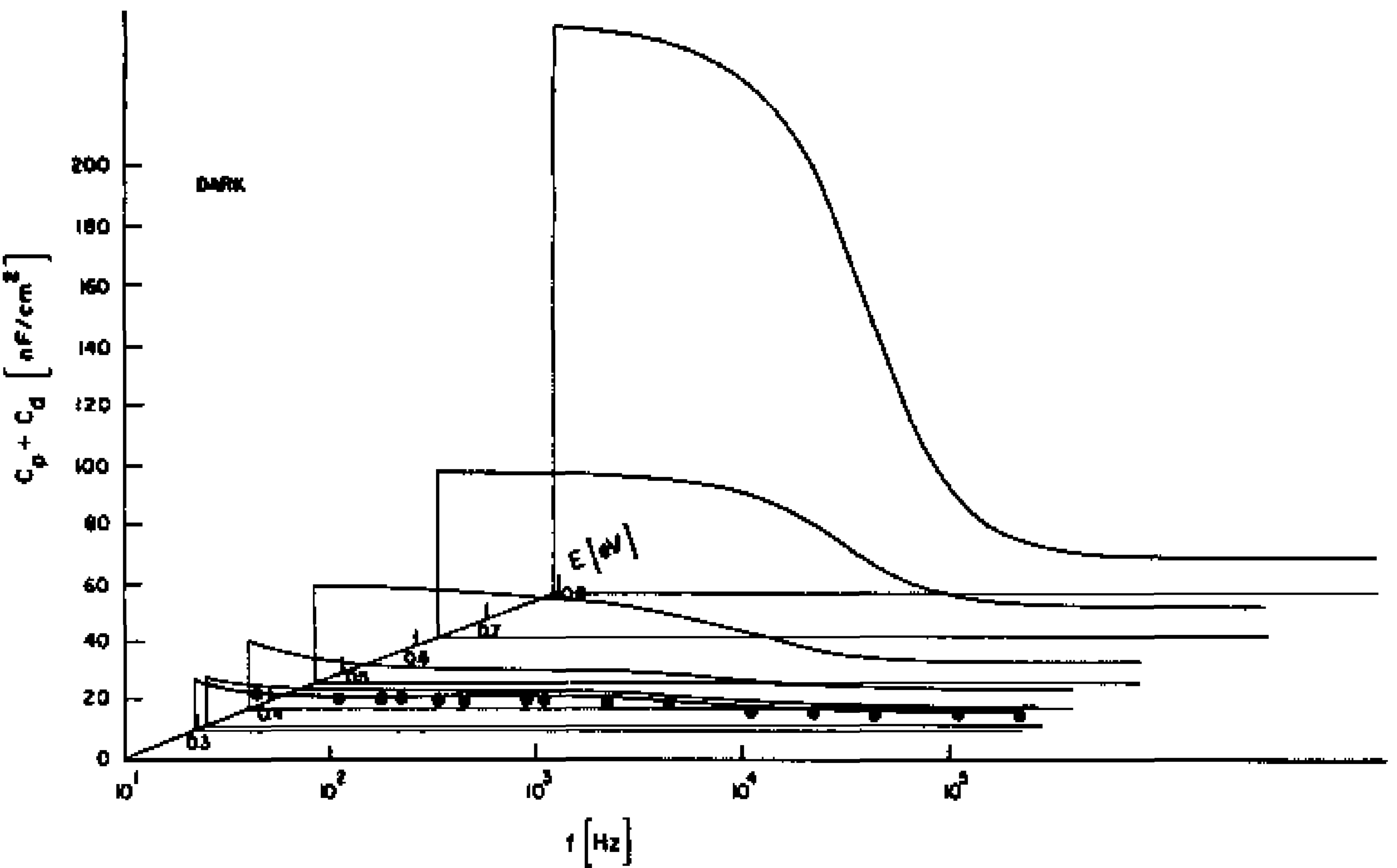


Fig. V-7

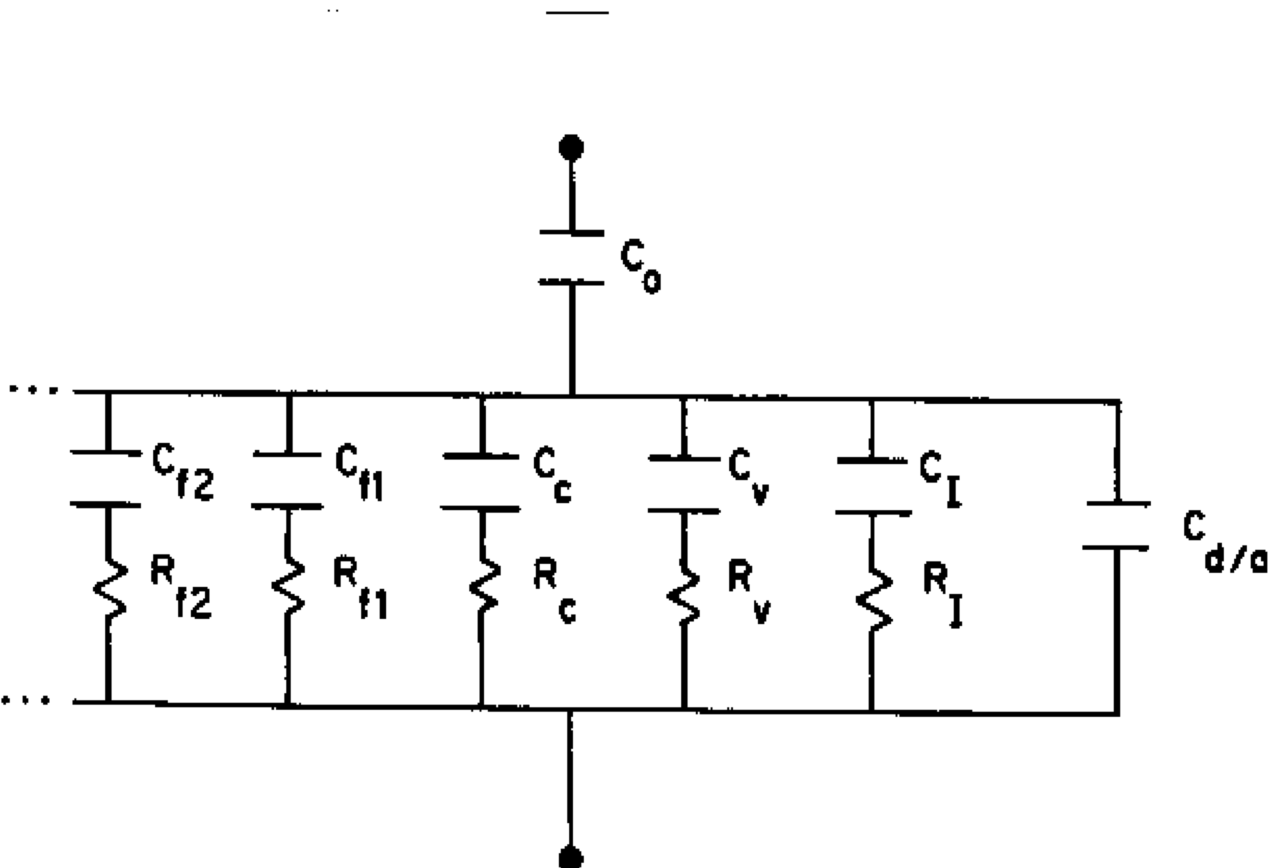


Fig. V-8

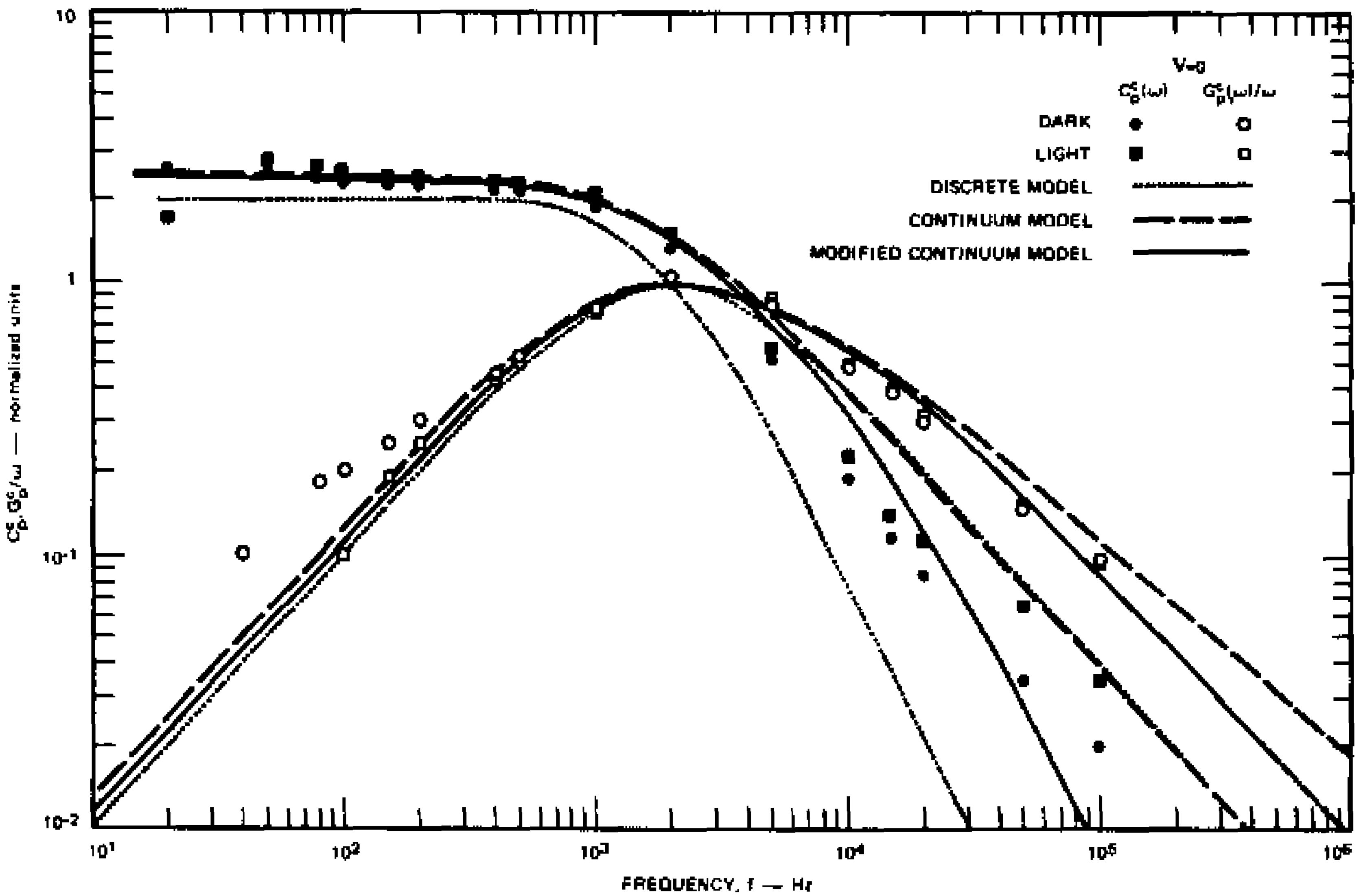


Fig. V-9

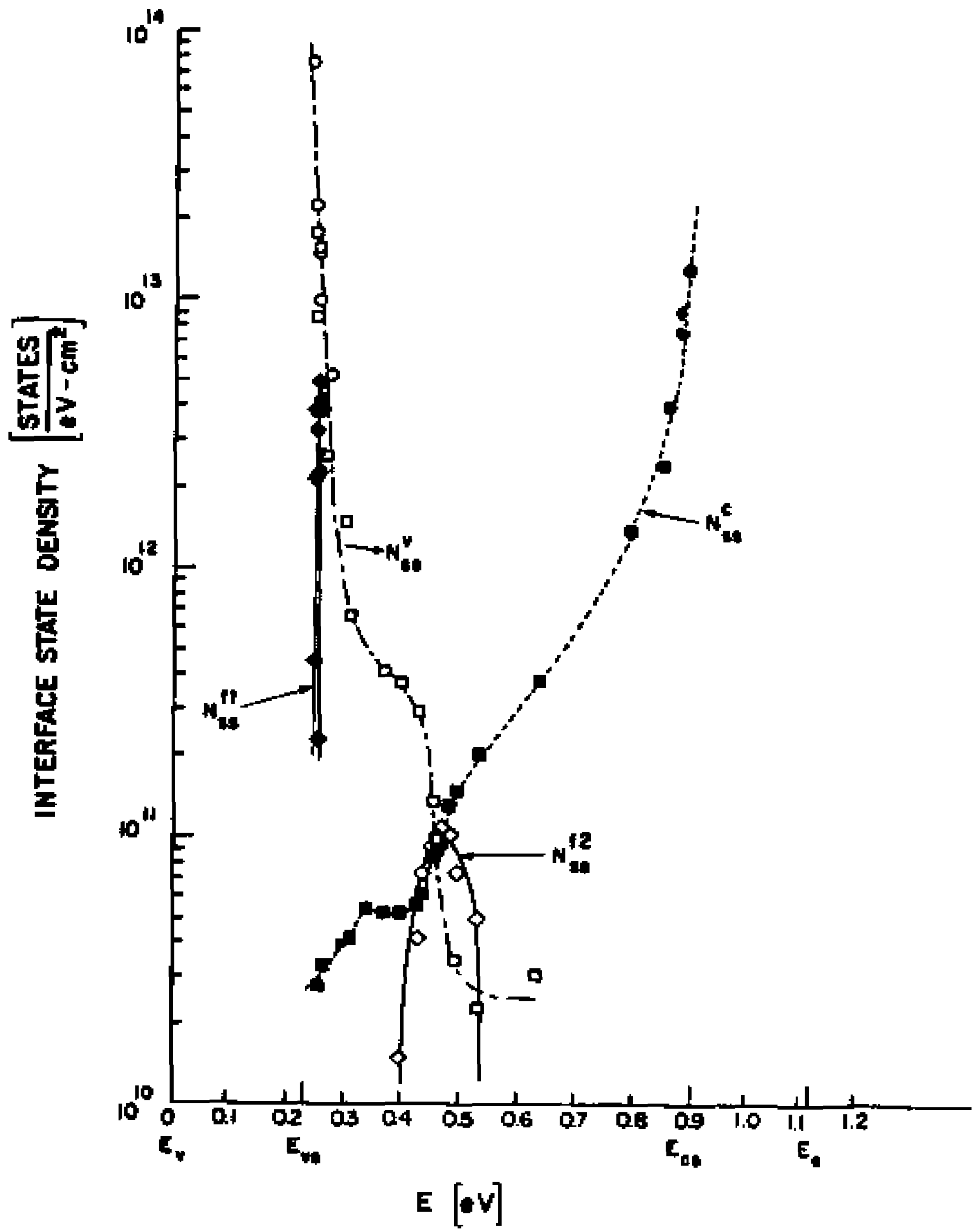


Fig. V-10

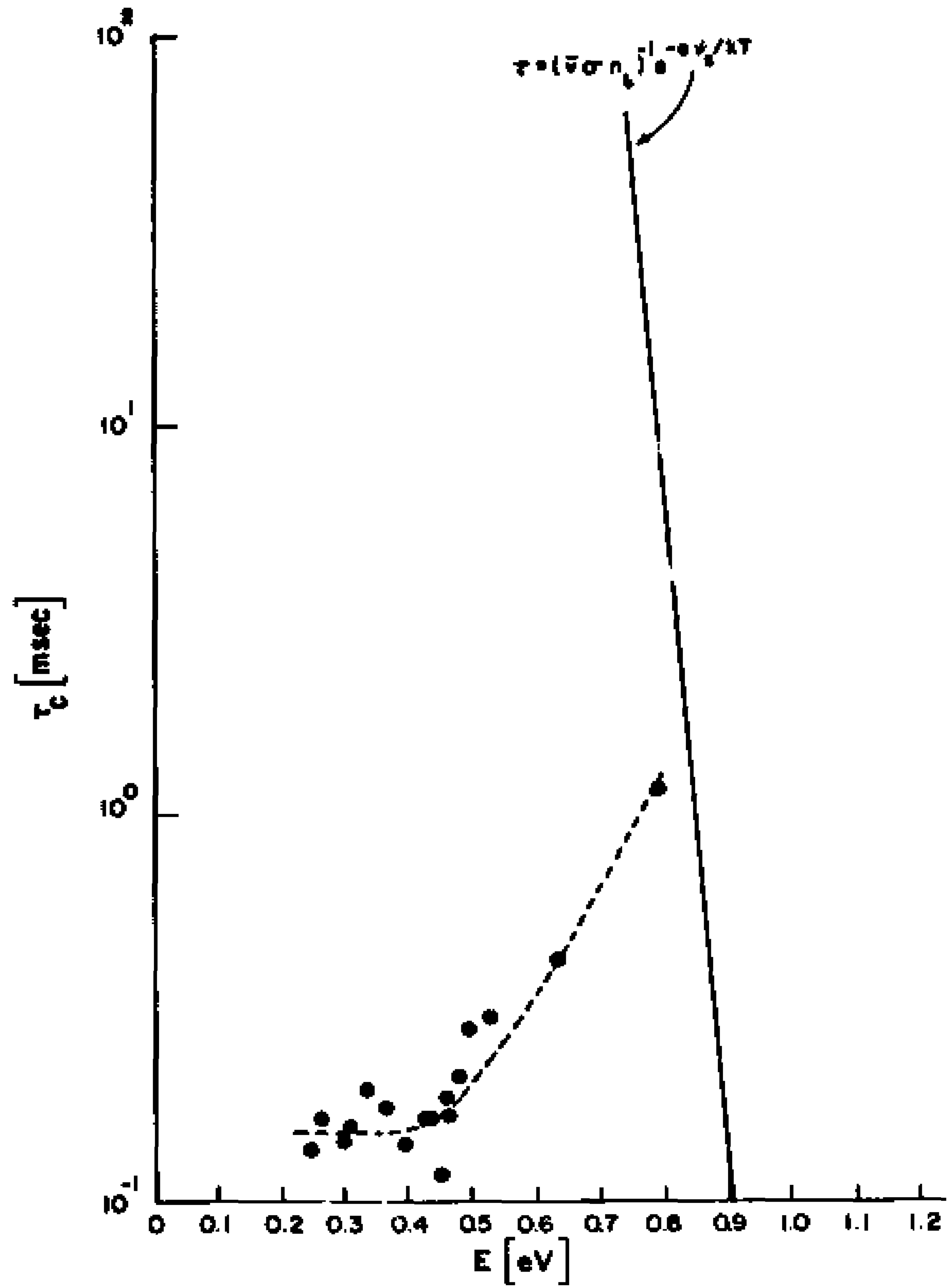


Fig. V-11

## VI. OTHER INTERESTING DATA

In addition to the data presented in the previous sections, measurements have been made on many other samples. The most interesting results are collected in this section. Results of some preliminary experiments on the sample Si-58 at liquid nitrogen temperature, samples with 500Å thick oxides, and one sample with a (110) surface orientation are presented. Table (VI-1) summarizes the general character of the samples investigated.

### A. Si-58 at liquid nitrogen temperature (77°K)

The measurements made on Si-58 at room temperature were all repeated at 77°K. From the variation of $Cd^{-2}$ with $\psi_s^*$, the maximum excursion of surface potential and the carrier concentration were determined to be 0.381 V and $1.90 \times 10^{14}$ $cm^{-3}$, respectively. Then we plotted surface potential versus applied bias voltage and found $V_{FB}$ = 0.91 V. Since the flat band voltage for this sample is mostly due to the work function difference between the metals on the front and back surfaces, it should behave as a thermocouple and decrease when the temperature is lowered. This is the observed trend. The decrease of the effective carrier concentration results from carrier freeze out. The donor energy that would produce this result is 51 MeV, a typical number for donors in silicon.

The 77°K quasistatic and conductance measurements were taken in light at the same wavelength 0.820 $\mu$m as the room temperature data, but with intensity about an order of magnitude higher at 16.5 $\mu W/cm^2$. There is little change in the gross character of the quasistatic capacitance curve as the light intensity changes from 1.60 $\mu W/cm^2$ to 16.5 $\mu W/cm^2$. The major qualitative change is that the fluorine lines are broadened by the higher light intensity and the depletion layer, as determined from $C_d$, is thinned slightly. The $G_p/\omega$ peaks for states in the valence band tail are shifted to higher frequencies and are easier to study under higher illumination levels. This is the principal reason the higher light intensity was used.

The data at 77°K were taken and reduced in the same fashion as described in Sections IV and V at room temperature. The shape of the conductance curves could still be fit accurately by the discrete level expressions, and then related to the continuum model interface state densities and time constants with the same multiplicative factors discussed before.

The resulting interface state densities and the conduction band tail time constants as functions of the energy in the band gap are illustrated in Figures (VI-1) and (VI-2). The density of states exhibits the same general structure found at room temperature, but shifted toward the valence band edge. A new spectral feature appears in the energy variation of $\tau_c$. Evidently at 77°K the response times of the system can be used to help sort the various contributions to the density of states.

B. Si-101

This sample has a 500Å thick oxide layer on a (100) surface, followed by 250Å of $LaF_3$. It was prepared so we could examine the effect of a thicker oxide layer on the interface states and the fluorine lines. We anticipated that growing a thick oxide might produce a less abrupt transition region from the Si to the $SiO_2$ which may broaden interface state features. The area under the fluorine lines were expected to decrease since less fluorine should diffuse to the interface.

The quasistatic capacitance measurement was conducted at a ramp rate of 10.3 mV/sec in the dark and at two light intensities. The curves are shown in Figure (VI-3). The middle curve was taken at light intensity $P_0 = 1.60\ \mu W/cm^2$ which is slightly lower than the highest light intensity used in Figure (IV-2). The highest light intensity was $16.5\ \mu W/cm^2$. All the curves are sharper than those for Si-58. In part this is due to the near absence of the strong fluorine lines, and in part it is caused by differences in the interface states. A very small shoulder appears on the curves at the energy of second fluorine line of Figure (IV-2). The first fluorine line is imperceptible. Apparently, thicker oxide, as expected, prevents most of the fluorine ions from diffusing through it to the interface.

Figure (VI-4) is a plot of the reciprocal of the square of the high frequency depletion layer capacitance $C_d^{-2}$ versus the quantity $\Psi_s^*$ defined in Eq. (IV-9). Once again we find that the slopes of the straight line portions of the curves in different light intensities are the same,

but the apparent maximum excursion of surface potential changes. Most of this shift with light is due to a failure to satisfy the low frequency condition in the quasistatic capacitance measurement in the absence of the light. The observed flat-band voltage in the high light intensity 0.26V is shifted lower than the 5.5V work function difference between the front Au and the back Al contacts. The difference is mostly a shift caused by the light induced thinning of the depletion layer. This interpretation is supported by the fact that in this sample too there is no statistical broadening of the $G_p/\omega$ peaks that one would ascribe to fixed charges in the interface.

The density of states and the conduction band tail time constants extracted from fitting the $G_p(\omega)/\omega$ curve are shown in Figures (VI-5) and (VI-6), respectively. The interface state density curves are narrow and sharp. And again the time constants are shorter than suggested by the SRH model and exhibit sharp spectral features.

In order to test Eq. (V-55), we measured $G_p(\omega)/\omega$ at $V = -0.25V$ for different light intensities. At this applied bias it is possible to see the full peaks for most light intensities, so the time constants can be accurately determined. The light intensities and the time constants are listed in Table (VI-2). These time constants $\tau_v$ follow an exponential dependence on $P_0$ and are fit by the equation $\tau_v = 2.7 \times 10^{-3} \exp(-0.217P_0)$. Using Eq. (V-56) the electron-hole combination time $\tau_r = 98$ msec is determined. This time constant is about a factor of ten larger than that for Si-58. Thus $\tau_v$ in Si-101 is significantly more sensitive to light than it is in Si-58.

C. Si-102

A discussion of this sample is included because its behavior supports the trends found in Si-101 and a new feature was found in the conductance measurement. First, the quasistatic C-V curves were measured in the dark, and with light of intensities 1.60 $\mu W/cm^2$ and 16.5 $\mu W/cm^2$. These curves are very similar to those for Si-101: the fluorine lines are small, the structure of interface state density is sharp, the dark quasistatic capacitance curve does not satisfy the low frequency condition, and no fixed positive charges are present at the interface. Then we plotted $G_p(\omega)/\omega$ versus frequency. Once again these curves exhibit no statistical broadening and are consistent with the lack of fixed positive charges. However, there is a new feature in $G_p(\omega)/\omega$ in the accumulation region. Following the peak, the $G_p(\omega)/\omega$ curves usually fall monotonically with frequency. In Si-102 the curves begin to rise again toward the upper end of the frequency range of the capacitance bridge. The new peak is not reached by the upper limit of our frequency range. This feature can be explained as due to a non-ohmic back contact. This bad contact can slow the response time of the accumulation layer capacitance. This effect can be modeled in the equivalent circuit Figure (V-2) by adding a small resistance in series with $C_d/a$.

There are several possibilities for the cause of a bad contact:[37]

(i) The surface of the substrate was not clean, or the oxide was not thoroughly removed prior to the deposition of the aluminum.

(ii) In the process of e-gun deposition of Al, the pressure must be kept below 2 x $10^{-6}$ torr. A high background pressure is disastrous, resulting in films that are very cloudy, rough and grainy. Background pressures higher than 2 x $10^{-6}$ torr simply produce poor ohmic contacts.

(iii) After deposition, if the sample is not sintered at the correct temperature for the proper amount of time, the Al film will not adhere well to the subtrate and, hence, is not ohmic.

D. Si-107

This sample differs from the other because it has a (110) surface oxidized. The two curves in Figure (VI-7) are the raw quasistatic capacitance measurements with ramp rate 10.3 mV/sec in the dark and in the light. In this case the major effect of the light is to introduce an extra peak at E = 0.50 eV. This peak lies at the same energy as fluorine 2 found in Si-58. Since the ion implantation studies that allowed us to identify the sharp lines in Si-58 with fluorine at the (100) surface have not been performed on a (110) surface, no identification of this peak is possible. Whatever its origin, this feature behaves like a discrete level with a time constant that is reduced by light so these states respond to the varying gate voltage in quasistatic capacitance measurement only in the light. Our normal data reduction method has been followed and the resulting total interface state density is shown in Figure (VI-8). Only the peak centered at 0.50 eV is light sensitive.

The density of Si(110) surface atoms, $\rho_s = 9.6 \times 10^{14}$ atoms/cm$^2$, is a factor of $\sqrt{2}$ higher than that of the (100) surface. Hence one expects the interface state densities to be higher for (110) surface samples. While the qualitative behavior of Si-107 is as expected, the increase in the density of states compared with Si-58 is far larger than a factor of $\sqrt{2}$. Moreover, the observed states are confined to a narrower energy range and have a peak at 0.275 eV that is not present in the (100) surface sample.

There are other important differences between Si-58 and this sample. Si-107 has a finite positive fixed surface charge density and the peak of the $G_p(\omega)/\omega$ curves are statistically broadened. The statistical broadening makes it almost impossible to extract accurate interface state densities and time constants from the conductance method as discussed in detail in Section V. Time constants roughly determined from the peak positions are shown in Figure (VI-9). For the first time for one of our samples, the variation of $\tau_c$ as a function of surface potential follows the prediction of the SRH model. The capture cross section deduced from this data has the reasonable value, $\sigma = 7.1 \times 10^{-15} cm^{-2}$.

Table VI-1

| Sample | Surface Orientation | Composite Insulator | $C_0[n_F/cm^2]$ | $n_b[cm^{-3}]$ | $V_{FB}[V]$ |
|---|---|---|---|---|---|
| Si-58(298°K) | (100) | 250Å $LaF_3$/250Å $SiO_2$ | 139 | $2.42 \times 10^{14}$ | 0.81 |
| Si-58(77°K) | (100) | 250Å $LaF_3$/250Å $SiO_2$ | 123 | $1.90 \times 10^{14}$ | 0.91 |
| Si-101 | (100) | 250Å $LaF_3$/500Å $SiO_2$ | 75.7 | $1.93 \times 10^{14}$ | 0.26 |
| Si-102 | (100) | 250Å $LaF_3$/500Å $SiO_2$ | 66.4 | $2.12 \times 10^{14}$ | 0.52 |
| Si-107 | (110) | 250Å $LaF_3$/250Å $SiO_2$ | 98.3 | $4.12 \times 10^{13}$ | 1.20 |

Table VI-2

| $P_0[\mu W/cm^2]$ | 0.00 | 0.0632 | 1.60 | 4.45 | 7.01 |
|---|---|---|---|---|---|
| $\tau_v$[sec] | $3.0 \times 10^{-3}$ | $2.7 \times 10^{-3}$ | $1.7 \times 10^{-3}$ | $9.4 \times 10^{-4}$ | $6.0 \times 10^{-4}$ |

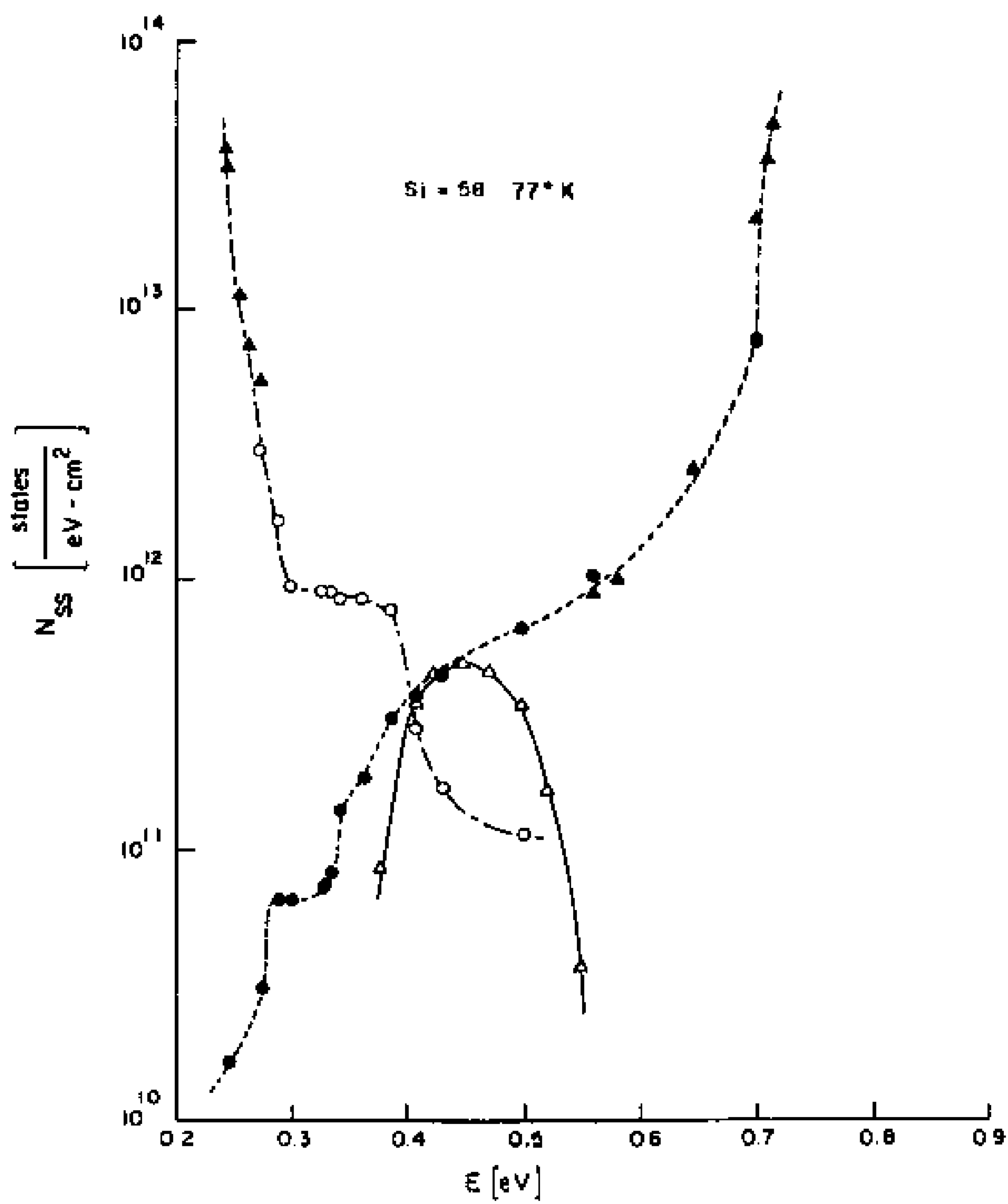


Fig. VI-1

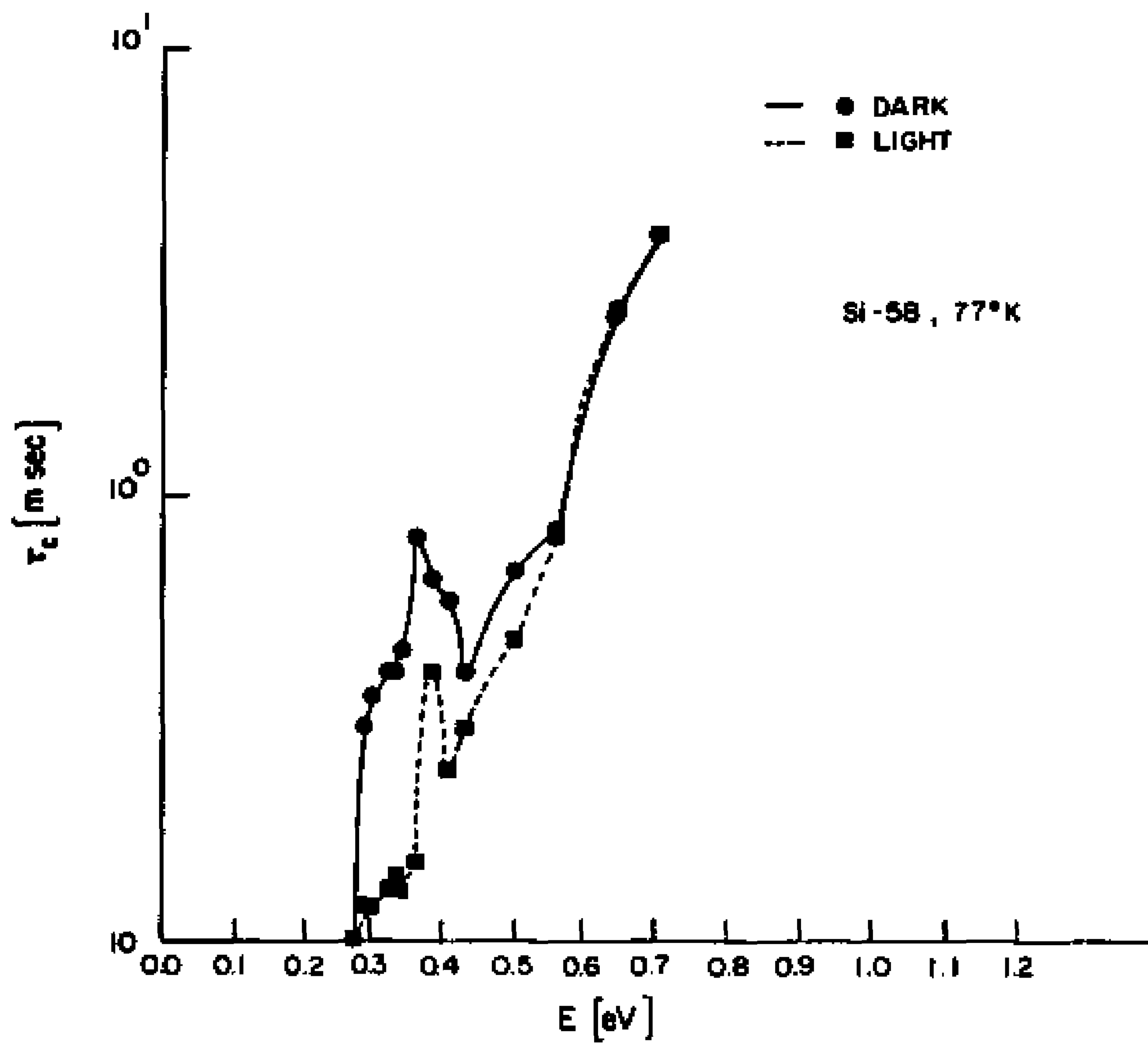


Fig. VI-2

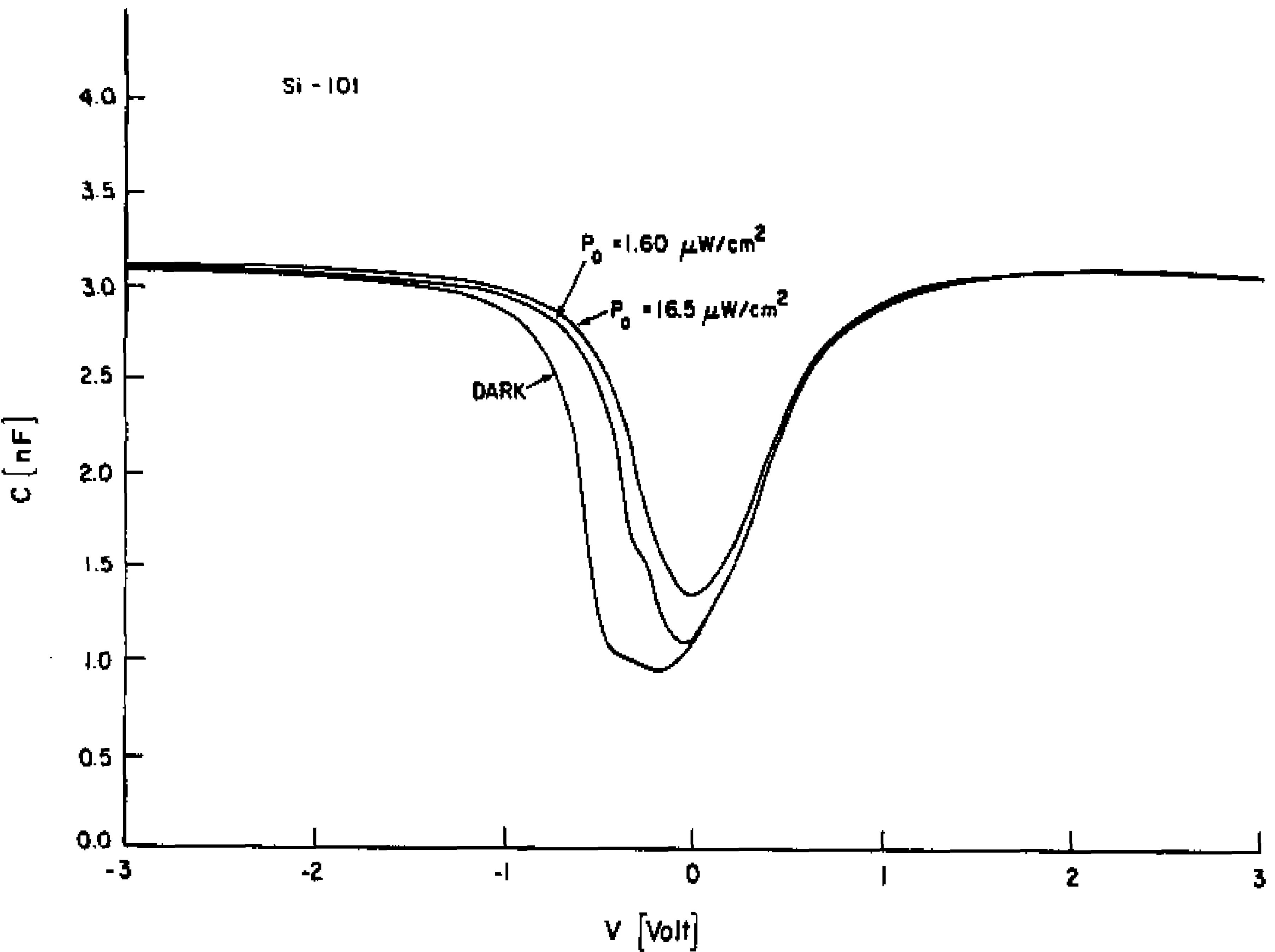


Fig. VI-3

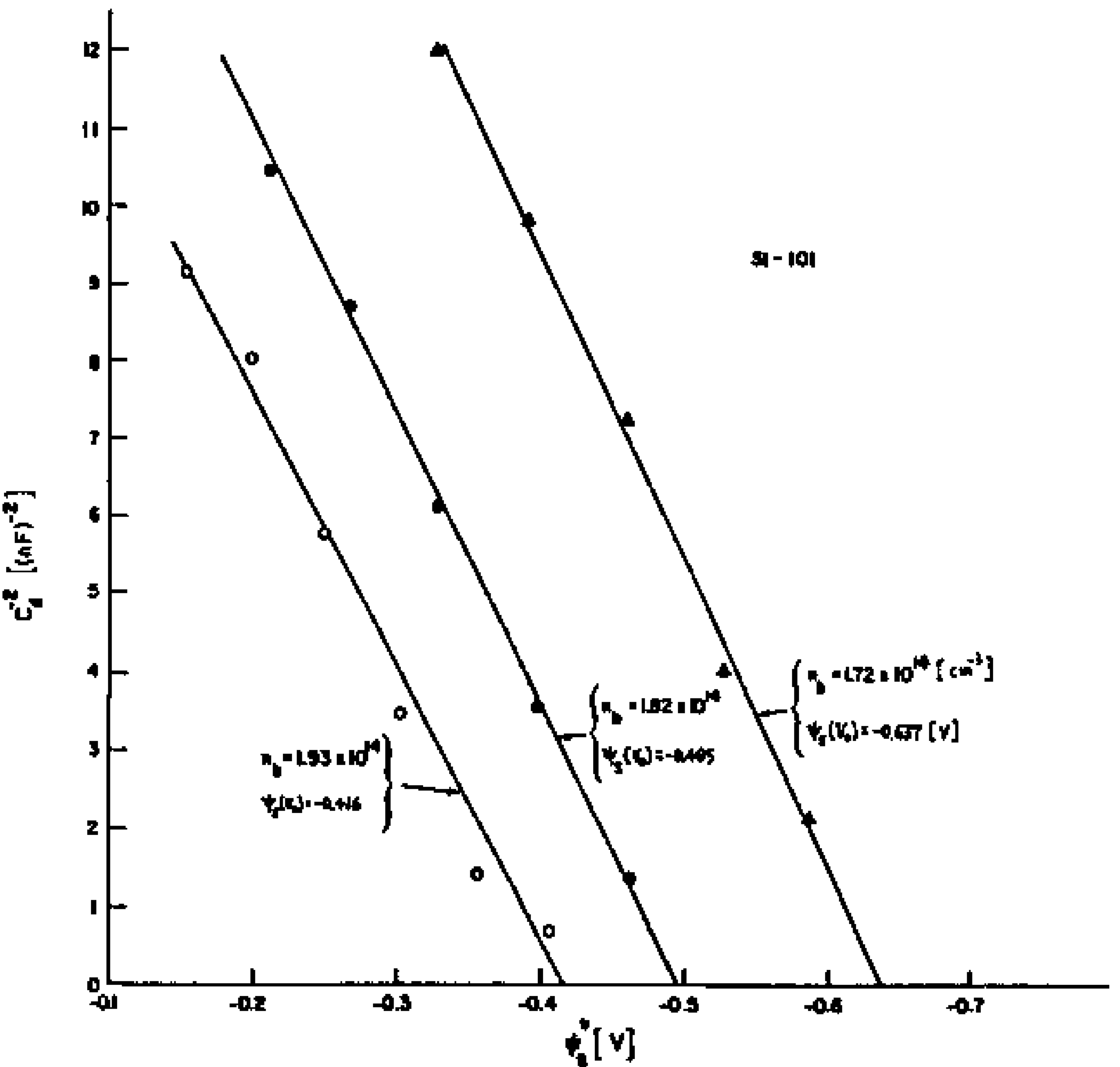


Fig. VI-4

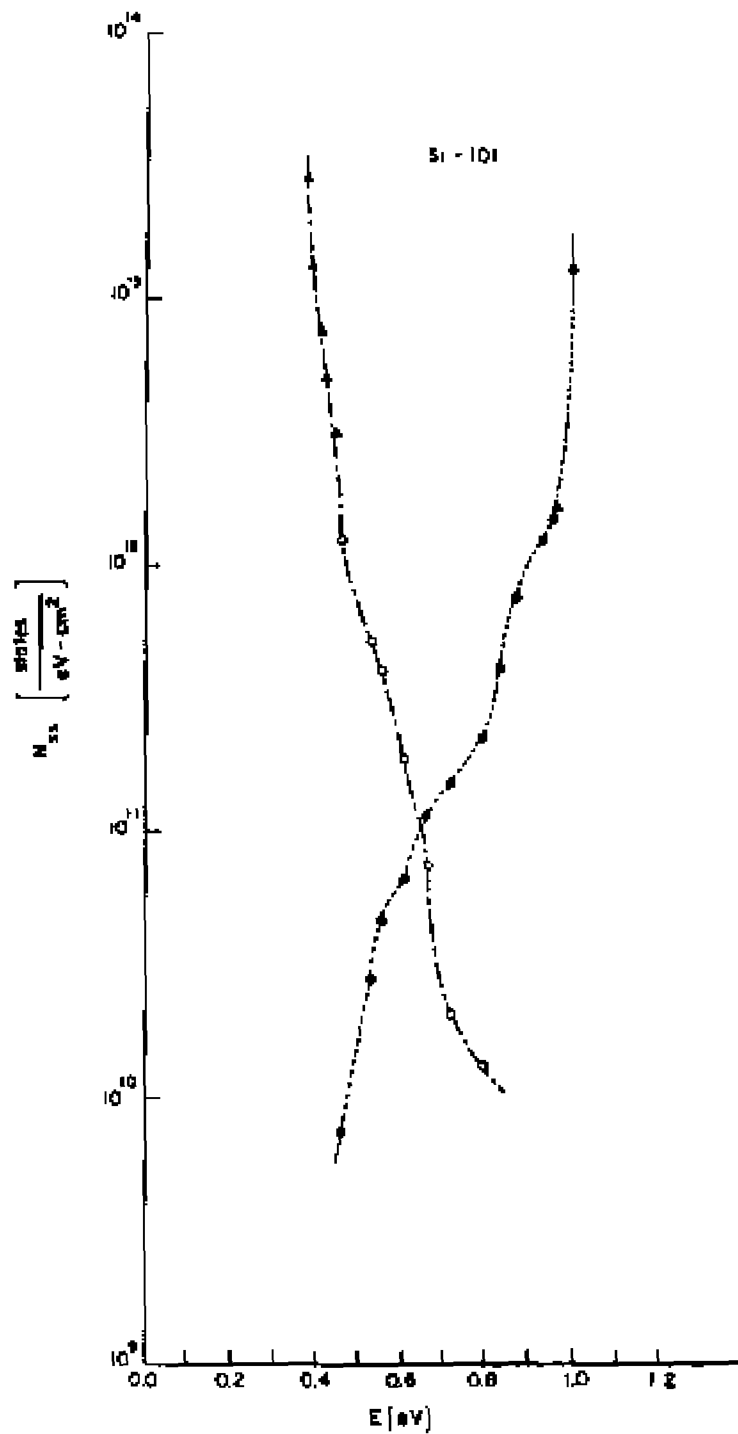


Fig. VI-5

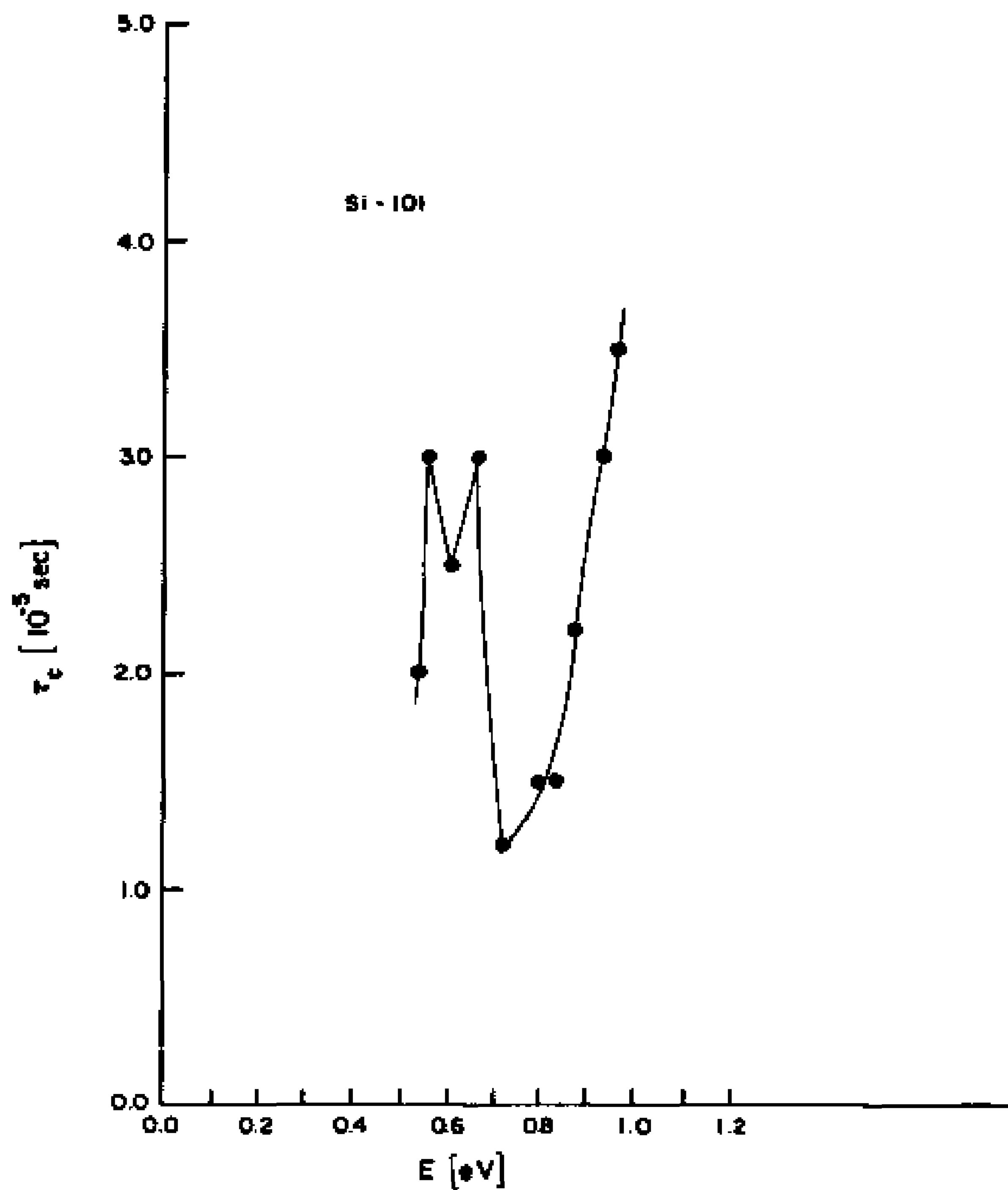


Fig. VI-6

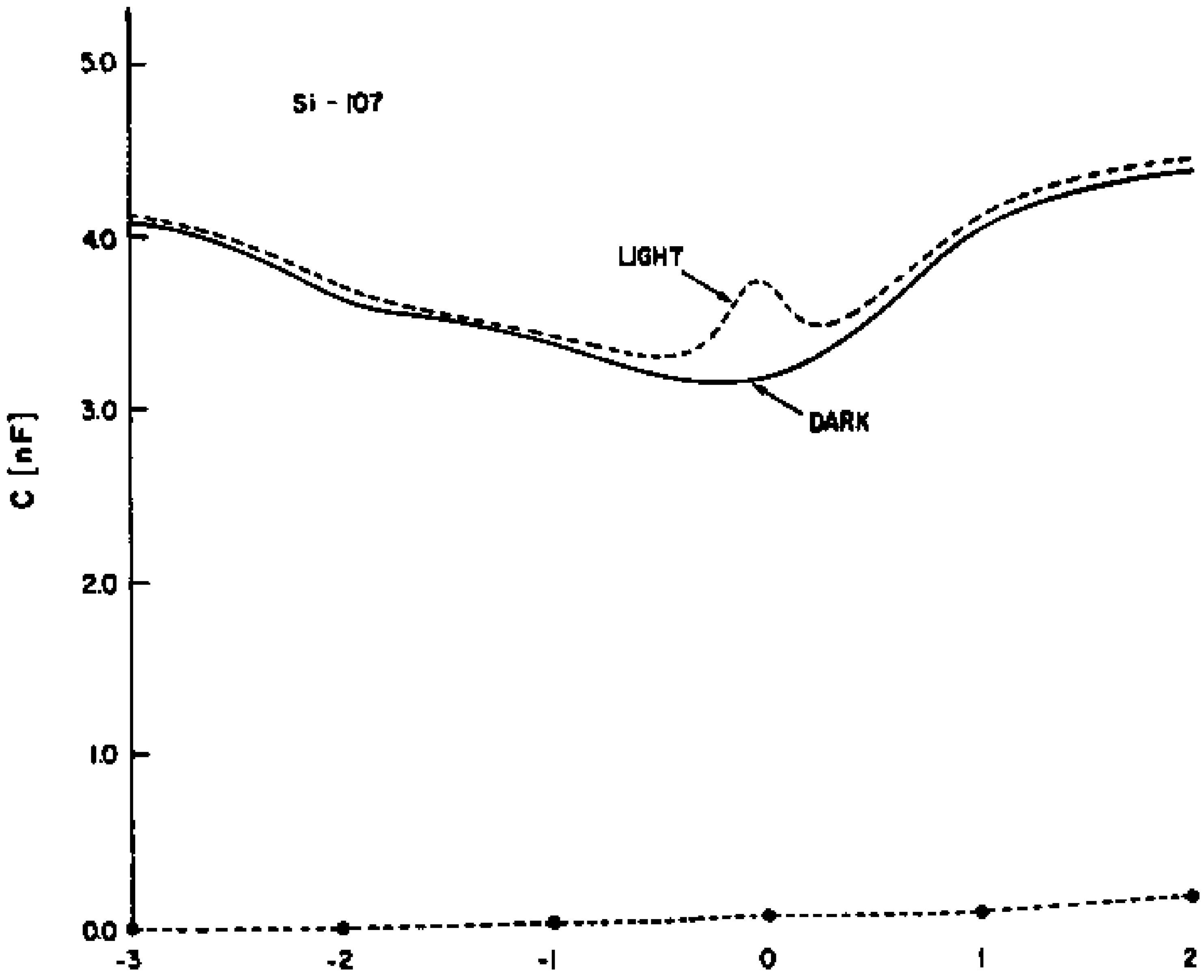


Fig. VI-7

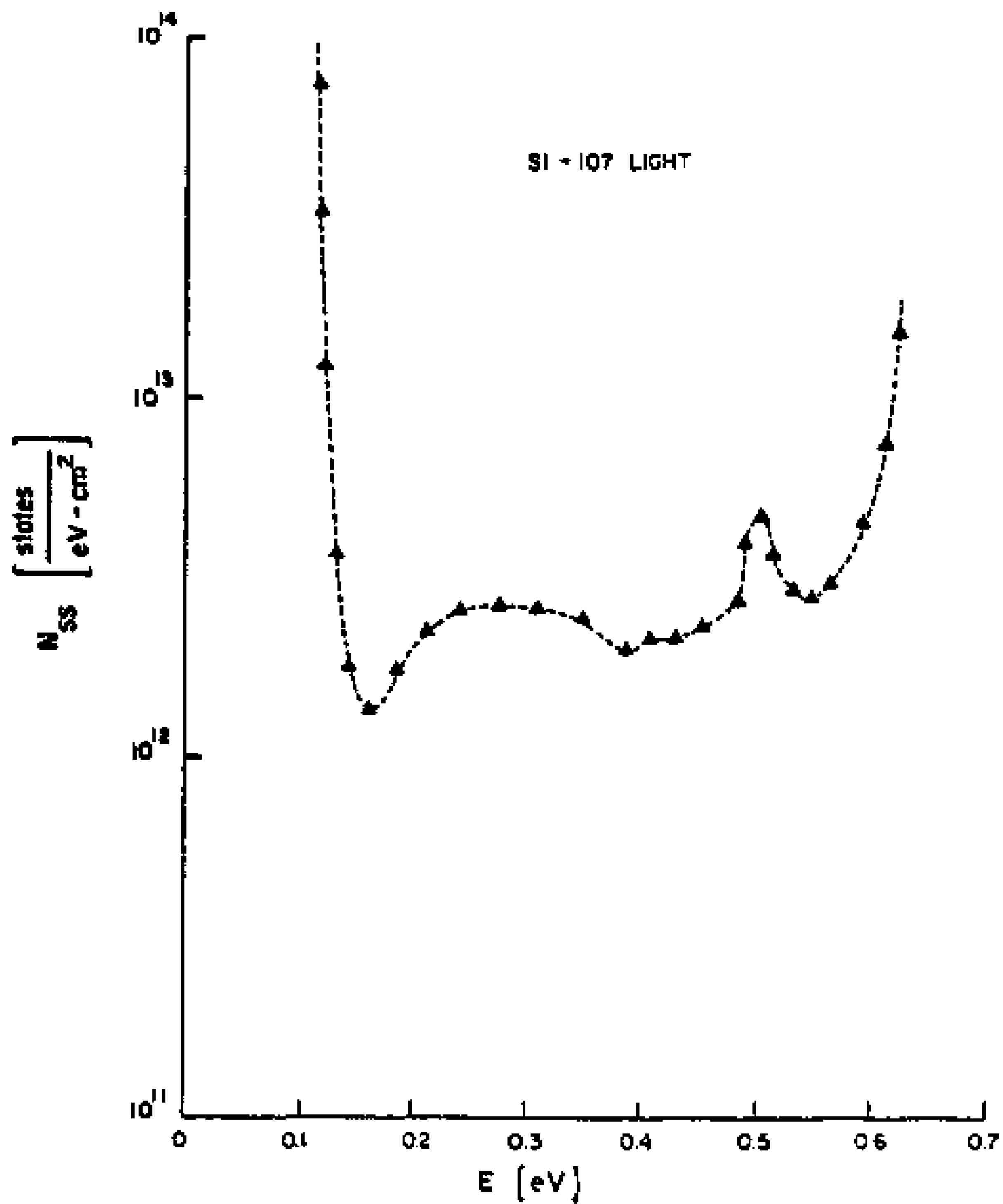


Fig. VI-8

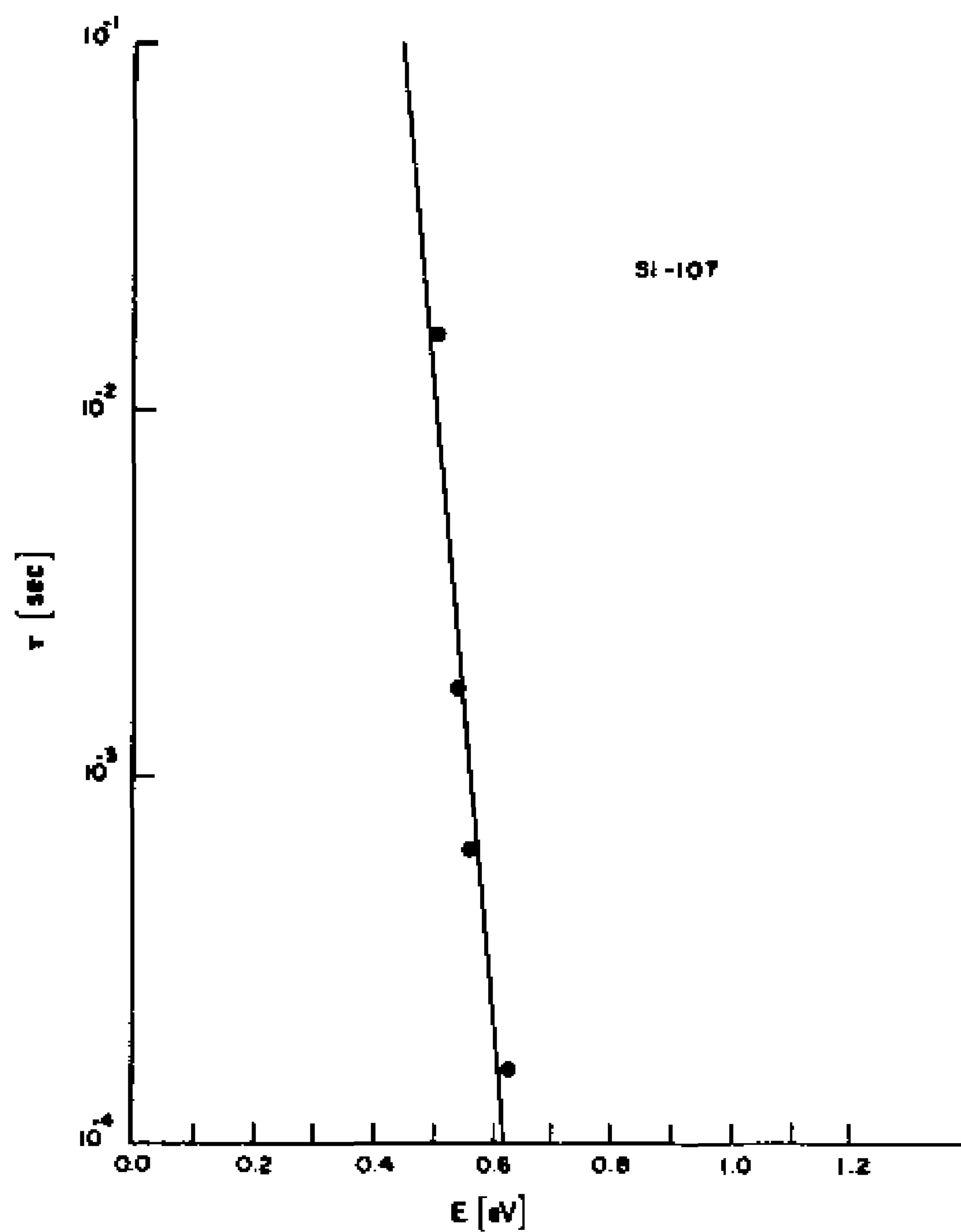


Fig. VI-9

## VII. DISCUSSION

We are now prepared to offer interpretations of the quasistatic and conductance measurement results. The interpretations are based on Si-58 room temperature data unless otherwise indicated, but they can be applied to other samples. We shall speculate about alternative interpretations, and suggest reasons for rejecting some of these alternatives.

Detailed theories of the interface states between Si and $SiO_2$ are just beginning to appear. Since these theories are structure-dependent and only the gross features of the interface structure are known,[31] the theories are not easily tested. Despite the enormous effort that has been devoted to the study of the Si-$SiO_2$ interface and the control that can be exercised to build good devices, the fundamentals are in a rudimentary state. Hence, we shall examine ours and other experimental information without reference to the developing theories, and later establish possible connections with them.

Good agreement is found between the results obtained from the quasistatic and conductance methods, so long as the continuum nature of interface state distributions is taken into account in interpreting the conductance method data. In contrast to the often-reported featureless U-shaped total density of states,[2,3] our well-resolved components show a great deal of structure with a number of prominent features:

1) The two light-sensitive peaks are fluorine-related state densities $N_{SS}^{f1}$ and $N_{SS}^{f2}$. They are very sharply peaked at energies E = 0.25 eV and 0.46 eV, respectively. The density $N_{SS}^{f1}$ is exceedingly narrow with a half-width at half-maximum of only $2.1 \times 10^{-3}$ eV.

2) The total area under the curve corresponds to $2.2 \times 10^{10}$ states/cm$^2$ or to $3.4 \times 10^{-5}$ states/atom on the (100) surface. The density $N_{SS}^{f2}$, on the other hand, has a half-width of $20 \times 10^{-3}$ eV and corresponds to $1.8 \times 10^{-5}$ states/atom. From these results one infers respective fluorine concentrations of 34 ppm and 18 ppm at the interface, respectively.

3) Near the energies 0.23 eV and 0.90 eV, labeled $E_{vs}$ and $E_{cs}$, respectively, the slopes of the curves become very large, so large that they seem to be approaching singularities.

4) The area under $N_{SS}^{v}$ and $N_{SS}^{c}$ corresponds to $7.9 \times 10^{-4}$ and $1.0 \times 10^{-3}$ states/atom of the (100) surface, respectively. Most of the states with energy in the band gap evidently lie below $E_{vs}$, or above $E_{cs}$, where their density is too large to measure.

5) While the $N_{SS}^{v}$ and $N_{SS}^{c}$ curves have some distinctive structure, they appear to be continuous rather than composites made of a finite number of discrete superimposed lines.

6) There are sharp features in both $N_{SS}^{v}$ and $N_{SS}^{c}$ in the vicinity of the second fluorine peak $N_{SS}^{f2}$.

While the present theoretical understanding of the Si-$SiO_2$ interface on a microscopic level remains rudimentary, it is of interest

to attempt to correlate our results with current ideas. The few quantum-mechanical calculations that have been performed on the interface[4] suggest the following picture for the origin of interface states. The "ideal" or intrinsic surface, defined as one possessing at least short-range order (i.e., without chemical or structural defects), has no states in the energy range of the bulk Si bandgap. All bandgap interface states are thus by-products of imperfections. Four very fundamental types of defects which can produce states in the gap are (i) chemical impurities, (ii) bond angle distortions of Si-O-Si bonds in the oxide or Si-Si bonds in the silicon, (iii) Si-Si bonds in the oxide, and (iv) dangling Si bonds in the vicinity of the interface. There is clearly considerable evidence both here, e.g., $f_1$ and $f_2$, and elsewhere[3] for impurity-derived states. Defects (ii), (iii), and (iv), on the other hand, have been only recently correlated with actual density-of-state features by Laughlin, et al.[38] Specifically, these workers find that Si-O-Si bond-angle distortions give rise to a conduction band tail of interface states, while distorted Si-Si bonds in silicon will introduce midgap interface states, but dangling Si bonds or Si-Si bonds in the oxide will produce trap-like states near both band edges.

The above picture strongly suggests, in agreement with our measurements, that the interface density of states will normally be made up of several distinguishable components and, in particular, that valence- and conduction-band-side states can indeed have different physical origins. Our measured densities $N_{SS}^{v}$ and $N_{SS}^{c}$ have the expected

shape and magnitude of band tails of major features to the left of $E_{vs}$ and to the right of $E_{cs}$, respectively. We have noted, in fact, that $N_{SS}^{v}$ approaches $E_{vs}$ in the manner of a scattering-induced band tail of the valence band edge.[39] The midgap structure in $N_{SS}^{v}$ and $N_{SS}^{c}$, on the other hand, is reminiscent of the effect on a continuum caused by a strong scattering resonance, such as $N_{SS}^{f2}$ apparently represents. But in any case, the actual relationship between the midgap structure and $N_{SS}^{f2}$ should be readily accessible to further investigation through direct control of the fluorine content at the interface.

Two other experimental results about these systems are useful additions to those listed above. First, in photoemission experiments[6] interface states for cleaved Si and partially oxidized surfaces to vacuum have been identified. Some of these states are found to lie adjacent to the valence-band edge and to protrude into the band gap. The energy resolution of such experiments is of order 0.1 eV and the sensitivity is limited to state densities greater than $10^{12}$ states/eV-$cm^2$. Second, low-temperature surface-conductance measurements on n-channel MOSFET structures and a complementary theory have established the existence of two-dimensional surface energy band structures.[39-41] These bands exhibit minigaps that are attributed to periodic superlattice potentials established at the Si-$SiO_2$ interface.

A consistent picture that accounts for all the observations, and also have some elements in common with the new theories, has the following features:

## A. The "Ideal" $Si-SiO_2$ Interface

The "ideal $Si-SiO_2$ interface," one with no chemical impurities, no fixed charge, a moderately abrupt transition from Si to $SiO_2$ that is confined to a few lattice spacings, and with at least short-range order, has states located below the energy $E_{vs}$ and above $E_{cs}$. Then $E_{vs}$ and $E_{cs}$ are the surface-valence and conduction-band edges, respectively. The states below $E_{vs}$ are the ones seen in photoemission and the ones above $E_{cs}$ are the ones responsible for the n-channel conduction properties with the minigaps. The occurrence of periodic superlattice potentials at the interface could conceivably arise from imperfections, but it seems much more likely that this is a property that should be ascribed to the "ideal interface".

## B. Scattering-induced band tails

The $N^{v}_{SS}$ and $N^{c}_{SS}$ curves in Figure (V-13) are the band tails of the principal interface states described above. Using the very general scattering theory,[42] these tails can be thought of as states caused by scattering from defects in the "ideal interface". The defects may be categorized as usual into two classes, imperfections and impurities. It is a bit difficult to identify imperfections in the interface without first defining the structure of the "ideal interface". However, if, for example, an ideal interface has a characteristic sequence of bond-angle distortions, a deviation from the ideal sequence would constitute an imperfection. If oxygen vacancies and silicon dangling bonds are

part of the ideal interface, then one located in the wrong place would again be an imperfection, etc.

In terms of this picture, one can think of ideal densities of interface states $N^{v}_{SSO}(E)$, $N^{c}_{SSO}(E)$ that are confined to energies $E < E_{vs}$ and $E > E_{cs}$, respectively. The scattering theory[42] can then be invoked to relate the ideal density of states to the observed band tails,

$$N^{j}_{SS}(E) = \int d\varepsilon \frac{N^{j}_{SSO}(\varepsilon)\Delta_j(E)/\pi}{[\varepsilon - E - \Lambda_j(E)]^2 + \Delta_j^2(E)} , \quad j = v, c , \qquad \text{(VII-1)}$$

where $\Lambda_j$ and $\Delta_j$ are the real and imaginary parts of the scattering-induced self-energies. If one examines this expression in energy-intervals E far removed from the band edges - that is, $|E - E_{js}| \gg \Delta_j$, $\Lambda_j$ - then Eq. (VII-1) simplifies to

$$\begin{aligned} N^{j}_{SS}(E) &\cong \frac{\Delta_j(E)}{\pi} \frac{1}{(E - E_{js})^2} \int d\varepsilon\, N^{j}_{SSO}(\varepsilon) \\ &= \frac{\rho_s \Delta_j(E)}{\pi} \frac{1}{(E - E_{js})^2} . \end{aligned} \qquad \text{(VII-2)}$$

For definiteness we have identified the remaining integral in Eq. (VII-2) with $\rho_s$, the density of Si surface atoms, where $\rho_s = 6.8 \times 10^{14}$ atoms/cm$^2$ for the (100) surface. Both the room temperature and liquid nitrogen temperature data, calculated from Eq. (VII-2) are plotted in Figure (VII-1). If the scattering causing the band tails all arose from states with

energies well away from the band edges - e.g., charged centers - then the $\Delta_j$'s would decrease monotonically from the band edges.[43] The structure in $\Delta_v$ and $\Delta_c$ is a fingerprint of the scattering mechanisms contributing to the measured interface-state density.

There is a measure of ambiguity in the interpretation of the gross features of the $\Delta_v$ and $\Delta_c$ behavior. First, the scale of $\Delta_v$ and $\Delta_c$ is set by the assumption that the integral in Eq. (VII-2) equals $\rho_s$ for both cases. This could be true for one but not the other, or for neither. Until this point is settled, no conclusion can be drawn from the relative magnitudes of $\Delta_c$ and $\Delta_v$. Using the scale indicated leads to $\Delta_c$ with a maximum of about 130 $\mu$eV or a corresponding scattering lifetime of $\tau_{min} = \frac{h}{2(\Delta_c)_{max}} = 2.4 \times 10^{-12}$ sec at room temperature. If the scale is proper, then $\Lambda_c$, which would be of the same order as $\Delta_c$, is quite small compared to $E - E_{cs}$ over the energy range considered, so dropping it is correct. However, if the energy scale is grossly different, then $\Lambda_c$ may not be so small and the apparent sharp decrease in $\Delta_c$ from 0.65 to 0.90 eV (or 0.43 to 0.70 eV at 77°K) may be only an artifact of the approximation that $\Lambda_c$ is small. Then, the major structure in $\Delta_c$ would all be a part of the general monotonic fall of $\Delta_c$. On the other hand, if the scale is properly set, then the major peak in $\Delta_c$ around 0.6 eV (or 0.4 eV at 77°K) must be caused by a resonance with defects states at that energy. Presumably these states have too low a density to be seen directly, and their presence can be detected only by their effect on the

conduction-band tail. Evidence to support this later position will be presented shortly.

Examining the curves in Figure (VII-1), it is evident that both peaks of the self energies for the conduction and valence band tails are shifted toward the valence band side at 77°K in comparison with those at the room temperature. Notice that not all the lines shift by the same energy, so this general trend is not likely to be just an artifact of the method. Moreover, the principal peaks narrow and become higher, while their areas are nearly preserved. Since the major peaks have unresolved shoulders on them, they are evidently composites of lines with different origins. It will be necessary to perform controlled experiments intended to modify these features one at a time if they are to be identified. The important point here is that this method of collecting and reducing data allows one to see such detail.

On sample Si-101 the higher light intensity that was used at 77°K was again used to see if it caused any artifacts in the data. The imaginary parts of the self energies were deduced from Eq. (VII-2) and are plotted in Figure (VII-2). Their gross structure is similar to $\Delta_c$ and $\Delta_v$ of Si-58. However, both $\Delta_c$ and $\Delta_v$ for Si-101 are narrower. The peak height of $\Delta_c$ is about a factor of two smaller and these spectral features are shifted toward the conduction band relative to the corresponding quantities for Si-58. Since in the higher light intensity the trends of $\Delta_c$ and $\Delta_v$ for Si-101 shift in the opposite direction to those in Si-58 from room temperature to 77°K, we conclude that these shifts and line shape changes are not caused by the light.

C. Hybridization and resonant scattering

The sharp structure in $N_{SS}^{v}$ and $N_{SS}^{c}$ (and $\Delta_v$, $\Delta_c$) in the energy range 0.25 to 0.5 eV will be interpreted next. The rapid variations of $N_{SS}^{v}$ and $N_{SS}^{c}$ occur near the coincidence of two effects. The first is that this is the energy range where the states $N_{SS}^{v}$ and $N_{SS}^{c}$ meet, and as a consequence might be expected to hybridize. Second, this is also near the energy of the 0.46-eV fluorine peak, and it may act as a strong resonant scattering center for the continuum states in the valence- and conduction-band tails.

The relative importance of these two mechanisms can be determined by examining the $\Delta_c$ curve in Figure (VII-1) and estimating some numbers. Notice in Figure (VII-1) that there is a sharp peak in $\Delta_c$ just at 0.46 eV. If this peak is ascribed to the fluorine resonance and its height $\Delta_{cf2}$ is estimated as $\Delta_{cf2} \lesssim 30$ $\mu$eV, then the effective scattering range of this feature $\ell_{f2}$ is

$$\ell_{f2} \cong \frac{2\Delta_{cf2}}{\hbar \bar{v}_s \rho_{f2}} \lesssim 200\,\text{Å} \cong 70 \text{ lattice spacings} \qquad \text{(VII-3)}$$

where $\bar{v}_s = 4 \times 10^6$ cm/sec is the surface thermal velocity of electrons with a free electron mass, and $\rho_{f2} = 1.2 \times 10^{10}$ atoms/cm$^2$ is the measured fluorine 2 surface density. An effective range of 70 lattice spacings is at the upper limit of what might be considered reasonable for a scattering center, even one as disruptive as fluorine. Two conclusions can be drawn from this result: the scale of $\Delta_c$ as set by $\rho_s$

is not too small, a possibility raised earlier; and since the peak $\Delta_{cf2}$ is small and confined to a narrow energy range compared to the structure in $\Delta_c$ and $\Delta_v$, the fluorine is not the principal contributor to this structure.

This leaves us with hybridization as the most likely explanation of most of the sharp features in $N^v_{SS}$ and $N^c_{SS}$. There is an additional piece of evidence to support this interpretation. Notice that the main peaks and valleys of $\Delta_v$ and $\Delta_c$ in the energy range 0.25 to 0.5 eV anticorrelate. This is exactly what one expects in a two-band, strong-scattering case. The valleys arise in the scattering rates because the density of final states into which scattering can occur decreases in those energy ranges where hybridization-caused band gaps open.

While the fluorine resonance and hybridization are the most likely explanations of the sharp features in $N^v_{SS}$ and $N^c_{SS}$, two other mechanisms have been examined. We considered the possibility that the features are van Hove singularities in the scattering-induced band tails,[44] or depressions in the density of states arising from superlattice-produced minigaps. Both van Hove singularities and minigaps occur at special wave numbers. The observed sharp features in both $N^v_{SS}$ and $N^c_{SS}$ all appear at nearly the same energy. It is unlikely that this energy corresponds to the same wave number for both band tails. The explanations that involve energy resonances are more compelling in view of the data, so we have tentatively rejected the alternatives.

The final question we wish to address in this section is the nature of the observed variation of $\tau_c(E)$ with energy, shown in

Figure (V-14). Clearly, the variation differs significantly from the prediction of the SRH model, which is also shown in Figure (V-14) for comparison.

While we have no detailed explanation of the origin of this difference, there are features of the interface-state density that suggest modifications in the usual SRH treatment. The high state density $N^c_{SSO}$ in the energy range between $E_{cs}$ and $E_c$ can act as an electron reservoir for the lower-lying states. Depending on the relative rate $r_1$ of electron exchange between $N^c_{SS}$ and $N^c_{SSO}$, the rate $r_2$ between $N^c_{SSO}$ and the electrons in the bulk-conduction band beyond the depletion layer, and, finally, the rate $r_3$ between $N^c_{SS}$ and the bulk-conduction band electrons, different energy variations of $\tau_c^{-1}$ may occur.

<u>Case A</u>: If $r_3$, $r_1 \ll r_2$, then the usual SRH time constant ${}_{SRH}$ results. Our Si-107 sample falls into this class. The time constant measured on Si-107 follows the prediction of the SRH model.

<u>Case B</u>: If $r_2 \ll r_3$, $r_1$, then the states $N^c_{SSO}$ act as a reservoir and

$$\begin{aligned} \tau_c &= \tau_{SRH} \exp -\left[ (E_c - E_{cs})/kT \right] \\ &\cong 2 \times 10^{-4} \, \tau_{SRH} \quad . \end{aligned} \tag{VII-4}$$

The explanation of the observed behavior of $\tau_c$ may be that for E well below $E_{cs}$, case B holds, and $\tau_c$ is much smaller than predicted by the ordinary SRH model. However, as E approaches $E_{cs}$, there are two changes. The state density $N^c_{SS}$ increases, and the transition

probabilities per unit time from a state $N_{SS}^{c}$ to one of the states $N_{SSO}^{c}$ also increase because the energy difference is smaller. Hence, the situation tends to change from Case B to Case A, where the states $N_{SSO}^{c}$ no longer behave as an electron reservoir. It is impossible to turn this into a quantitative theory without knowing $N_{SSO}^{c}$ and the energy dependence of capture cross section. In addition to the gross trends just discussed, the spectral features found in $\tau_c$ must also be explained. An understanding of these features will undoubtably help establish the origin of the various contributions to the interface states. The anomalous variation of $\tau_c$ with energy is another indication that some samples, such as Si-58, Si-101, differs from those studied previously. However, some other samples, such as Si-107, do behave as predicted by SRH model.

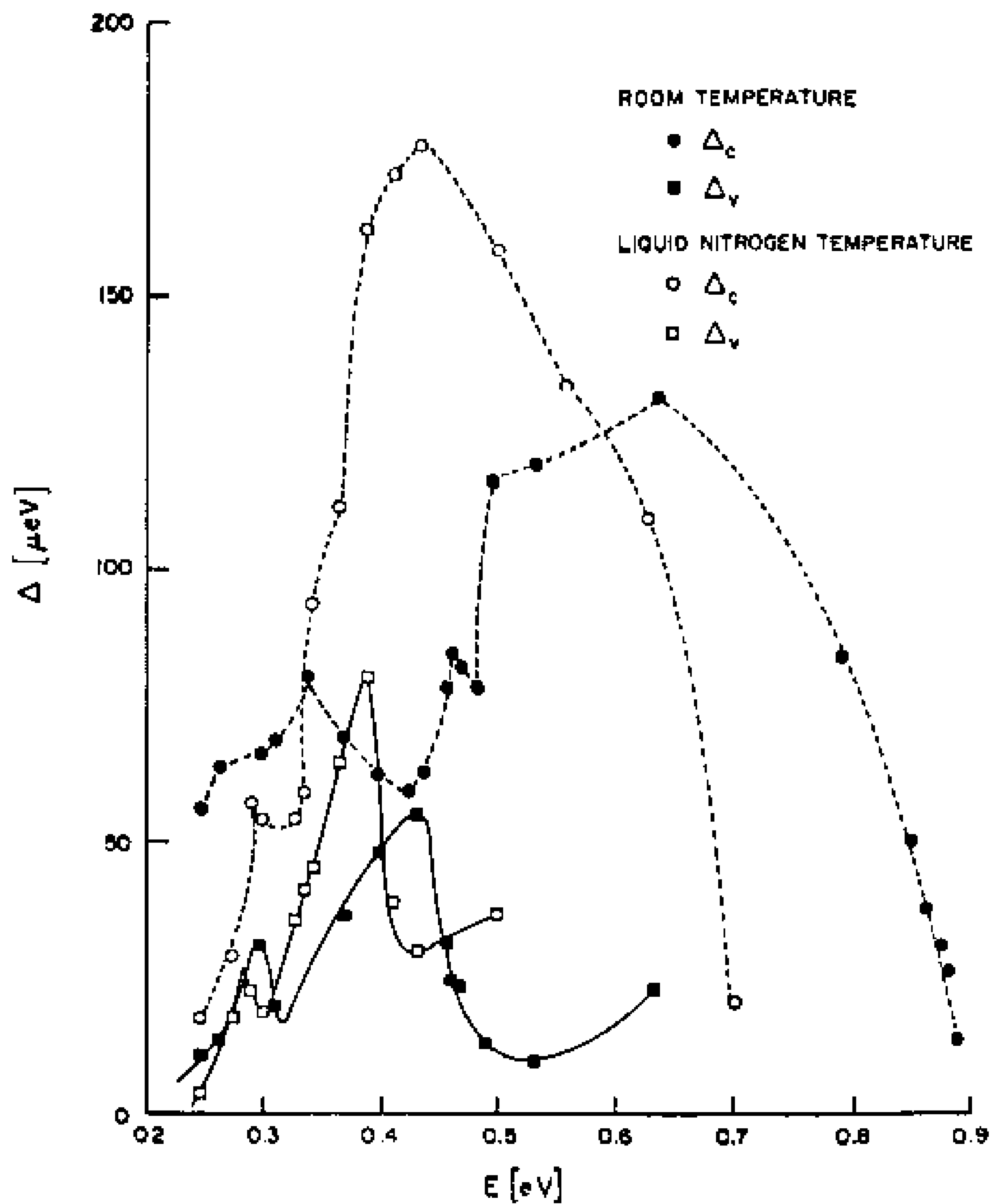


Fig. VII-1

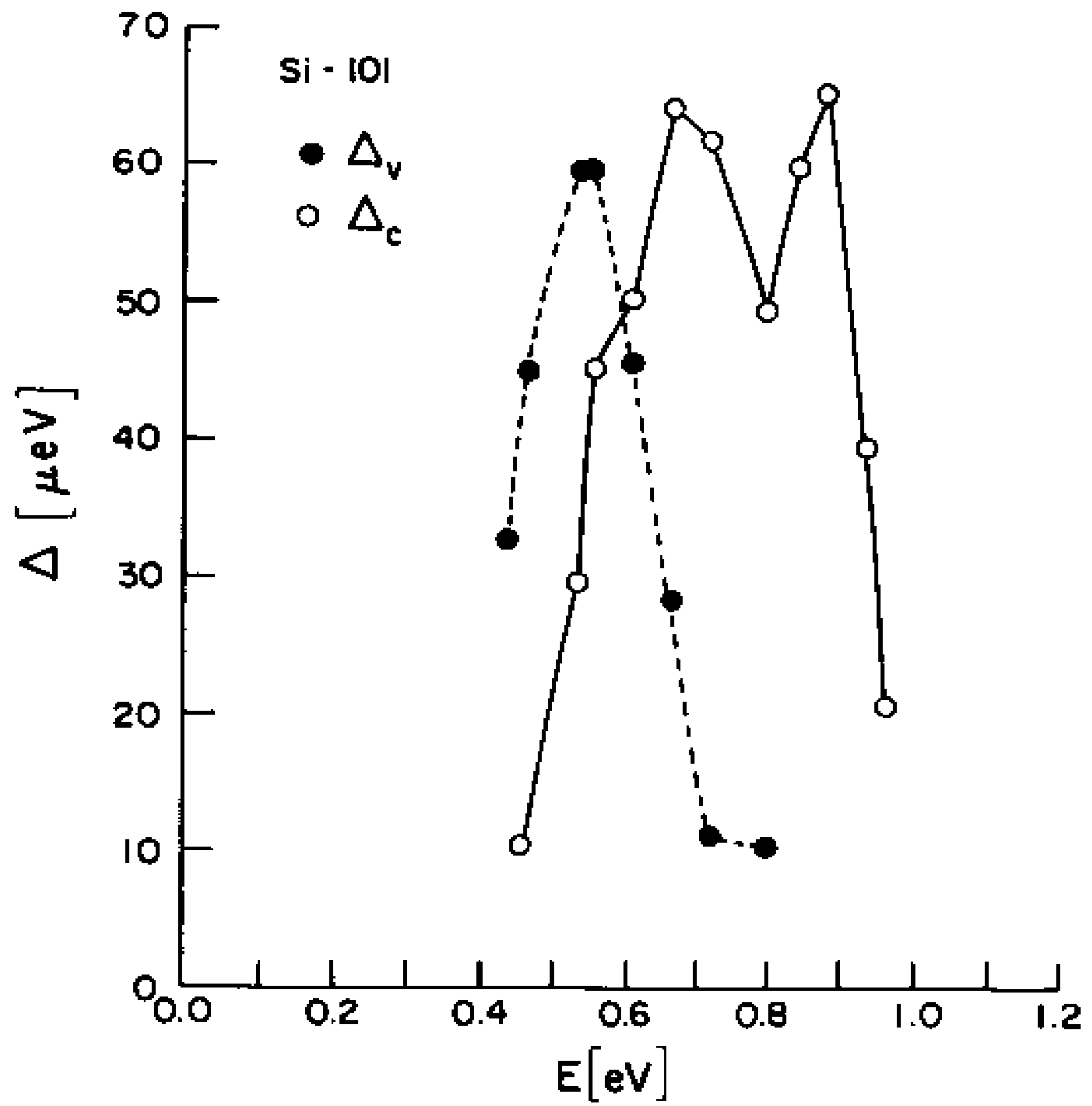


Fig. VII-2

# VIII. CONCLUDING REMARKS

We have made several additions to the techniques of electrical measurement used to study interface states. These are: the use of effectively thin composite insulators, low carrier concentration substrates, and low-intensity light that creates electron-hole pairs in the space-charge region. While these modifications are easy to put into effect, they introduce surprisingly profound differences in the experimental results.

In the absence of the light, it would be almost impossible to reach the quasistatic condition and still retain a useful signal-to-noise ratio with our samples. The main consequences of not satisfying this condition are that the surface-potential distribution deduced from the measurement is too broad and some state densities are underestimated. This causes interface-state profiles to seem smoother than they are in fact. It can also lead to incorrect conclusions about the number of positive fixed charges. In light of these results, experiments on fixed charge should be re-examined. For example, some of the changes introduced by annealing or by radiation effects may be due to time-constant modifications rather than to actual changes in the number of fixed charges.

The light also allows the interface-state density to be measured throughout the band gap, using the conductance method. The main

advantage of the conductance method is that using it we can decompose the interface-state density into partial contributions from different origins. When this is done, distinctive structure in the interface-state densities becomes evident.

The main interface-state density seems to be concentrated at energies in the range $E \lesssim E_{vs}$ and $E_{cs} \lesssim E$ where they are too large to be observed. The features at energies $E_{vs} \lesssim E \lesssim E_{cs}$ are evidently band tails of the major densities. The sharp structure in the midgap region is probably due to hybridization of the valence- and conduction-band tails. Laughlin et al.[38] and Herman et al.[45] both predict that there are no states in the band gap for an "ideal" interface. Only defects in the ideal arrangement produce such states. Laughlin et al. find a conduction band tail that arises from Si-O-Si bond-angle distortions, while Si-Si bond distortions can produce a valence band tail. Dangling Si bonds in silicon cause midgap states, while dangling Si bonds or Si-Si bonds in the oxide produce trap-like states near both band edges. It is impossible at present to uniquely identify any of the theoretically predicted features with the observed ones. To do this, we must devise experiments designed to modify one feature at a time.

Our oxide was grown in dry $O_2$ and was thin, so the sample was maintained at the growth temperature for a relatively short time ($\lesssim$ 8 min). It was never intentionally exposed to $H_2$ or $H_2O$ at an elevated temperature. Consequently, the interface properties reported here may be qualitatively different from those measured on thicker

oxides, for which the interface is not abrupt,[46] and those exposed to hydrogen. It is imperative that other samples, prepared in different ways, be subjected to our improved measurement technique.

## REFERENCES


1. E. H. Nicollian, J. Vac. Sci. Technol. 14, 1112 (1977).
2. This subject is extensively reviewed in a book by S. M. Sze, Physics of Semiconductor Devices (Wiley, New York, 1969).
3. The literature of MOS-C structures prior to 1976 is reviewed by A. Goetzberger, E. Klausman, and M. J. Schultz, CRC Critical Reviews in Solid State Sci. 6, 1 (1976).
4. More recent work and additional references can be found in Proceedings of the International Topical Conference on the Physics of $SiO_2$ and its Interfaces, edited by S. T. Pantelides (Pergamon, New York, 1978).
5. D. E. Eastman and W. D. Grobman, Phys. Rev. Lett. 28, 1378 (1972).
6. L. F. Wagner and W. E. Spicer, Phys. Rev. Lett. 28, 1381 (1972).
7. E. H. Nicollian and A. Goetzberger, Bell Sys. Tech. Jour. 45, 1055 (1967).
8. K. Ziegler and E. Klausmann, Appl. Phys. Lett. 26, 400 (1975).
9. R. Castagne and A. Vapaille, Surf. Sci. 28, 157 (1971).
10. A. Sher, W. E. Miller, Y. H. Tsuo, J. A. Moriarty, R. K. Crouch, and B. A. Seiber, Appl. Phys. Lett. 34, 799 (1979).
11. R. F. Pierret and C. T. Sah, Solid St. Electron 13, 269 (1970); C. T. Sah, L. Forbes, L. L. Rosier and A. F. Fasch, Jr., Solid St. Electron 13, 759 (1970); C. T. Sah and H. S. Tsu, IEEE Trans. Electron Devices ED-21, 202 (1974); W. J. Stepowicz, Solid St. Electron 20, 817 (1977).

12. K. Lehovec, Appl. Phys. Lett. 8, 48 (1966).

13. K. Lehovec, A. Slobodskoy, Electronics 7, 59 (1964).

14. W. Shockley and W. T. Reed, Phys. Rev. 87, 835 (1952).

15. R. Castagne, C. R. Acad. Sci. Paris 267, 866 (1968).

16. D. R. Kerr, Inter. Conf. on the Properties and Use of MIS Structures, Grenoble, 1969, ed. J. Bovel, p. 303.

17. M. Kuhn, Solid St. Electron 13, 873 (1970).

18. C. N. Berglund, IEEE Trans. Electron Devices ED-13, 701 (1966).

19. L. M. Terman, Solid-St. Electron 5, 285 (1962).

20. P. V. Gray and D. M. Brown, Appl. Phys. Lett. 8, 31 (1966).

21. D. R. Frankl, J. Appl. Phys. 38, 1966 (1967).

22. D. Lang, J. Appl. Phys. 45, 3023 (1974).

23. C. T. Sah, Solid-St. Electron 19, 975 (1976).

24. K. Yamasaki, M. Yashida, and T. Sugano, Jap. J. Appl. Phys. 18, 113 (1979).

25. J. A. Cooper, Jr. and R. J. Schwartz, Solid-St. Electron 17, 641 (1974).

26. A. G. Nassibian, L. Farsone, and J. G. Simmons, J. Appl. Phys. 50, 1439 (1979).

27. C. N. Berglund, IEEE Trans. Electon Devices ED-13, 701 (1966).

28. Private communication, Jacket et al., Hughes report on germanium technology (1979).

29. W. Fahrner and A. Goetzberger, J. Appl. Phys. 44, 725 (1973).

30. W. Fahrner and A. Goetzberger, Appl. Phys. Lett. 21, 329 (1972).

31. A. Goetzberger, Proc. 5th Conf. on Solid State Devices, Tokyo 1973, Supplement, J. Japan Soc. Appl. Phys. 43, 289 (1974).

32. H. Deuling, E. Klausmann, and A. Goetzberger, Solid-St. Electron 15, 559 (1972).

33. G. Declerck, R. van Overstraeten, and G. Bronx, J. Appl. Phys. 45, 2593 (1974).

34. K. Ziegler and E. Klausmann, Appl. Phys. Lett. 28, 678 (1976).

35. C. Werner, H. Bernt, and A. Eder, J. Appl. Phys. 50, 7015 (1979).

36. A. Sher, Y. H. Tsuo, J. A. Moriarty, W. E. Miller, and R. K. Crouch, J. Appl. Phys. (manuscript number 8053 R, in press).

37. F. Hegner and A. Fenerstein, Solid-St. Tech. 21, 49 (Nov. 1978).

38. R. B. Laughlin, J. D. Joannopoulos, and D. J. Chadi, reference 3, p. 321.

39. T. Cole, A. A. Lakhani, and P. J. Stiles, Phys. Rev. Lett. 38, (1977); P. J. Stiles, T. Cole, and A. A. Lakhani, J. Vac. Sci. Technol. 14, 969 (1977).

40. L. J. Sham, S. J. Allen, A. Kamgar, and D. C. Tsui, Phys. Rev. Lett. 40, 472 (1978).

41. D. C. Tsui, M. D. Struge, A. Kamgar, and S. J. Allen, Jr., Phys. Rev. Lett. 40, 1667 (1978).

42. A. B. Chen, G. Weisz, and A. Sher, Phys. Rev. B5, 2897 (1972). The expression for a density of states that is modified by strong scattering is given in Eq. (130). The argument leading to this equation is quite general and applies equally well to imperfection-modified interface states.

43. A. B. Chen and A. Sher, Phys. Rev. B 17, 4726 (1978); A. B. Chen and A. Sher, Phys. Rev. Lett. 40, 900 (1978).

44. H. C. Hwang and A. Sher, Phys. Rev. B 12, 5514 (1975).

45. F. Herman, T. P. Batra, and R. V. Kasowski, reference 3, p. 333.

46. D. E. Aspnes and J. B. Theeten, Phys. Rev. Lett. 14, 1046 (1979).

## VITA

Pin Su

Born in Taiwan, China, 24 February 1951. Graduated from National Cheng-Kung University in Taiwan with B. S. degree, 1973, with concentration in physics and mathematics.

In September, 1975, the author entered the College of William and Mary as a graduate assistant in the Department of Physics.